ELECTRONIC AND OPTICAL PROPERTIES OF OXIDE THIN FILMS

A Dissertation

Presented to the Faculty of the Graduate School

of Cornell University

In Partial Fulfillment of the Requirements for the Degree of

Doctor of Philosophy

by

Steven Daniel Kirby

August 2009

INTERESTING OXIDE THIN FILMS USING OFF-AXIS SPUTTERING

Steven Daniel Kirby, Ph. D.

Cornell University 2009

Off-axis sputtering has been used to study two oxide thin film systems. The first study involved developing an epitaxially grown NiO/$SrTiO_3$ heterostructure to be used for a negative index of refraction. The second used off-axis sputtering as a combinatorial approach to study the effects of doping and codoping of transparent conducting ZnO.

A negative index of refraction should be possible by combining only intrinsic material resonances. We proposed that combining NiO, which has an antiferromagnetic resonance in the far infrared, and $SrTiO_3$, which has a dielectric resonance in the far-infrared, can be used to achieve a negative refractive index of refraction in the far-infrared. These resonances can be shifted through changing temperature, doping, or through applying a magnetic field. A high quality epitaxially grown composite heterostructure and bulk ceramics have been fabricated. Preliminary measurements of the permeability and permittivity been taken for a bulk composite structure. The $SrTiO_3$ ionic resonance can be seen in a reflection technique while the NiO antiferromagnetic resonance is easily seen in a transmission technique

ZnO is a potential inexpensive replacement for indium tin oxide (ITO) as a high-end transparent conductor. However, ZnO has not replaced ITO in many applications such as flat-panel displays due to high resistivity and poor thermal stability. ZnO has been doped with many elements including Al, In and Ga. We proposed that codoping with both Al and In might result in size compensation which

would lead to improved dopant solubility and therefore better electrical conductivity and stability.

A high-throughput combinatorial approach was used to study codoping of ZnO with both Al and In. Measurement of the deposited composition spread suggests that codoping results in much improved conductivity. By adding 1% In to highly Al-doped ZnO (3-6%) the conductivity increases by an order of magnitude. Thermal annealing in a variety of atmospheres including air, vacuum and hydrogen results in some understanding of the difference in the two dopants. It was found that Al doping results in a higher carrier concentration than In doping, but any excess Al greatly decreases the mobility. In doping improves the mobility but with lower carrier concentrations. Calculations based on density functional theory support the experimental data, showing that Al is a shallower dopant than In. Unit cell volume comparisons between theory and experiment correspond well. The interplay between substitutional doping, oxygen vacancies, and possible adventitious H doping makes the doped ZnO system difficult to analyze definitively.

BIOGRAPHICAL SKETCH

Steven Kirby, originally from Moatsville, WV graduated from Philip Barbour High School in 1998. He then went to Rochester, NY where he majored in the Microelectronic Engineering program at the Rochester Institute of Technology. While there, he completed two internships at Dominion Semiconductor in Manassas, VA and one at Micron Inc. in Boise, ID. He also acted as vice-president for Tau Beta Pi for one year. He graduated with a B.S. in Microelectronic Engineering in May 2003. Desiring a further understanding of the origins of semiconductor material properties, he began studying Materials Science and Engineering at Cornell University in the fall of 2003 and joined the research group of Prof. R.B. van Dover.

This dissertation is dedicated to my wife who put up with me as a graduate student.

ACKNOWLEDGMENTS

I would like to acknowledge all the people who have helped me mentally, physically and spiritually during my time at Cornell. First, I have to thank my advisor Prof. R. Bruce van Dover for being a friendly, patient and extremely knowledgeable advisor. It only took him a year to convince me to not use MS Excel for my figures. I also would like to thank Prof. Mike Thompson and Prof. David Muller for their assistance and excellent feedback on my work. Special thanks also to Prof. Richard Hennig who took the extra time to teach and help me with the computational work.

There have been many collaborators who have helped with this work. Mark Lee at Sandia National Labs helped with some FTIR measurements. Prof. Farhan Rana and his student Jared Strait in ECE at Cornell were very helpful in getting THz TDS measurements on my samples in a timely manner. I also would like to thank Maura Weathers for help in getting started in the XRD facility, Dr. Stephen Menasian for help with RBS and John Hunt for help with the Microprobe.

I must thank those students who have helped me directly and indirectly in this work. The van Dover group members have helped in a number of ways. I'd like to thank Jon, Sara, Karen, John, Mark, Maxim, and Noble for an infinite amount of help and fun. I'd also like to acknowledge the undergraduates that have done work has been very enlightening even if not necessarily included here.

I would like to thank Prof. Sass for making my first TA position a very enjoyable and enlightening experience. I'd also like to thank Prof. Thompson and Prof. Liddell for more very enjoyable TA positions. If in the future I find myself teaching at some level, my experience with these professors will become invaluable.

I very much need to acknowledge the Graduate Christian Fellowship at Cornell, which has helped me spiritually and mentally. The perspective and

knowledge gained from studies and roundtables has not only helped me spiritually in ways that can hardly be described, but also helped clear my head and has lead to better research in my own studies.

I'd particularly like to acknowledge Ray Fertig with whom I have had many meaningful (and not) discussions on everything from research to politics to religious matters. He also helped me to "cowboy up" so that I actually started to date Angela.

I would like to acknowledge my family who have been very supportive during my time at Cornell. I thank my Mom for all the love and work that she has given me throughout my life. Of course lastly I must thank Angela for all the support that she has given me during some of the most stressful times of my graduate studies. Coming home to a loving wife has helped immensely.

TABLE OF CONTENTS

LIST OF FIGURES

LIST OF TABLES

CHAPTER 1

INTRODUCTION: EPITAXY AND COMBINATORIAL OXIDE THIN FILMS

1.1 – Introduction: Epitaxial Growth of Oxide Films

Magnetic and ferroelectric thin film materials are useful for a number of applications. Magnetic and ferroelectric properties depend strongly on the crystal quality of the film [1-2]. For this reason, there is strong motivation for growing magnetic and ferroelectric films epitaxially; that is, with a single crystal orientation relative to the substrate. In the following sections, a method of achieving a negative index of refraction using magnetic and ferroelectric thin films is proposed. In order to obtain a negative index of refraction, the magnetic and ferroelectric materials must have high crystal quality in order to achieve the required magnetic and dielectric qualities. In this case, the properties required are lowly damped magnetic or dielectric resonances.

1.2 – Negative Index of Refraction in the Far-Infrared

The index of refraction or refractive index n of a material is a material property that describes how electromagnetic waves interact with the material. It can be defined as the ratio of the velocity of the wave in the medium v to the speed of the light in vacuum c. From Maxwell's equations, the refractive index is found to be related to the permittivity ε and permeability μ of the material as:

$$n = \frac{c}{v} = \pm\sqrt{\varepsilon\mu} \tag{1.1}$$

It is well known that the speed of light in a material is lower than the speed of light in vacuum. This means that for well-behaved materials, n is greater than 1 and light in the material acts as we expect. This means that as an electromagnetic wave travels from vacuum into a material with an index of refraction n, the speed of the wave slows from c to v. The frequency of the wave remains constant while the wavelength decreases, causing an apparent bending of the light. This effect is seen

when looking at a straw "bend" in a glass of water. This change in direction of the incident wave is well defined by Snell's Law:

$$n_1 \sin\theta_1 = n_2 \sin\theta_2 \qquad (1.2)$$

Normally, n is greater than unity and the angle relative to the surface must decrease in the material relative to the incident angle. The wave is said to refract in a normal "right-handed way", which leads to the complex shapes needed for high quality lenses.

In 1968, Veselago postulated that a material with a negative permittivity and a negative permeability should have a negative index of refraction [3]. This leads to interesting effects such as a negative group velocity and "left-handed refraction". This results in the possibility of achieving a focal point in a lens that is perfectly flat. Pendry added to the theory of Veselago by predicting the possibility of near perfect lenses unconstrained by the diffraction limit [4], at least in the near field. Evanescent waves that typically are exponentially decaying waves do not propagate in standard materials. In a material with a negative index of refraction, these waves become exponentially increasing and do propagate. Fourier analysis shows that these waves contain information on a length scale much smaller than the wavelength of light and therefore can be used to image smaller than the standard diffraction limit suggests. Negative index materials might lead to a number of interesting applications including improved coupling in antennae [5], monolithic microwave integrated circuits [6], and improved optics and lenses [7-8].

Both negative permittivity and negative permeability are needed in order to obtain a negative index of refraction. No material exhibits either a negative permittivity or negative permeability as a fundamental materials property. However, it is possible for negative permittivity or negative permeability to occur near a resonance frequency. At frequencies above a weakly damped magnetic or dielectric resonance, the permeability or permittivity can have a negative excursion for some range of

frequencies. For a material that exhibits both a dielectric and a magnetic resonance, if the frequency range for negative permeability matches the frequency range for negative permittivity, a negative index of refraction results at that frequency range.

A negative index of refraction was first realized experimentally in 2001 by Shelby, Smith and Schultz [9]. They used an array of copper strips to achieve an electronic resonance at about 10 GHz. They matched this resonance with an array of split ring resonators to achieve a negative permeability. They verified that this metamaterial shows an effective negative index of refraction through Snell's Law.

The work by Pendry and Shelby, Smith and Shultz has lead to a large amount of research in studying negative index of refraction material. The status of the field was extensively reviewed in October 2008 [10-14]. In general, the field has focused on either using metamaterials such as those discussed above [10-12] or using photonic crystals [13]. Photonic crystals use diffractive effects to mimic a negative index of refraction. Even for the metamaterials, the size of the structure is on the scale of a wavelength, so diffraction effects are possible. Furthermore, for optical frequencies, the structures become more difficult to fabricate using standard lithography. Also, there would be great difficulty in achieving a truly three-dimensional negative index using metamaterials. If a material could be designed to use intrinsic material properties to get the negative index of refraction, the structure problems of metamaterials and photonic crystals would not have to be considered.

Theoretical work suggests that a layered material with alternating layers of negative permittivity (and small permeability) and negative permeability (and small permittivity) would act as a material with a negative effective index of refraction [15-16]. The composite material should exhibit a negative refractive index if the size of each phase of the composite is significantly smaller than the wavelength of interest. We next consider the three regions of the electromagnetic spectrum where it might be

viable to match a dielectric resonance with a magnetic resonance in order to obtain a negative index of refraction: the visible to ultraviolet, the UHF to microwave region and the infrared region.

For the visible to ultraviolet region, there are many choices for dielectric resonance. Electronic polarization modes tend to occur in this region. These are very lightly damped and often result in a negative permittivity over a range of frequencies. The options for magnetic materials are less obvious. Conventional magnetic resonances (ferromagnetic resonance) occur at frequencies far lower than optical frequencies, certainly less than about 100 GHz.

In the microwave frequency region (1-100GHz), there are many materials that exhibit suitable magnetic resonances and negative permeability. Ferromagnetic resonances can be lightly damped in insulating materials such as garnets [17]. Ferromagnetic materials are well understood and often result in a negative permeability. Dielectric polarization modes in the microwave region are typically due to dipolar modes. These tend to be very highly damped and do not result in a negative excursion of the permittivity. If a material with a suitable dielectric resonance were identified, it could undoubtedly be incorporated in a composite with a magnetic resonance material to yield a negative index of refraction in the microwave region.

The infrared region appears to be most promising. The resonance frequencies of ionic modes in dielectric materials tend to be in this region. For example, $SrTiO_3$ has a mode with a characteristic frequency at about 100 cm^{-1} at room temperature [18]. Antiferromagnetic materials can have a magnetic resonance at similar frequencies. NiO, for example, has an antiferromagnetic resonance (AFMR) of about 35 cm^{-1} [19-20]. It should be possible to synthesize a composite material that matches an ionic resonance with an AFMR in the far infrared region to obtain a negative index of refraction.

In order to engineer a negative index of refraction in the infrared, the region of negative permittivity and the region of negative permeability must occur at the same frequency. It should be possible to shift the dielectric resonance of $SrTiO_3$ to lower frequency by either lowering the temperature or adding Ba, thus softening the ferroelectric phonon mode [18]. It should also be possible to shift the NiO AFMR by either applying an external magnetic field or increasing the anisotropy by doping with Fe or Co [20]. Using a combination of these methods, it should be possible to achieve a negative index of refraction in the far infrared.

1.2.1 Tuning the $SrTiO_3$ dielectric resonance

Cochran [21] proposed that a ferroelectric transition in certain crystals is associated with an optic mode of the lattice becoming unstable below the critical temperature. This mode approaches zero frequency as the temperature approaches the Curie temperature. The temperature dependence of this mode is given by $\omega_{FE}^2 \propto T - T_c$. Barker [22] used experimental data [18, 23] to develop an equation for this resonance frequency as a function of temperature for $SrTiO_3$.

$$\omega^2(SrTiO_3) \approx 35T - 1200 \qquad (\text{cm}^{-1}) \tag{1.3}$$

Equation 3 represents a good fit to the data over the temperature range 85-300 K, though extrapolation to $\omega = 0$ implies a Curie temperature of 34 K, which is known to be incorrect. This equation should give a reasonable estimate of the temperature dependence of the $SrTiO_3$ phonon mode at temperatures away from the Curie temperature. Equation 3 can be rewritten to emphasize the dependence on $T - T_C$.

$$\omega^2(T, T_C) \approx 35(T - T_C) \qquad (\text{cm}^{-1}) \tag{1.4}$$

at 300K

$$\omega^2(T = 300K) \approx -35T_C + 10500 \qquad (\text{cm}^{-1}) \tag{1.5}$$

Equation (5) gives an estimate of the response of the room temperature resonance frequency to the change in Curie temperature due to doping. Of course, as T_C approaches 300K, the linear approximation is no longer valid.

It is possible to adjust the Curie temperature of $SrTiO_3$ by doping. The Curie temperature of (Ba, Sr)TiO_3 has been reported by Alexandru et al [24], who found that the Curie temperature increases linearly with increased Ba content.

$$T_C \approx 360 x_{Ba} + 33 \qquad \text{(K)} \tag{1.6}$$

Substituting Equation 6 into Equation 4:

$$\omega^2(x_{Ba}) \approx 9345 - 12600 x_{Ba} \quad (\text{cm}^{-1}) \tag{1.7}$$

We have now identified two methods of shifting the $SrTiO_3$ dielectric resonance. The resonance frequency will decrease with decreasing temperature (Equation 3) or with increased Ba content (Equation 7).

1.2.2 Tuning the NiO Antiferromagnetic Resonance

it is well known that the square of the AFMR frequency is proportional to the exchange field H_E and the effective anisotropy field H_A.

$$\omega_{AFMR}^2 \propto H_E H_A \tag{1.8}$$

This results in an AFMR frequency for NiO of about 36 cm^{-1}. Other ions, such as Co^{2+} and Fe^{2+}, have higher anisotropy energies than Ni^{2+} so we anticipate that doping NiO with Co^{2+} or Fe^{2+} will raise the AFMR frequency. Becker et al [20] have experimentally confirmed this behavior. They also showed that the AFMR frequency is increased greater for Co^{2+} doping than for Fe^{2+} as expected based on the particularly high anisotropy associated with Co^{2+}. For small dopant concentrations, the square of the AFMR frequency was found to increase linearly with concentration [20], indicating that the exchange field is essentially unaffected. At a Co^{2+} doping level of 6.6%, the AFMR frequency was found to shift to about 65 cm^{-1}.

By setting the effective exchange energy and the anisotropy energy to be averages of the contributions from host and dopant ions, Becker et al [20] minimized the sum of these energies to obtain a simple equation for the AFMR as a function of Co doping.

$$\omega^2 = 4zJ^{HH}\left[(1-x)S^H H_A^H + xS^D H_A^D\right] + 8xzJ^{HH} H_A^H S^D \times \left(1 - \frac{J^{HH}}{J^{HD}}\right) \qquad (1.9)$$

H and *D* refer to the host ions and defect ions respectively. *J* terms refer to the exchange interaction parameters, H_A are the anistotropy field for the given ion, *z* is the number of effective nearest neighbors (taken to be six).

Table 1.1. Magnetic Constants for Ni^{2+} and Co^{2+} in NiO

Ion	**Ni^{2+} (cm^{-1})**	**Co^{2+} (cm^{-1})**
J	*71.3*	*29.6*
H_A	*0.75*	*18*

The values of these material constants associated with Equation 9 were inferred from the literature [20, 25-27] and are summarized in Table 1. Substituting these values in Equation 9 yields a simple linear equation for the AFMR as a function of doping concentration:

$$\omega_{AFMR}^2 \approx 45000x + 1300 \qquad (\text{cm}^{-1}) \qquad (1.10)$$

This equation is a good fit to experimental data for Co^{2+} doping for NiO for x <, 0.07. Above this level, peak broadening limited the ability to measure the resonance. This effect limits the extent to which the AFMR can be shifted with doping: if a peak becomes too broad, it will not result in a negative excursion in the permeability.

Equation 9 can also be used to determine the effect of an applied field. Any external applied field will simply add to the anisotropy field in the equation if the field is applied in a direction coincident with the anisotropy axis. This can be used to yield a significant increase in the AFMR frequency. Thus we have identified two methods for tuning the AFMR resonance of NiO: applying a magnetic field in the range 1 – 10 T, and doping with 1 – 10 at% Co.

1.2.3 Matching the NiO AFMR with $SrTiO_3$ dielectric resonance

To achieve a negative index of refraction, it is necessary to engineer the frequencies of the AFMR in NiO and the dielectric resonance in $SrTiO_3$ so as to overlap. The NiO AFMR can be shifted by applying an external field or by doping with a high anisotropy ion such as Fe^{2+} or Co^{2+}. The $SrTiO_3$ dielectric resonance can be shifted by a decrease in temperature or by doping with Ba to increase the ferroelectric Curie temperature. This allows for several approaches to achieve a matched resonance at frequencies in the far-infrared.

Figure 1.1 shows the temperature response of both the NiO AFMR and the $SrTiO_3$ dielectric resonance. The AFMR does not change much with temperature below 300 K. Sievers and Tinkham [19] showed that the AFMR only shifted from about 34 to 36 cm^{-1} when decreasing from 300 to 2 K. The $SrTiO_3$ resonance is much more sensitive to temperature, so simply changing the temperature of the NiO/$SrTiO_3$ composite should give a coincident resonance. As seen in Figure 1.1, we estimate that this will occur at about 75 K, though we emphasize that this prediction is only approximate because the model is very crude.

Figure 1.2 shows the room temperature AFMR frequency shift of NiO in response to doping by Co, along with the shift in the $SrTiO_3$ dielectric resonance as a result of Ba doping. The effect of applying a modest magnetic field of 3 T is also shown. Even at zero field, coincident resonances can be arranged over a wide range of

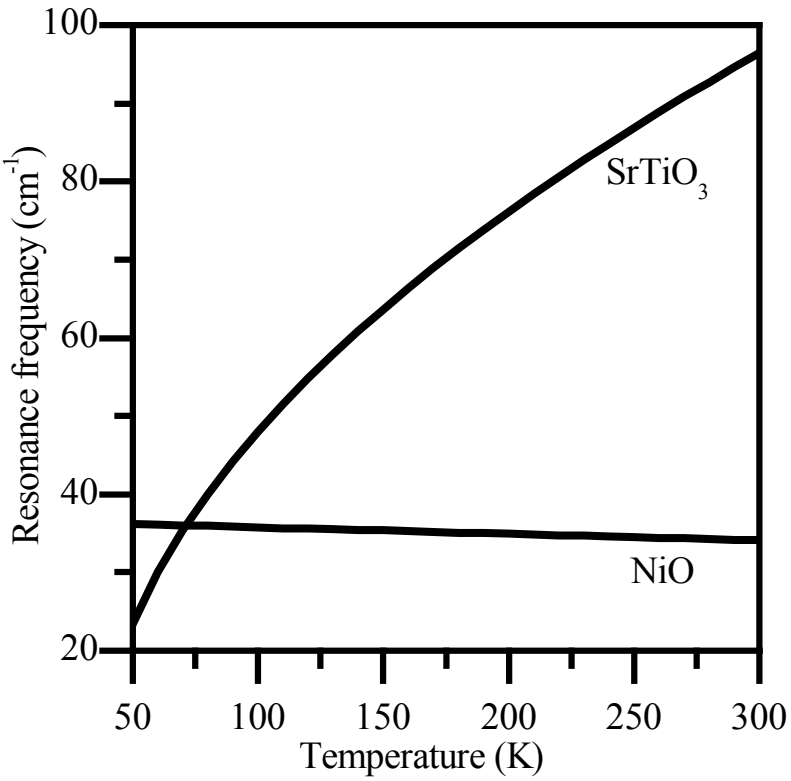

Figure 1.1: Temperature response of the resonance frequencies of $SrTiO_3$ and NiO. The NiO AFMR has little change in this range due to the high Neél temperature. The $SrTiO_3$ dielectric resonance approaches zero as temperature approaches 0 K.

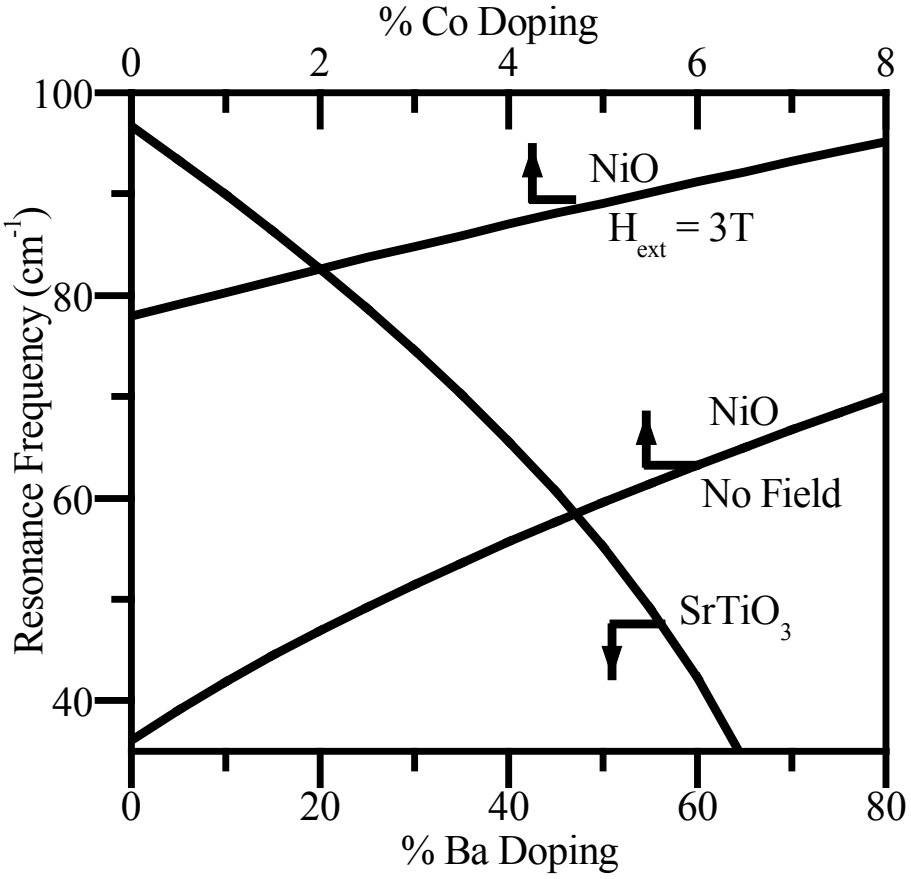

Figure 1.2: The effect of Ba doping on the $SrTiO_3$ dielectric resonance and Co doping and applied field on the NiO AFMR at 300 K. Using both doping and applied magnetic field should allow for resonance matching in the entire range between the intrinsic NiO AFMR (~36 cm^{-1}) and the $SrTiO_3$ dielectric resonance (~100 cm^{-1}).

frequencies (~40 to 70 cm^{-1}) by doping. Including the magnetic field, it should be possible to achieve matched resonance at a chosen frequency within the entire range from 40 cm^{-1} to almost 100 cm^{-1}. For example, a sample composition of ($Sr_{.46}Ba_{.54}TiO_3/Co_{.027}Ni_{.973}O$) should exhibit both a dielectric resonance and the AFMR at 50 cm^{-1} (1.5 THz). Assuming that the linewidth of the NiO is ~2 cm^{-1} [20] and the $SrTiO_3$ linewidth is much larger than this [18], this system should exhibit a negative index over the range 50-51 cm^{-1} (1.50 – 1.55 THz). The magnitude of negative index is not trivial to predict. For terahertz radiation incident on a thin film or finely dispersed composite material, the wavelength is much larger than the structure of the composite, so we approximate the effective permeability and permittivity of the composite by volume-weighted averages for the $SrTiO_3$ and NiO. $SrTiO_3$ has $\mu = 1$so even if the NiO resonance is broad (small negative permeability) the system should exhibit an overall negative permeability. NiO has $\varepsilon \sim 5$ at high frequency [20], but the dielectric constant of $SrTiO_3$ can approach $\varepsilon_r \sim -100$ near the resonance [18], so the system should also exhibit an overall negative permittivity. The actual values obtained depend on the linewidth of the resonance, which is affected by doping conditions, temperature and crystal quality.

1.3 Introduction – Combinatorial Oxide Thin Films

Oxide thin films are used in a variety of systems and applications. Oxides exist as dielectric materials, magnetic materials and semiconductor materials among other material types. The material properties of these materials can be changed in a variety of ways through changing the composition of the material.

Studies of composition effects in thin films can be long and tedious using standard techniques that require a new deposition for each composition (and often a new source as well). In order to systematically study the effects of composition on oxide materials, several high-throughput combinatorial techniques have been devised.

One such technique [28] was used to systematically study the effect of dopant concentration in ZnO as a transparent conducting material. This technique allows for a robust method of studying changes in composition in ZnO with a single deposition. This technique will be further discussed in Chapter 2.

1.4 ZnO as a Transparent Conducting Oxide

1.4.1 Transparent and Conducting

Material that are both transparent to optical wavelengths and have high electrical conductivity are vital for many applications. Reports of transparent conducting (TC) films appear to date back to the 19th century [29]. These first TC films were coatings of silver, gold or platinum that was thin enough to let some amount of light through. These films had limited use and were only used for a few niche industries. TC films first became truly viable for manufacturing use when wide band-gap materials such as SnO_2 were considered. Transparent conducting oxides (TCOs) were first used for defrosting windows on airplanes. SnO_2 was a major key to allowing high altitude bombing during World War II [30] and is still a major component in many functional glass applications. There has been a lot of research on TCO materials summarized in many reviews [29-40]. Indium tin oxide (ITO), typically 90% In_2O_3 10% SnO_2, has now become the most used TCO in applications such as photovoltaics and flat panel displays (FPD). Many new materials are on the horizon, including ZnO.

TCO materials have become the main class of materials for TC applications for a couple key reasons. Althought thin metal films were used initially as TC materials, they had to be very thin to allow any reasonable amount of light through. A common figure of merit (Φ) for a TC material is given by [29]:

$$\Phi = \frac{T^{10}}{R_s} \tag{1.11}$$

Where T is the optical transmission and R_s is the sheet resistance. The exponent on the optical term is high in order to balance the electrical and optical properties in a more useful way. For metals, in order to keep T high, the film must be very thin, which greatly reduces R_s.

The solution to this problem was to use wide band-gap materials. Many wide-gap materials are oxides, which leads to the term TCO. In order to be useful, the material should have a band-gap larger than the largest energy of light for the given application. This corresponds to about 3.1 eV gap for 400 nm light. A useful TCO must also be easily degenerately doped. This is not always trivial; many donors and acceptors for these materials tend to have deep energy levels. Also, point defects such as vacancies or interstitials can compensate for any extrinsic dopant. At this time, the most common TCO materials are In_2O_3, ITO, SnO_2, ZnO and CdO. The majority of the research in searching for new TCO materials has focused on binary and ternary oxides of these materials [41-49].

The other optical property that one must consider is the plasma edge. The plasma edge is highly correlated with the electrical properties and is often used as a measure of the carrier concentration of the material. The plasma frequency ω_p is given by Drude's theory of electrons as:

$$\omega_p = \left(\frac{4\pi N e^2}{\varepsilon_0 \varepsilon_\infty m_e^*} \right)^{1/2} \tag{1.12}$$

where ε_0 and ε_∞ are the dielectric constant of the material and the dielectric constant of free space. N is the carrier concentration, e is the charge of an electron and m_e^* is the effective mass of the carriers. Although ω_p is a function of the material through the effective mass and dielectric constant, the frequency for a given material shifts as a function of $N^{1/2}$. For a metal, the plasma frequency is in the optical frequencies making the metal reflect optical light. For a good TCO, the plasma edge must be in the

infrared. The plasma edge can be used to estimate the carrier concentration optically. The plasma edge is also the property of primary importance in many applications such as low-emissivity glass.

1.4.2 Applications of transparent conducting oxides

TCO materials are vital to many industries today. There are many comprehensive reviews of TCO applications [30,37,40]. Some of the most important applications for TCO materials are functional glasses, photovoltaics, FPDs and other optoelectronic devices.

The term functional glass includes glasses for a wide range of uses. They are typically structural glasses that utilize the electrical properties of the TCO material to gain a function. Along with defrosting windows as mentioned before, one of the most common examples is a low-emissivity glass. In this application, the TCO is designed to have a plasma edge that is around or less than 1000 nm. This allows the glass to be transparent to visible light while reflecting the infrared radiation. These low-emissivity glasses are used as window glass to keep heat inside buildings in cool climates, heat outside in warm climates or even to keep the outside of oven door windows cool. Cost, transparency and chemical stability are the main TCO requirements for functional glasses with less of a requirement on electrical conductivity. SnO_2 has been the main TCO material for these applications.

Although functional glasses and other applications are important, the two applications that are driving much of the TCO research are FPDs and photovoltaics. All FPD technologies require TCO materials as front electrodes. These materials must combine the highest transparency with the highest conductivity. Although highly doped silicon is often used as a top electrode for single crystalline silicon solar cells, most other solar cell technologies require a TCO material. The efficiency of these solar cells will of course be highly dependent on the transparency of the TCO along

with the conductivity. Only the best TCO materials are viable for most of these applications. ITO has been the standard TCO material for high-end applications such as photovoltaics and FPDs. Much of the research in TCO materials has involved the search for a replacement for ITO, which has become a very expensive material.

One could also imagine a vast array of applications if transparent electronics could become a reality. These applications require pn junctions in transparent materials. This has been difficult dut to the non-symmetric doping of wide band-gap TCO materials. There has been a vast amount of research in recent years attempting to obtain better transparent electronics. Much of the work has focused on achieving p-type ZnO to match the relatively easily obtained n-type ZnO [36, 50-57]. A lot of research has also gone into obtaining good interfaces between n-type ZnO and a second p-type material such as GaN.

1.4.3 Search for an ITO replacement

The current standard material for FPDs and many photovoltaic devices is ITO. Standard ITO contains about 80% indium and 20% tin. ITO can easily be made highly conductive ($<10^{-4}$ Ω.cm) with an absorption coefficient of less than 0.05. ITO is also highly stable, both chemically and thermally. This fulfills the requirements for FPDs and photovoltaics. ITO has been found to be an excellent material for high-end electronic devices.

The problem with ITO has to do with its cost. The supply of indium results from mining of other metals such as zinc, tin, copper or iron. Indium is a byproduct of many ores of these metals. The fact that indium is a byproduct of other manufacturing and does not have a significant ore of its own means that the supply is essentially fixed. Due to the increased demand of indium from increased FPD manufacturing, the price of indium has increased significantly in recent years. Accoring to EconStats [58], the price for indium was leass than $100/kg in 2002. By 2006, the price had increased

to more than $980/kg. Without a significant increase in supply, the price is expected to continue to climb as demand increases. There is a strong desire to find a TCO material that has the stable optical and electrical properties of ITO without relying on large amounts of indium.

Of the commonly known TCO materials, SnO_2, ZnO and CdO are the most commonly studied as replacements for ITO. So far, SnO_2 has not shown conductivities that are sufficient to be used in FPD or future photovoltaics. CdO has shown promise, however research on CdO has been limited due to the highly toxic nature of Cd. ZnO is still thought to be a promising choice due to conductivities that approach ITO along with excellent optical transparency. ZnO has not been used widely as a replacement for ITO due to poor electrical stability at elevated temperatures needed in subsequent processing in FPD or photovoltaic applications. In general, there is a relatively poor understanding of the doping mechanisms in ZnO. The role of the point defects and hydrogen defects is a much-debated topic in regard to ZnO.

There have also been many studies searching for new TCO materials [42-49]. The majority of these studies have involved binary and ternary oxide compounds of Sn, Zn, In and Cd. Although there have been promising leads, there has been little follow-up in order to understand the materials found. In general, it is expected that binary and ternary oxides will result in more difficulties in understanding and controlling point defects.

1.4.4 ZnO as a transparent conductor

ZnO is a leading candidate for replacement of ITO as a high-end TCO material. ZnO has been studied extensively for many years and several reviews have been published [59-61]. Although ZnO studies have shown many successes, there is still a relatively poor understanding of some aspects of the material. ZnO is typically n-type even without intentional doping. This has also led to some difficulty in

achieving p-type ZnO. There is much debate as to what the source of n-type carriers is in ZnO and how they can be controlled. History has suggested that point defects such as zinc interstitials [62-65] or oxygen vacancies [66-69] are the source, while some recent work has suggested that it is all due to unintentional hydrogen doping [70-78]

ZnO has been chosen as a possible ITO replacement due to several important properties. ZnO is a particularly cheap alternative to ITO. ZnO has a direct band-gap of about 3.2 eV, which is near ideal for TCO applications. ZnO has the wurtzite structure and can be grown with relatively large grain size even at moderate deposition temperatures. The structure also allows for a wide range of dopant materials. High conductivity n-type ZnO has been achieved through doping [79-83] with B, Al [84-105], Ga [106-110], In [111-116], Ag [117], rare earth [118] and other dopants. There have also been some studies that suggest that p-type ZnO is possible [36, 50-57]. Finally, ZnO is easily etched, which allows for relatively easy patterning for device structures.

There are still a few drawbacks to using ZnO at this time. First, although conductivities have approached those of ITO, they are not quite as good and are only achieved using extreme care and precision in processing. Second, the best conductivities do not tend to be stable even at moderate temperatures in the presence of air or humidity. This makes high conductivity ZnO an extreme difficulty using current manufacturing techniques for fabrication of FPDs, which require several subsequent high temperature processes. This also raises questions of reliability of ZnO based devices.

One cause of the poor stability of ZnO electrical properties comes from the source of carriers. Essentially all of the high conductivity ZnO has been achieved with great care to control point defects. In particular, most films are deposited or annealed in the presence of hydrogen. The hydrogen has been thought to act as a reducing

agent, which keeps the oxygen level in the film low. There have been many studies that have correlated the presence of oxygen vacancies [66-69], or zinc interstitials [62-65] with the carrier concentration in ZnO. More recently, density functional theory calculations suggest that hydrogen acts exclusively as a donor in ZnO, either as an interstitial or even as a substitutional dopant [70-73]. The presence of hydrogen and the correlation with electrical properties has been shown experimentally as well [74-78]. This suggests that the best ZnO conductivities are a result of not only the extrinsic dopant (Al, Ga, In for example), but also point defects such as oxygen vacancies, zinc interstitials or hyrdrogen. These defects have high mobilities and can be annealed out, reducing the conductivities. For example, interstitial hydrogen has been shown to be removed rapidly at temperatures as low as 150 ºC [78] substitutional hydrogen is thought to remain stable at higher temperatures.

There is a strong desire to achieve ZnO with a conductivity that approaches the conductivity of ITO and does not require high temperature annealing in reducing gases such as hydrogen. To achieve this will require higher activation of extrinsic dopants without also relying on point defects and hydrogen to act as sources of carriers. This requires increasing the solubility of an extrinsic dopant in order to decrease the amount of dopant precipitating out in a second phase. We propose to do this thorough codoping. Doping with more than one extrinisic dopant might lead to increased total dopant solubility.

Two of the most commonly used dopants for ZnO are Al and In. Zn^{2+} has an ionic radius of 0.074 nm while Al^{3+} has an ionic radius of 0.05 nm and In^{3+} has 0.081 [119]**.** These large mismatches of -32% for Al^{3+} and +9% for In^{3+} can lead to large strain in the lattice. We anticipate that codoping with both Al^{3+} and In^{3+} should allow for higher total dopant solubility and activation along with improved crystal quality even for low temperature depositions without the need for high temperature annealing.

This could lead to the improved electrical properties and stability needed to replace ITO. It could also lead to a material that could be used as a high quality TCO for applications that require a low thermal budget, such as TCO films deposited on polymer substrates or films. A combinatorial technique such as off-axis cosputtering is an excellent method to test this hypothesis.

CHAPTER 2

EXPERIMENTAL METHODS

2.1 Introduction

High throughput combinatorial techniques are often used to quickly examine a large number of parameters in a system. They may be used to study how properties change with a number of variables such as composition, temperature, deposition rates and many other process parameters. One such method used to combinatorially examine a large region of composition space uses co-sputtering from two or more off-axis sputter sources [28]. A variety of oxide thin film systems have been studied successfully using this technique. This technique has been used to study Al and In doping in ZnO and may be used in the future to study the effect of doping on resonance frequencies of materials such as SrTiO3 or NiO.

The high throughput deposition chamber is a small part of a combinatorial study. In order to fully utilize a combinatorial deposition technique, high throughput measurement techniques must be established to measure the desired properties in a reliable way. For the systems of interest here, these techniques include x-ray diffraction to determine atomic structure, optical spectrometry to determine transmission, reflection and absorption, four-point probe to determine sheet resistance along with other common techniques.

2.2 Combinatorial Technique Using Reactive Off-Axis r.f. Cosputtering

Off-axis sputtering is a method of sputtering that places the substrate at an angle relative to the sputter source. In particular, if the angle between the sputter source and the substrate is 90°, the deposition rate on the substrate will be a well-behaved function of the distance from the sputter source. In the direction perpendicular to the sputter source (i.e. the sputter direction), an exponential decay

function serves as a good empirical fit for the deposition rate as a function of distance from sputter source.

$$R(x) \approx b \cdot \exp\left(\frac{x - x_0}{d}\right) \tag{2.1}$$

R(x) is the change in thickness per unit time and is defined as the deposition rate. The constants b and d depend on the system of interest, which includes pressure and sputter source power among other parameters. Figure 2.1 shows the deposition rate of ZnO on Si as a function of distance on the substrate measured optically. The fit to this data is very good allowing us to model the deposition rate with a simple function even without an underlying theoretical basis.

Equation 2.1 can be extended easily to include a full 2 dimensional substrate. This is needed when depositing ternary composition spreads. Equation 2.1 can be extended as an exponential ellipsoid:

$$R(x, y) \approx b \cdot \exp\left(\frac{-\sqrt{(x - x_0)^2 + c(y - y_0)^2}}{d}\right) \tag{2.2}$$

In this equation, c is a term that accounts for the fact that the sputter source is not a point source. Figure 2.2 shows the optically measured thickness of ZnO on a silicon wafer. This is compared to the least squares fit for Equation 2.2. As can be seen, there is excellent fit to the data. In general, c is found to be about 0.7 for the deposition chamber. If the deposition parameters are similar to previously examined systems, c can be assumed to be 0.7 and a line scan along x is all that is needed to determine the deposition rate with good accuracy.

A combinatorial technique can then be devised that has three independent 90° off-axis sputter sources located at 90° to each other as in Figure 2.3. Each source is independent thus allowing for individual rate control from each source. Each source has a rate profile given by Equation 2.2. When cosputtering from each source simultaneously, the resulting film will be a superposition of the three sputter sources.

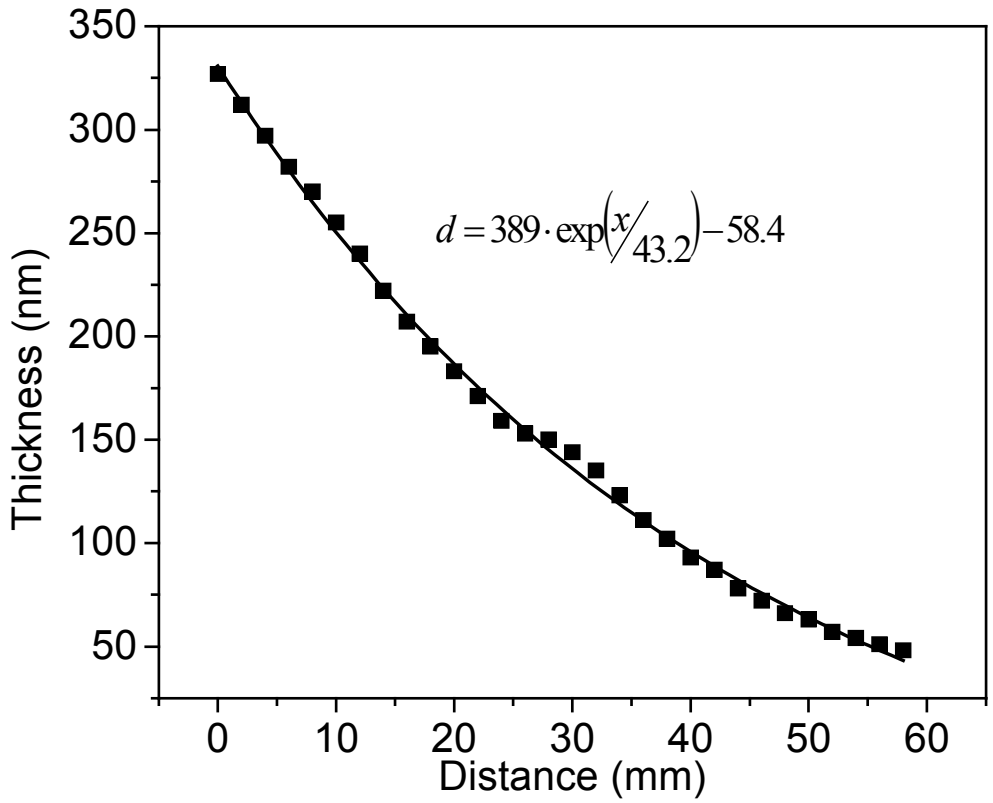

Figure 2.1: Thickness of ZnO measured optically as a function of distance on a substrate. The fit is a simple exponential decay function with excellent match to data.

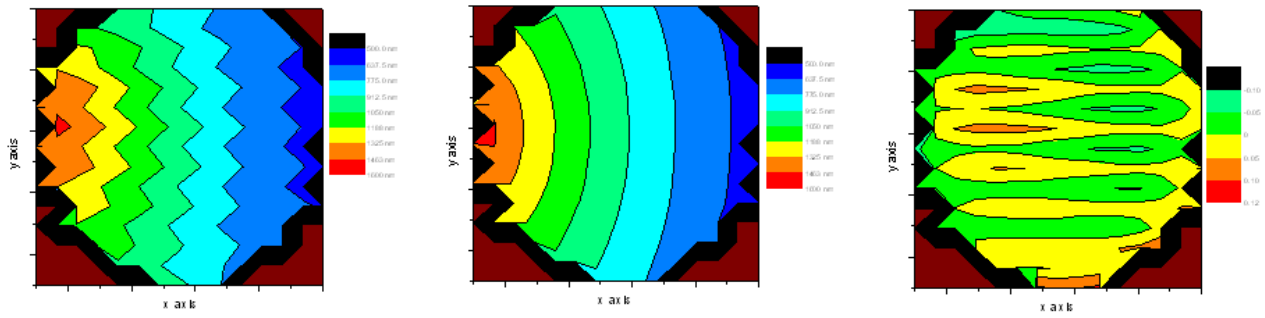

Figure 2.2: (a) Thickness of ZnO measured optically as a function of distance on a Si substrate. (b) Exponential ellipsoid fit to measured thickness (c) The percent error of fit to experimental data. The error is less than 10% for the entire substrate.

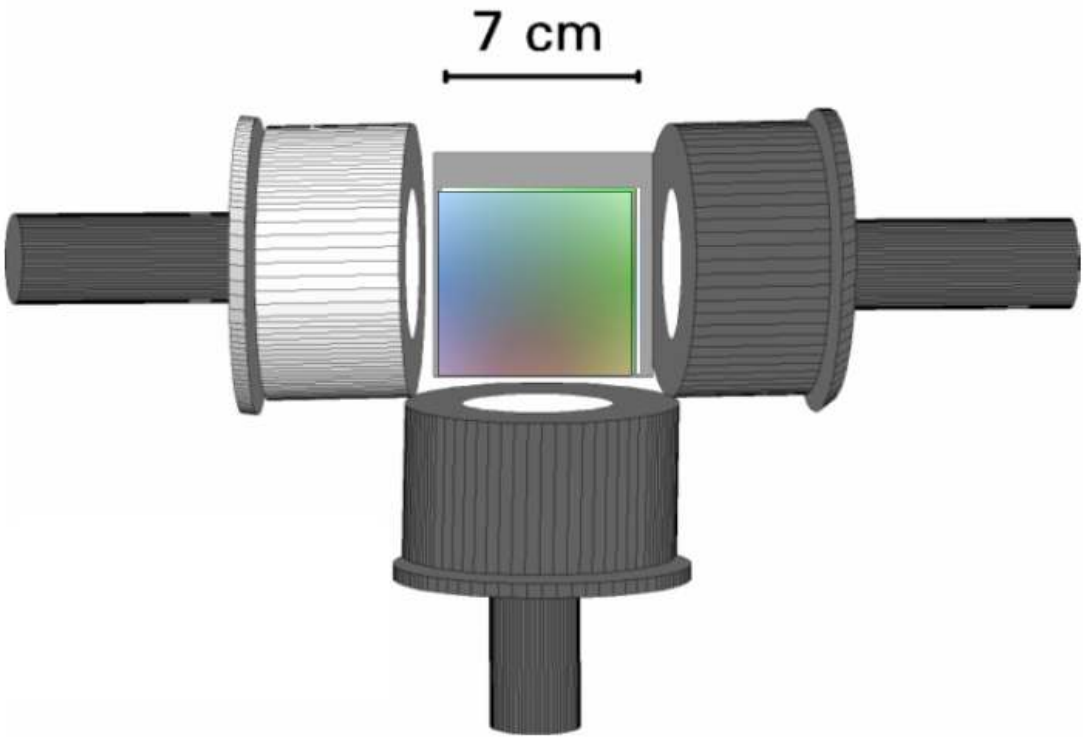

Figure 2.3: Off-axis cosputtering system used to make high-throughput combinatorial composition spreads. Cosputtering from two or three independent sputter sources results in a range of composition on a single substrate.

This means that the composition on the substrate is a function of location on the substrate.

The system also contains a fourth sputter source that is located on axis to the substrate. This source is typically a larger 4 inch sputter source. This source is used to obtain a uniform film with less than 10% variation in thickness possible. Figure 2.4 shows an example film thickness of a ZnO film deposited from a 4-inch Zn target in 5% oxygen as a function of distance. The 4-inch source was placed in a location as close to the source as possible in order to get the highest rate possible for a given sputter power. Figure 2.4 shows that the variation in thickness is about 10% for this film. It is possible to improve on this uniformity by increasing the distance between the sputter source and the substrate. The 4-inch sputter source is most useful for composition spreads in which it is desired to have one element constant and be the majority of the film, such as studies of doping in semiconductors.

There are several known issues that must be considered when using the on-axis source. First is the poor uniformity. Although reasonable uniformity in thickness is possible, the film can receive non-uniformity due to variation in ion bombardment. This is typically a radial effect due to the highest sputter rate coming from the target racetrack. This will effect will likely have some effect on the structure of the film. This can be seen in Figure 2.4 through the film resistivity. Although the thickness varies by only about 10%, the two-point resistance varies by more than an order of magnitude. In looking closer, the resistance increases on the substrate at locations that correspond with the sputter source racetrack. Although other systems might not be as sensitive to small changes in deposition conditions as this system, this non-uniformity in ion bombardment must be considered in all systems.

There is also strong evidence that the large 4-inch gun interacts with the other sputter sources. There appears to be a stronger effect when using a pulsed DC power

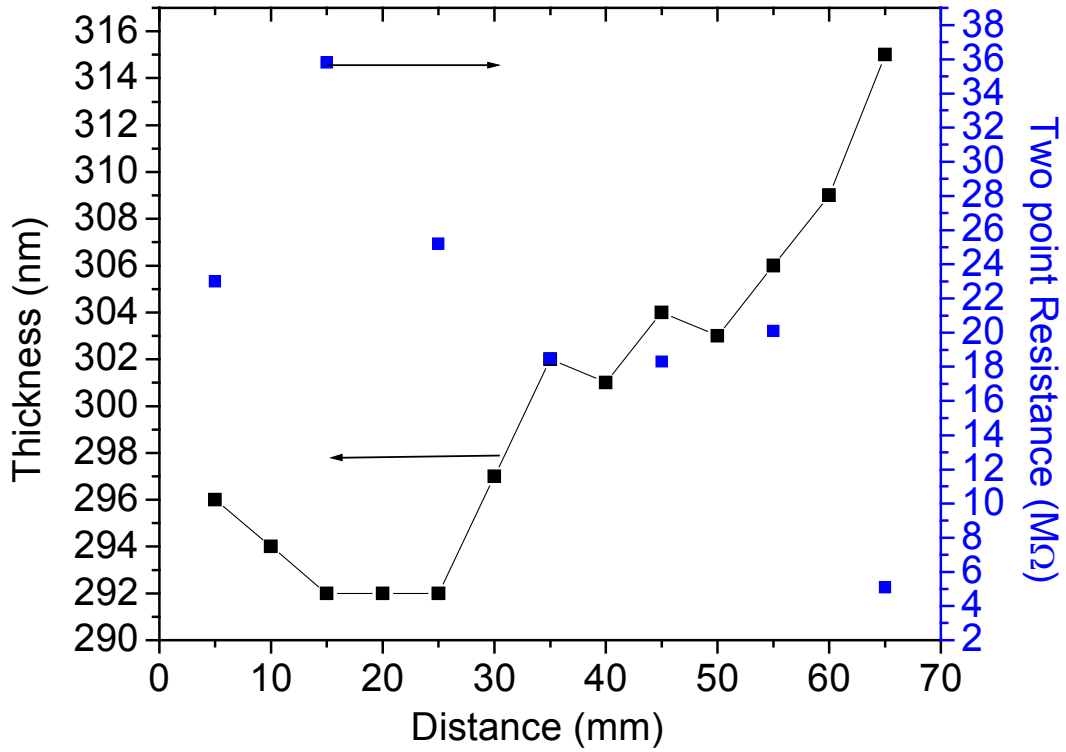

Figure 2.4: The two point resistance times the thickness of a ZnO film deposited on-axis from a 4-inch sputter source on a microscope slide as a function of location on substrate. The resistivity varies by an order of magnitude with two peaks (15 mm and 55mm) corresponding to the middle of the sputter source racetrack.

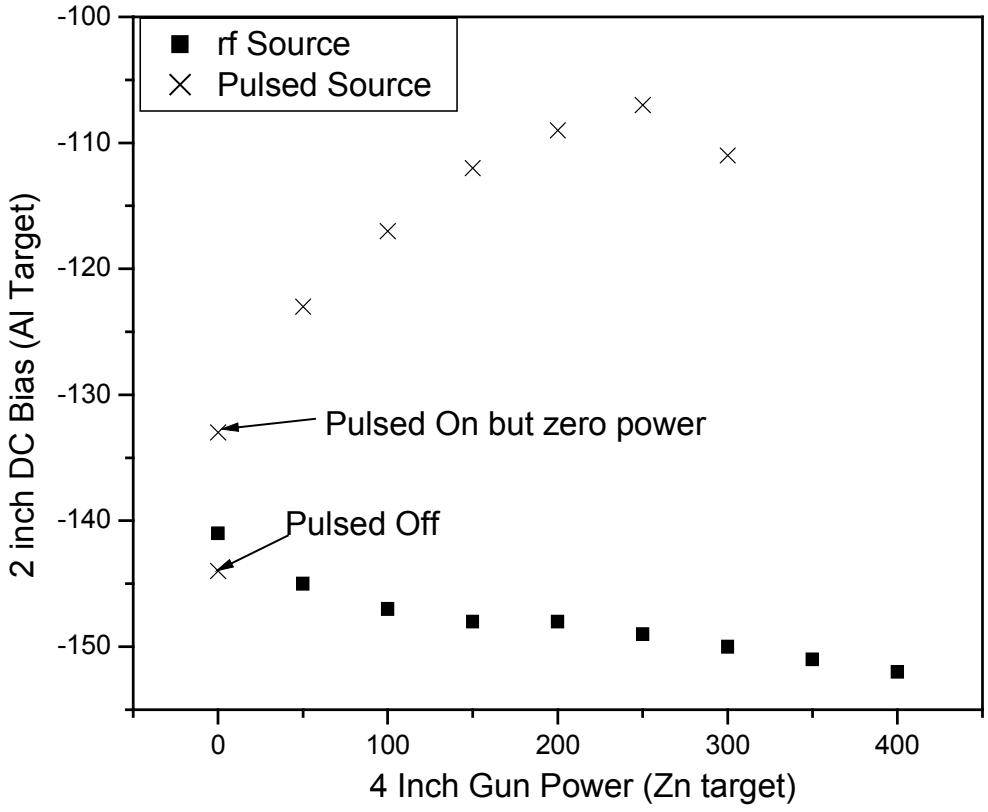

Figure 2.5: The DC bias of a 2-inch sputter source with an Al target and 100 W r.f. power as a function of sputter power on the 4-inch on-axis sputter source. Some level of interference is seen in the DC bias of the 2-inch source. This effect is larger when using a pulsed DC source for the 4-inch sputter source.

supply rather than an rf source. Figure 2.5 shows the DC bias of one of the 2 inch sputter sources with an Al target at 50 W as a function of power to the 4 inch sputter source with a zinc target. A significant decrease in the magnitude of the dc bias is obvious. This can lead to less Al in the Al:ZnO film than would be expected from deposition rates. It is interesting to note that the trend is opposite and smaller when using an rf source for the 4 inch sputter source. For this reason, a second independent method of determining composition in a cosputtered film other than deposition rates must be used.

2.3 High-throughput Measurement of Composition Spreads

2.3.1 X-ray Diffraction with GADDS

The Bruker AXS with General Area Detector Diffraction System (GADDS) uses a two-dimensional detector to achieve a combinatorial approach of examining a range of 2θ and θ [120]. Figure 2.6 shows a schematic of the system. Figure 2.7 shows the output for a polycrystalline corundum sample used as a calibration standard. The sample is polycrystalline and therefore each powder diffraction cone 2θ intersects the two-dimensional detector as a hyperbola. For a single crystal sample, the result will be spots located at the correct geometry. Textured thin films will be somewhere in between. The GADDS system allows for a quick method to locate single crystal diffraction peaks. Pole figures (rotation of ϕ) and rocking curves (vary ω) can be completed to quantify crystal quality.

2.3.2 High throughput optical measurements

Optical measurements are very useful for rapidly obtaining many material properties of thin films. These properties include optical quantities such as refractive index and absorption coefficient, band-gap and plasma frequency. From spectral data, one can also determine the thickness of the film for reasonably thick films. We have

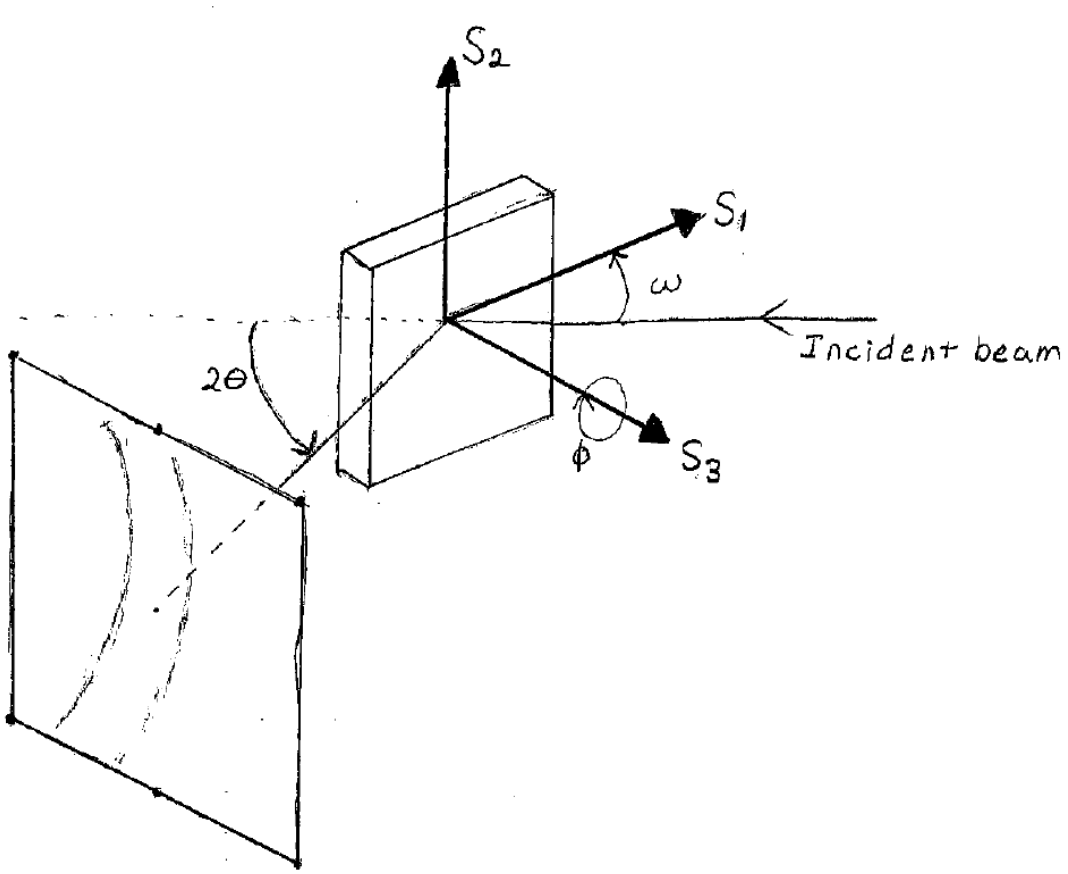

Figure 2.6 Schematic of x-ray diffraction system with two-dimensional detector.

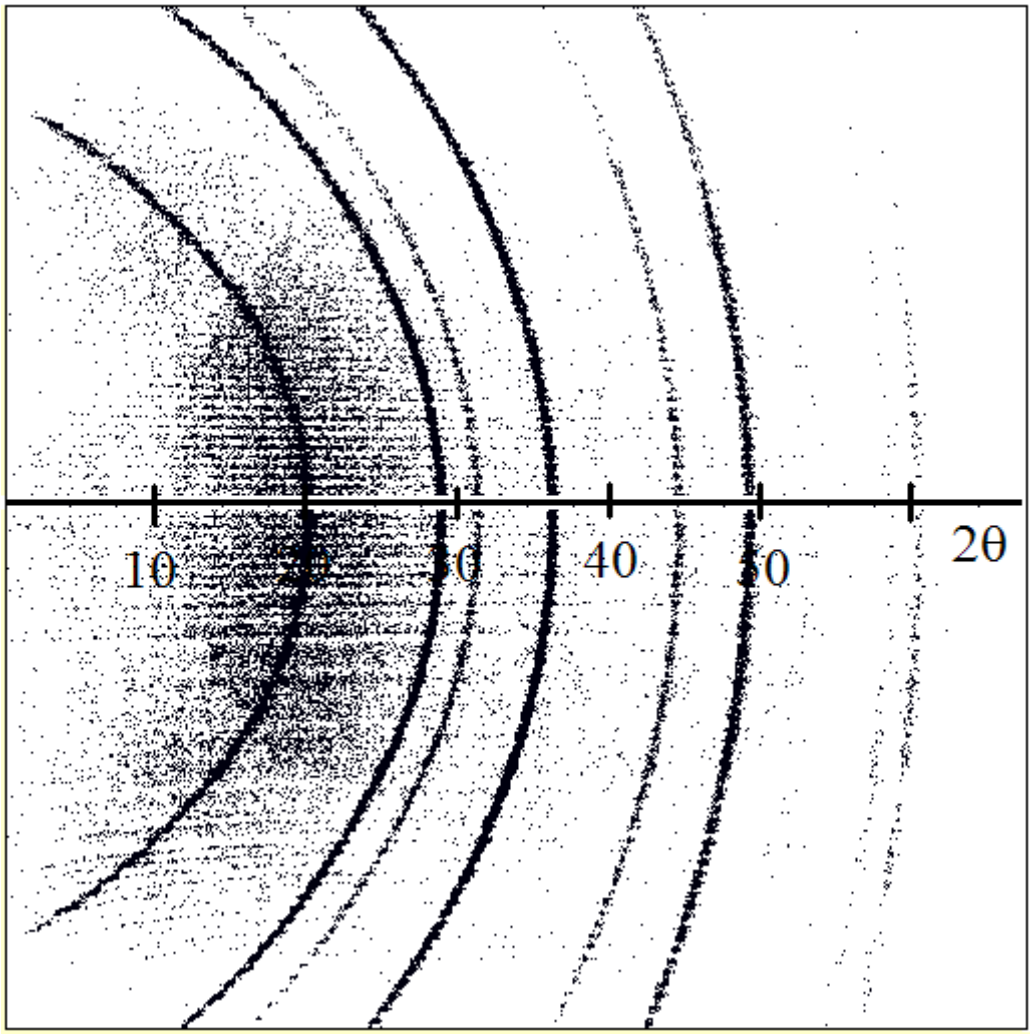

Figure 2.7: Output of Bruker GADDS for a polycrystalline corundum sample. The arcs at a given 2θ occur due to the intersection of diffraction cones with the 2D detector.

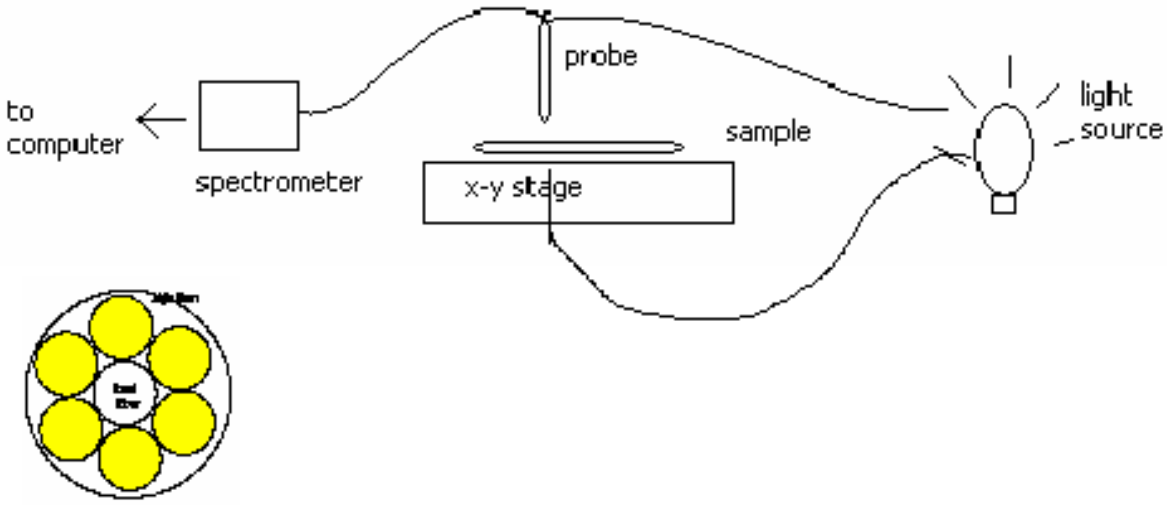

Figure 2.8: Optical apparatus used for measuring optical reflection and transmission of thin film composition spreads.

developed an optical measurement apparatus (Figure 2.8) that involves an x-y stage for rapid measurements of thin film composition spreads. This apparatus uses an Ocean Optics USB2000 Spectrometer with measurement capability between 340 – 1050 nm. At this time, the apparatus can be used for reflection or transmission measurements separately but not simultaneously. A second spectrometer would be needed for simultaneous reflection and transmission measurements.

Figure 2.9 shows the optical reflection for a standard mirror and for a ZnO film on Corning D-263 glass and the ZnO film reflection normalized to the mirror. Reflection measurements can be used to rapidly measure the films thickness and/or refractive index. The reflectivity R of a thin film of thickness d on a substrate is a function of the refractive index of the film n and of the substrate ns.

$$R(n,d,\lambda)=\frac{r_1^2+r_2^2+r_1r_2\cos\left(\frac{4\pi}{\lambda}nd\right)}{1+r_1^2r_2^2+2r_1r_2\cos\left(\frac{4\pi}{\lambda}nd\right)} \tag{2.3}$$

where r_1 is the Fresnel coefficient for the film/air interface and r_2 is the Fresnel coefficient for the substrate/film interface.

$$r_1=\frac{1-n}{1+n} \qquad r_2=\frac{n-n_s}{n+n_s} \tag{2.4}$$

There is a similar equation that one can use for fitting to the transmission T as a function of d, n and n_s.

$$T'=\frac{T}{T_{sub}}=\frac{\left(\frac{t_1}{t_{sub}}\right)^2 t_2^2}{1+r_1^2r_2^2-2r_1r_2\cos\left(\frac{4\pi}{\lambda}nd\right)} \tag{2.5}$$

where t1, t2 and tsub are given by:

$$t_1=\frac{2}{1+n} \qquad t_2=\frac{2n}{n+n_s} \qquad t_{sub}=\frac{2}{n_s+1} \tag{2.6}$$

Equations 2.3 and 2.5 assume that the film is transparent with $\alpha = 0$. This is often a reasonable assumption for oxide materials for wavelengths greater than the

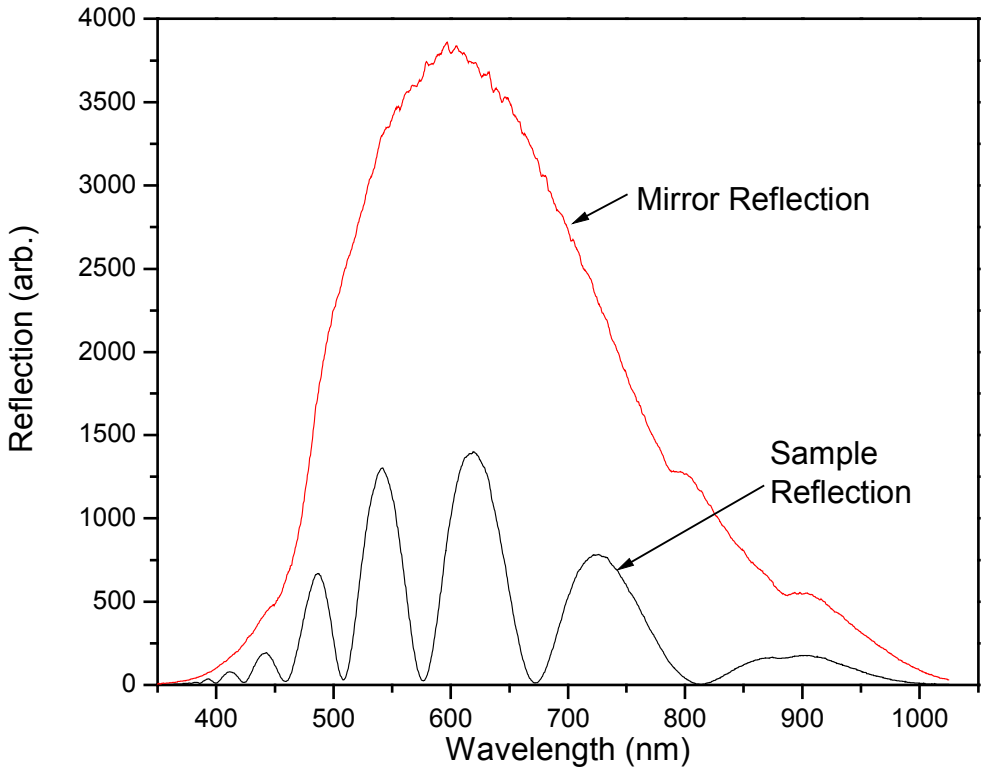

Figure 2.9: The optical reflection of the source from a standard (mirror) and a thick ZnO film on Corning D-263 glass.

band-gap. These equations will not be valid for any material that has a large absorption coefficient. One can typically assume absorption is small and the n is approximately constant with wavelength for wavelengths that are much greater than the band gap.

If the assumptions that absorption is small and that the refractive index is approximately constant are valid, one can easily determine the refractive index and thickness of a thin film using Equation 2.3. For a film that has $n>n_s$, the minimum resistivity R_{min} depends only on the refractive index of the substrate.

$$R_{\min} = \frac{r_1^2 + r_2^2 + 2r_1r_2}{1 + r_1^2r_2^2 + 2r_1r_2} = \frac{(n_s - 1)^2}{(n_2 + 1)^2} \neq f(n,d) \qquad n > n_s \qquad (2.7)$$

Similarly, if $n < n_s$, R_{max} is only a function of the refractive index of the substrate.

$$R_{\max} = \frac{r_1^2 + r_2^2 + 2r_1r_2}{1 + r_1^2r_2^2 + 2r_1r_2} = \frac{(n_s - 1)^2}{(n_2 + 1)^2} \neq f(n,d) \qquad n < n_s \qquad (2.8)$$

Equations 2.7 and 2.8 can be used to verify the assumption that absorption is small and can be used to determine a correction factor for errors in normalization. Looking again at Equation 2.3, one can see that the amplitude of oscillations in the reflectivity curve only depend on n. If the film is thick enough to accurately determine a maximum and a minimum, n can be calculated explicitly. The thickness of the film can then be calculated by determining the phase term. A C++ program has been written that rapidly determines the refractive index and thickness from reflectivity data using this method.

If the film is not thick enough to get an accurate minimum and maximum, a C++ program has been written to determine the lowest residual error fit for n and d. Much of the work has focused on ZnO. ZnO has a band-gap of about 3.25 eV (350 nm) and has a large variation in refractive index near this value. For ZnO films, the

wavelength range used for data fitting has been 600nm to 1000nm. The change in refractive index is expected to be less than 5% (2.0 – 1.95). Figure 2.10 shows the calculated fit for the sample of Figure 2.9. It can be seen that for this sample, the fit is very good above 450-500 nm.

Although transmission measurements can also be used to calculate refractive index and thickness in a similar way to reflectivity, transmission data is most useful for measuring band-gaps. Figure 2.11 shows an example of two ZnO transmission data at wavelengths near the band-gap. At wavelengths lower than the band-gap, the transmission is very close to zero. In order to determine an accurate optical band-gap, one would plot $\alpha^{1/2}$ for an indirect gap or α^2 for a direct gap and extrapolate the linear region to α=0. The absorption coefficient α is given by:

$$T = T'e^{-\alpha d} \tag{2.9}$$

The value α^2 is plotted versus energy for the two samples in Figure 2.12. It can be seen that the extrapolated value for the direct band-gap of ZnO shifts to higher values for higher conductivity. This is due to higher carrier concentration leading to the well known Burstein-Moss shift [121].

The plasma edge is another material property that can be measured optically. At wavelengths above the plasma edge, the material becomes highly reflective. The plasma edge is related to the carrier concentration N.

$$\omega_p^2 = \frac{4\pi N e^2}{\varepsilon m_e^*} \tag{2.10}$$

This results in a second method to examine changes in electrical properties optically. Increases in carrier concentration can shift the band-gap to higher energy (lower wavelength) and the plasma edge to higher frequency (lower wavelength). The plasma edge for most wide band-gap materials tend to be greater than 1000nm, which leads to difficulty in measuring plasma edge with our current apparatus.

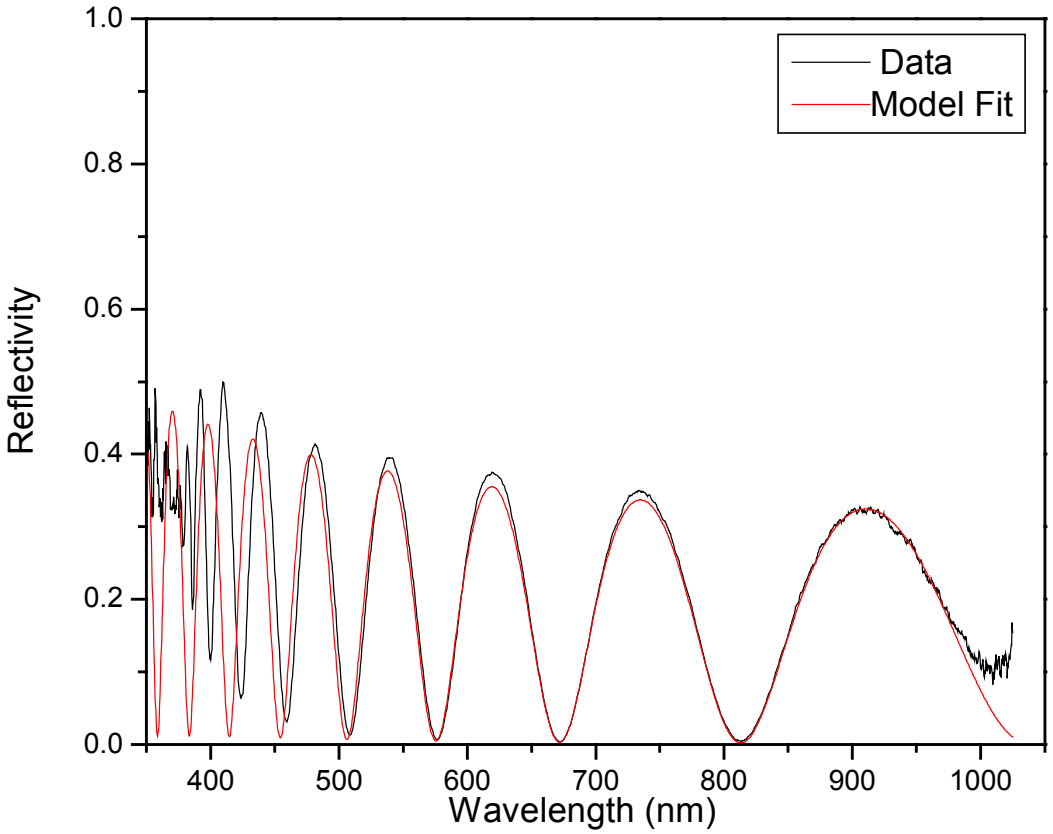

Figure 2.10: The normalized reflectivity from Figure 2.9 with the model fit from Equation 2.1. The fit is excellent above 450nm.

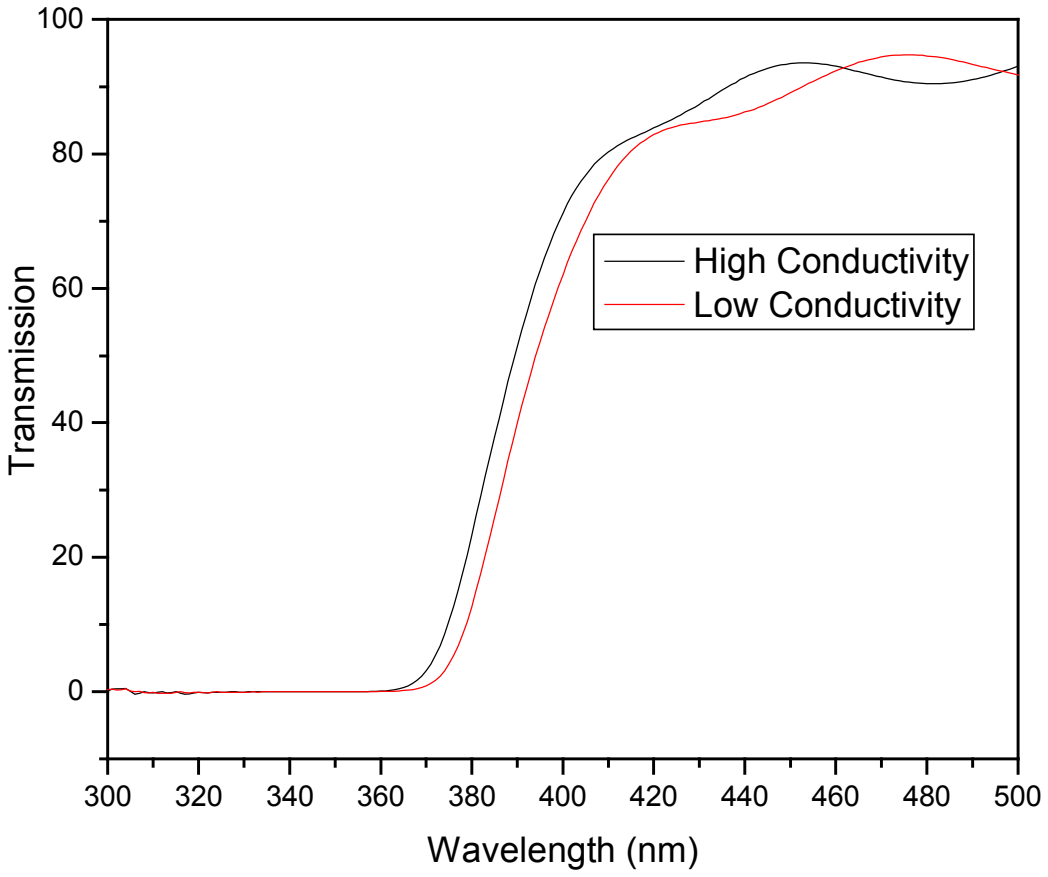

Figure 2.11: The optical transmission for two ZnO samples near the band-gap. The transmission drops for wavelengths below the optical band-gap. The band-gap shifts to higher energy (lower wavelength) due to the Burstein-Moss effect.

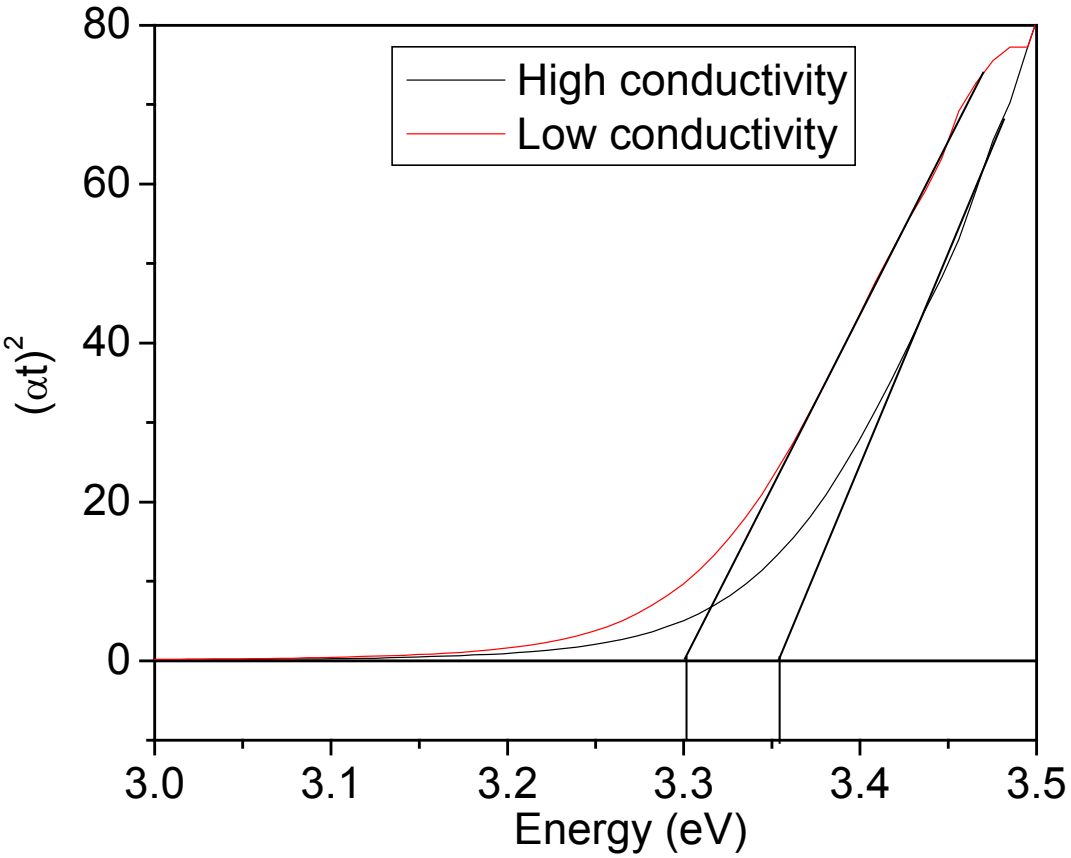

Figure 2.12: The square of the optical absorption as a function of energy. The linear extrapolation is used to estimate the value of the band-gap. The shift in band-gap to higher energy for the high conductivity film is due to the Burstein-Moss effect.

An optical apparatus that can measure reflection and transmission from ~350 – 1050 nm has been introduced. The x-y stage along with programming in C++ allows for high-throughput measurement of optical properties of thin film composition spreads. These measurements can be used to determine refractive index, film thickness, and optical band-gap rapidly. Further optical measurements can also be taken to higher wavelength to measure plasma edge.

2.3.3 High throughput resistivity measurements

There are two common methods of obtaining resistivity measurements of thin films. The first is a standard linear 4-point probe technique; the second is a 4-point measurement using the van der Pauw technique. Linear 4-point probe techniques are very easily used for high through-put measurements, while the van der Pauw technique is slower, but can easily be extended to measure the Hall coefficient. Both of these methods measure the sheet resistance Rs of the film, which is related to resistivity ρ by the film thickness *d*.

$$R_s = \rho / d \tag{2.11}$$

The first method of measuring sheet resistance is the linear (in-line) 4-point probe technique. In this method, four metal probes are spaced in a line of equal spacing as in Figure 2.13. A current is applied between the outer two probes and the resulting voltage is measured between the inner two probes. For a thin sample, the sheet resistance R_s is proportional to the voltage divided by the current.

$$R_s = k\frac{V}{I} \tag{2.12}$$

For an infinite sheet, $k = \pi/\ln 2$. This results from determining that the current will travel in circular current rings. This factor *k* will be different for non-ideal sample sizes and shapes and is termed the geometry factor. This method is a very rapid and fairly accurate method to determine the sheet resistance of a thin film.

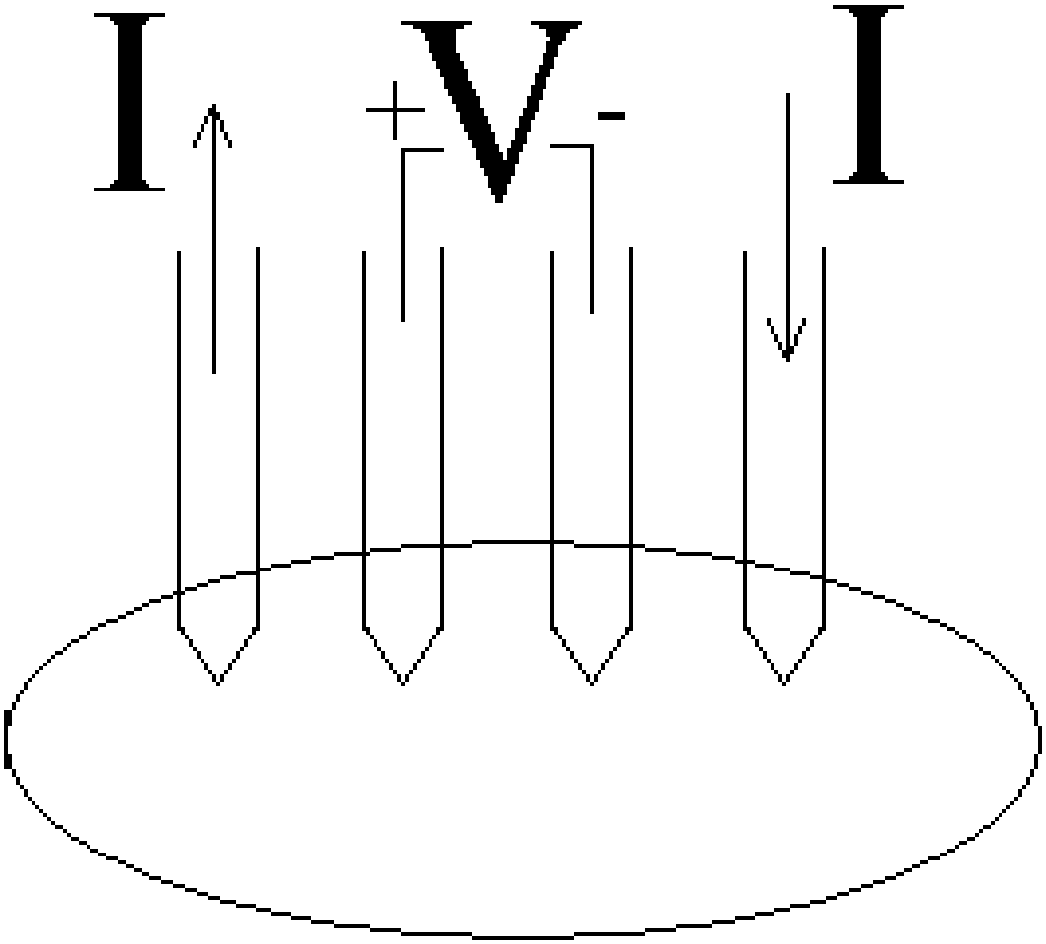

Figure 2.13: In-line four-point probe for sheet resistance measurements. A current is applied to the outer two probes. The voltage is measured between the inner two probes.

The van der Pauw technique is another common technique to measure the sheet resistance of thin films. This technique is particularly useful when used in combination with Hall measurements, which results in not only sheet resistance (resistivity), but also mobility, carrier concentration and carrier type. The van der Pauw technique is a four contact technique that can be used to measure flat films of any shape. Typically, the shape is chosen to allow for Hall measurements: cloverleaf, hall bar, etc. For the van der Pauw technique, the four contacts must be on the very edge of the film and must be very small. Any deviation from this results in error in the measurement. Cloverleaf patterns reduce the error from finite contact size. Figure 2.14 shows the simplest van der Pauw pattern with the contact labels.

The measurements needed to determine sheet resistance involve applying a current I_{12} from terminal 1 to terminal 2 and measuring the voltage V_{34} between terminals 3 and 4. For the second measurement, apply a current I_{23} from 2 to 3 and measure the voltage V_{41} between terminals 4 and 1. Two resistances can then be defined.

$$R_A = \frac{V_{34}}{I_{12}} \qquad R_B = \frac{V_{41}}{I_{23}} \tag{2.13}$$

The sheet resistance can then be found by solving:

$$\exp\left(-\pi \frac{R_A}{R_s}\right) + \exp\left(-\pi \frac{R_B}{R_s}\right) = 1 \tag{2.14}$$

This technique can easily be extended to include Hall measurements. In order to do this, a substrate holder was created that would place the sample with the contacts in a magnet for a vibrating sample magnetometer capable of fields up to 1.5 T. The sample is placed such that the field is perpendicular to the film surface. The Hall voltage can then be measured by, for example, applying a current I_{24} and measuring voltage V_{13}. An accurate value of the Hall voltage can be calculated by measuring each corner-to-corner Hall voltage with both polarities and with a positive and a negative

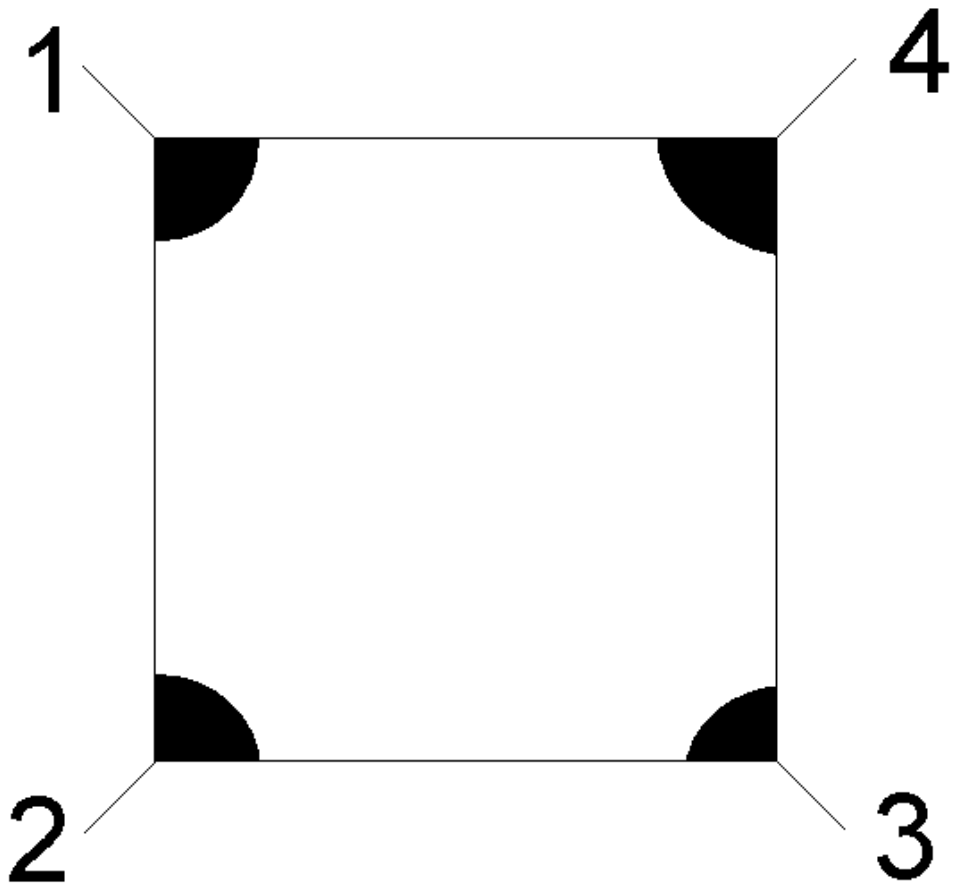

Figure 2.14: A standard sample with contacts for the van der Pauw technique. The contacts are labeled in a counter-clockwise fashion.

magnetic field. If the resulting Hall voltage V_H is positive, the material is p-type, if negative then n-type.

The Hall voltage can then be used to determine the carrier concentration and with the sheet resistance from Equation 2.14, the mobility. The carrier concentration is related to the Hall voltage by:

$$n = \frac{IB}{qd|V_H|} \tag{2.15}$$

The mobility μ is related to the Hall voltage and sheet resistance without any dependency on thickness.

$$\mu = \frac{1}{IBR_s} \tag{2.16}$$

In order to use the van der Pauw technique, each 2 to 3 inch sample must be diced up into smaller samples. For the work done here, the standard size adopted was 5 mm squares. In order to determine if this size was reasonable, a cloverleaf pattern was scribed into the sample. The variation in the electrical properties was found to vary less than 10% for cloverleaf patterns down to 1 mm. This suggests that the 5 mm square sample size is reasonable for measuring the electrical properties of composition spreads using the van der Pauw technique.

Two methods have been discussed for measuring electrical properties of conducting thin films. The in-line 4-point probe technique is a very rapid technique that is excellent for determining sheet resistance of composition spreads. The van der Pauw technique with Hall measurement is a relatively low throughput technique which requires dicing up a sample into small samples. This technique does allow for greater material understanding through separation of carrier concentration and mobility. This technique is very useful for combinatorial techniques due to the high reliability that results from composition spreads. The van der Pauw technique with Hall measurement is an excellent technique for discerning trends in a composition spread.

CHAPTER 3

EXPERIMENTAL STATUS OF ACHIEVING A NEGATIVE INDEX OF REFRACTION IN THE FAR-INFRARED

It has been proposed that it should be possible to achieve a negative index of refraction by combining an antiferromagnetic resonance (AFMR) with a dielectric resonance to achieve a negative index of refraction in the far-infrared. NiO has an AFMR at about 35 cm^{-1} (1.1THz) [20] and SrTiO3 has a dielectric resonance at about 100 cm^{-1} (3 THz) [18]. It has been shown in Chapter 1 how these resonance frequencies can be shifted. In order to verify this theory, two experimental techniques were attempted. First, a thin film heterostructure was grown with excellent crystal quality. This material could lead to a rapid method of studying the effect of dopants on the resonance frequencies of NiO and SrTiO3 using a composition spreads. The second method involves fabricating bulk ceramics through pressing of powders.

3.1 Epitaxial $(SrTiO_3/NiO)_n/MgO$ Thin Film Heterostructure

The deposition technique used in this work was reactive off-axis rf sputtering. This technique can later be used to deposit composition spreads like those in Chapter 2 in order to study the effects of doping on the resonance frequencies of NiO and $SrTiO_3$. One or two dc magnetron sputter sources (US Gun II) were oriented 90° off-axis with respect to the substrate. NiO films were sputtered reactively from an elemental Ni target with an r.f. power of 100W and the $SrTiO_3$ from a ceramic $SrTiO_3$ target with an r.f. power between 50 and 100W. The base pressure of the vacuum chamber was approximately 2×10^{-6} torr. The total pressure was held at 30 mtorr

during deposition. The composition of the sputter gas was 20 – 40% (by volume) O_2, balance Ar. Substrate temperatures from ambient temperature to 600°C were studied.

The films were deposited on single crystal (100) MgO substrates. The substrates were cleaned in acetone with an isopropyl alcohol rinse. Thermal contact between the substrate and heater was ensured using silver paste which was degassed in air by heating to 80 °C for 30 min followed by 180 °C for 30 min. The substrates were heated to 600 °C for 30 min in vacuum to remove any water adsorbed on the substrate and to ensure an atomically clean surface. The temperature was then brought to the desired deposition temperature.

3.1.1 Epitaxial NiO on MgO substrate

NiO films were grown with an r.f. power of 100 W with an oxygen partial pressure of 12 mtorr, argon partial pressure of 18 mtorr, and a target-to-substrate distance of 2.5 cm for various substrate temperatures ranging from room temperature to 600°C. These process parameters result in a deposition rate of about 18 nm/min. Film thickness ranged between 200 to 400 nm. The close lattice match between NiO films and the MgO substrate (~0.7% mismatch) makes x-ray diffraction analysis difficult using the GADDS system. The strong single crystal substrate peaks overloaded the detector making it difficult to resolve the NiO peaks from the MgO substrate peaks. However, the high sensitivity away from single crystal reflections did permit identification of any polycrystalline (nonepitaxial) material. The absence of such polycrystalline peaks either the film to be amorphous or a high quality single crystal.

Figure 3.1 shows the XRD results for depositions at temperatures of 200, 300, 400 and 600 °C. For this experiment, all samples were 400 nm thick. The *x* axis corresponds to 2θ, varying χ corresponds to the longitudinal direction of the beam. For a constant 2θ, varying χ corresponds to hyperbola (i.e. the intersection of the

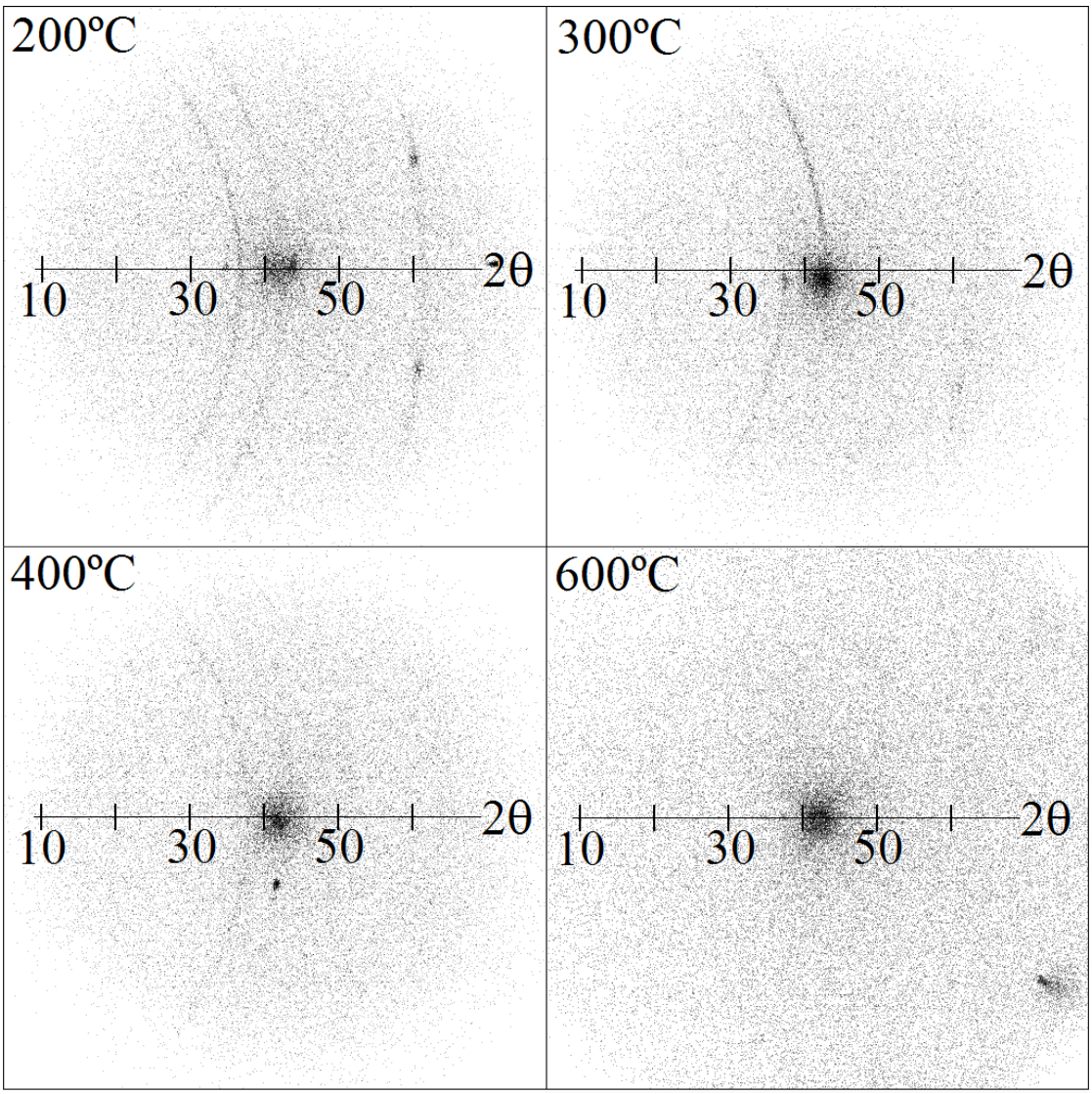

Figure 3.1: Effect of substrate temperature on crystal quality for NiO on MgO. The x-axis refers to 2θ in degrees. γ corresponds to the longitudinal location of the XRD peak and varies along constant 2θ values as hyperbola due to the intersection of XRD cones with the 2D detector. Arcs represent misoriented material. With a deposition temperature of 600°C, there is no evidence of misoriented material.

diffraction cone with the 2D detector). The streaks in the form of hyperbolas that are seen in Figure 3.1 correspond to misoriented material; single crystal material results in spots on the detector. It can be seen that there is significant texturing even at 200 °C as evidenced by spottiness in the arcs of constant 2θ, especially at 2θ~62°. For substrate temperatures >600 °C, there is no evidence of polycrystalline material. Furthermore, it can be seen in Figure 3.2 that when a sample deposited at 300 °C is post annealed at 1000 °C for 1 hr in air, the polycrystalline material is no longer evident.

Rutherford backscattering (RBS) channeling confirms that the films deposited at 600 °C or annealed at 1000 °C are, in fact, single crystals very well oriented to the MgO substrate. Figure 3.3 shows the channeling results for a sample deposited with 600 °C with no postanneal. The film thickness of this sample is approximately 400 nm. A χ_{min} of only 7% for the [100] channeling direction confirms that the NiO film has grown with high quality epitaxy since ion channeling is a stringent test of epitaxy. Modeling of the RBS data using RUMP software suggests that the film is stoichiometric with negligible diffusion occurring at the interface. Thus, we have demonstrated that NiO can be grown epitaxially as a high quality single crystal on an MgO substrate using reactive r.f. off-axis sputtering. This can be accomplished by deposition at a moderate substrate temperature or by low temperature deposition followed by a high temperature anneal.

3.1.2 Epitaxial SrTiO3 on MgO substrate

$SrTiO_3$ has the perovskite structure with a lattice constant of 0.39 nm, which represents a 7% lattice mismatch with MgO. The lattice mismatch leads to a high density of defects. This leads to a need for a high deposition temperature. The $SrTiO_3$ structure has a different symmetry compared to MgO, which allows for straightforward XRD analysis of the epitaxial relationship between the two materials. In particular, the (100) and (110) XRD peaks are strong for the perovskite while they

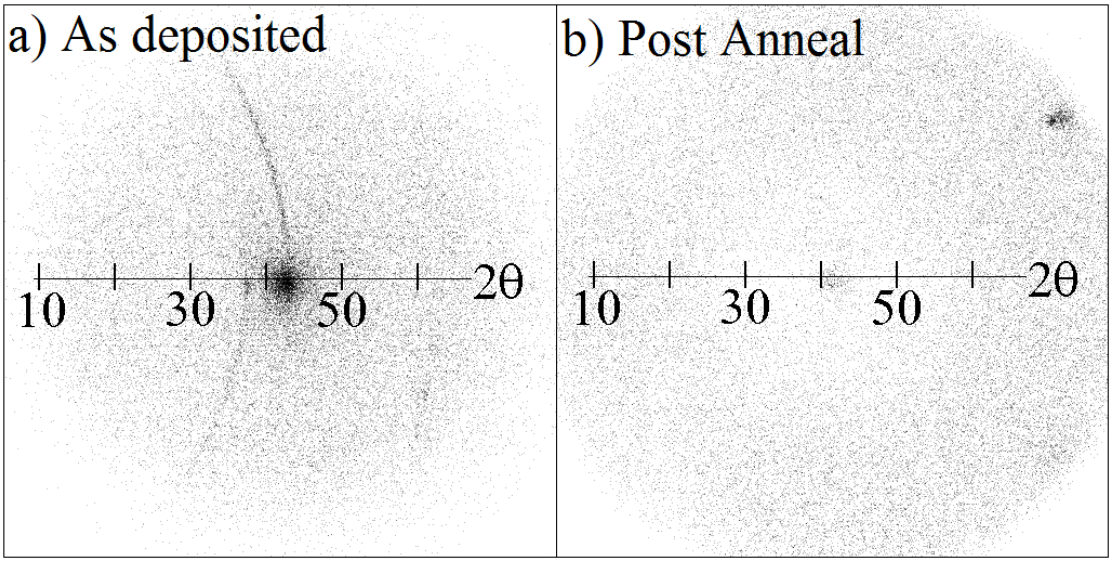

Figure 3.2: Effect of annealing at 1000°C for 1 hour in air on a NiO sample deposited at 300°C. Evidence of misoriented material disappears upon annealing.

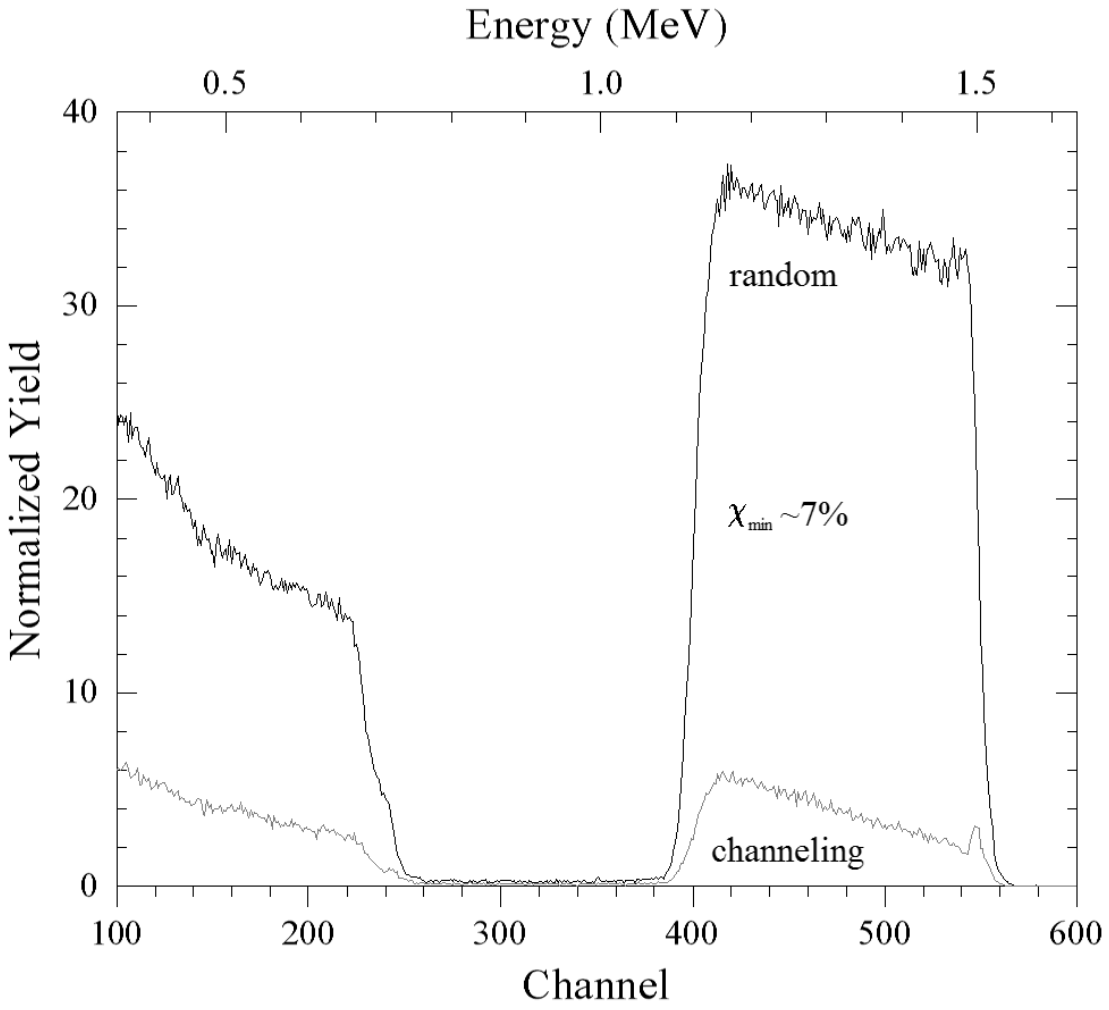

Figure 3.3: Ion channeling done with RBS in the [100] direction of a NiO thin film shows a χ_{min} of 7% for a sample deposited at 600°C. Film thickness was 400 nm. This is definitive evidence that the NiO is single crystalline.

are forbidden for the rocksalt structure.These diffraction peaks are not obscured by the substrate and therefore can be used to characterize the crystal quality.

Figure 3.4 shows the (100) rocking curve for a sample deposited at 600°C with and oxygen partial pressure of 12 mtorr, a r.f. power of 50 W, and a 2.5 cm target-to-substrate distance before and after a 1000 °C anneal for 1 hr in air. The deposition parameters resulted in a deposition rate of about 3 nm/s and the film thickness was 200 nm. The rocking curve is quite narrow with a full width at half maximum (FWHM) of 1.2°. The inset shows the (110) pole figure for the same sample after annealing at 1000 °C. The pole figure shows an excellent fourfold symmetry (as expected for rotation about the [100] axis) with essentially no misoriented material. These data confirm that the film is a single crystal grown with epitaxial orientation. Comparison with the substrate orientation reveals [100]||[100], i.e., cubic on cubic, as might be expected.

We found that a high deposition temperature and a low deposition rate were required to obtain the highest crystal quality in the system. At 600 °C, a deposition rate of less than 30Å/min and a postanneal at high temperature are required for the best crystallinity. Above this deposition rate, the crystal quality drops rapidly. Figure 3.5 presents the ratio of the intensity at the appropriate χ for the (110) peak ($\chi \sim 135°$) to the intensity at $\chi = 90°$ (equivalent to the standard planar θ-2θ diffraction geometry). This ratio increases as the crystal quality increases. It can be seen that the crystal quality decreases quickly and systematically with a deposition rate above 3 nm/min at a substrate temperature of 600 °C.

3.1.3 Epitaxial (SrTiO3/NiO)n/MgO thin film heterostructure

In order to fabricate a material with a negative index, it is necessary to achieve high quality crystal growth not only in a single film, but also on alternating layers. In

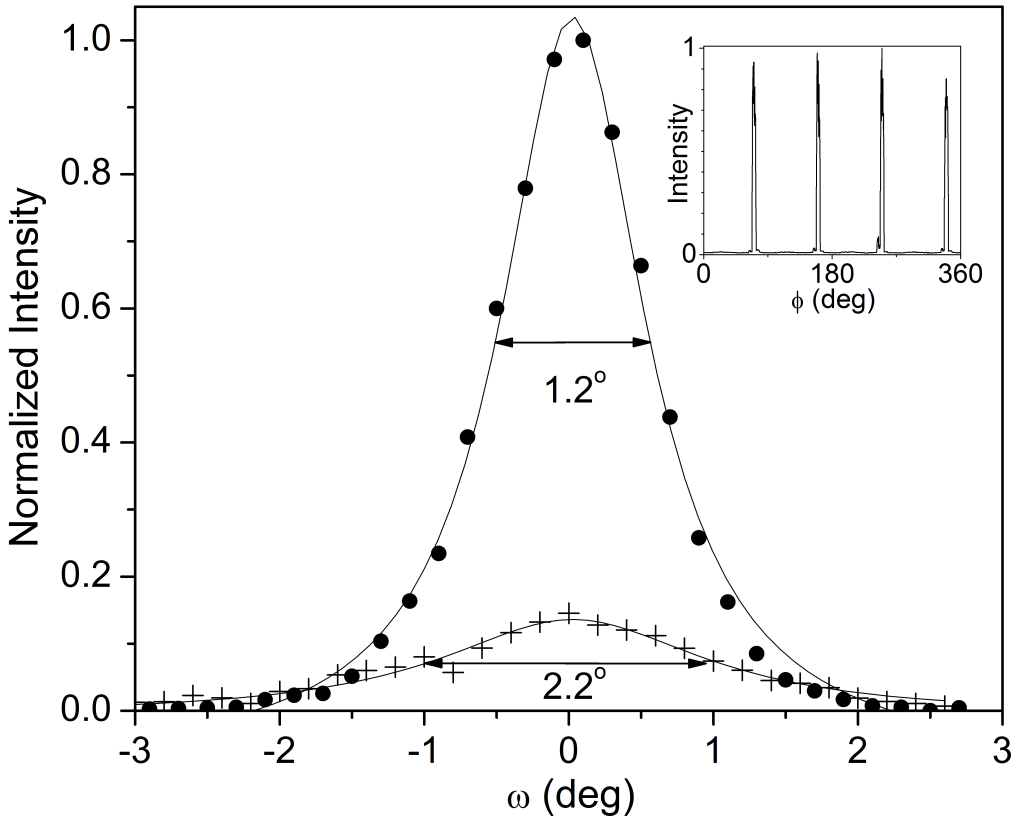

Figure 3.4: Rocking curve for the (100) peak of a $SrTiO_3$sample deposited at 600°C before and after annealing at 1000°C in air. Inset is the (110) pole figure of the same sample after annealing. These data suggest reasonable crystal quality oriented epitaxially.

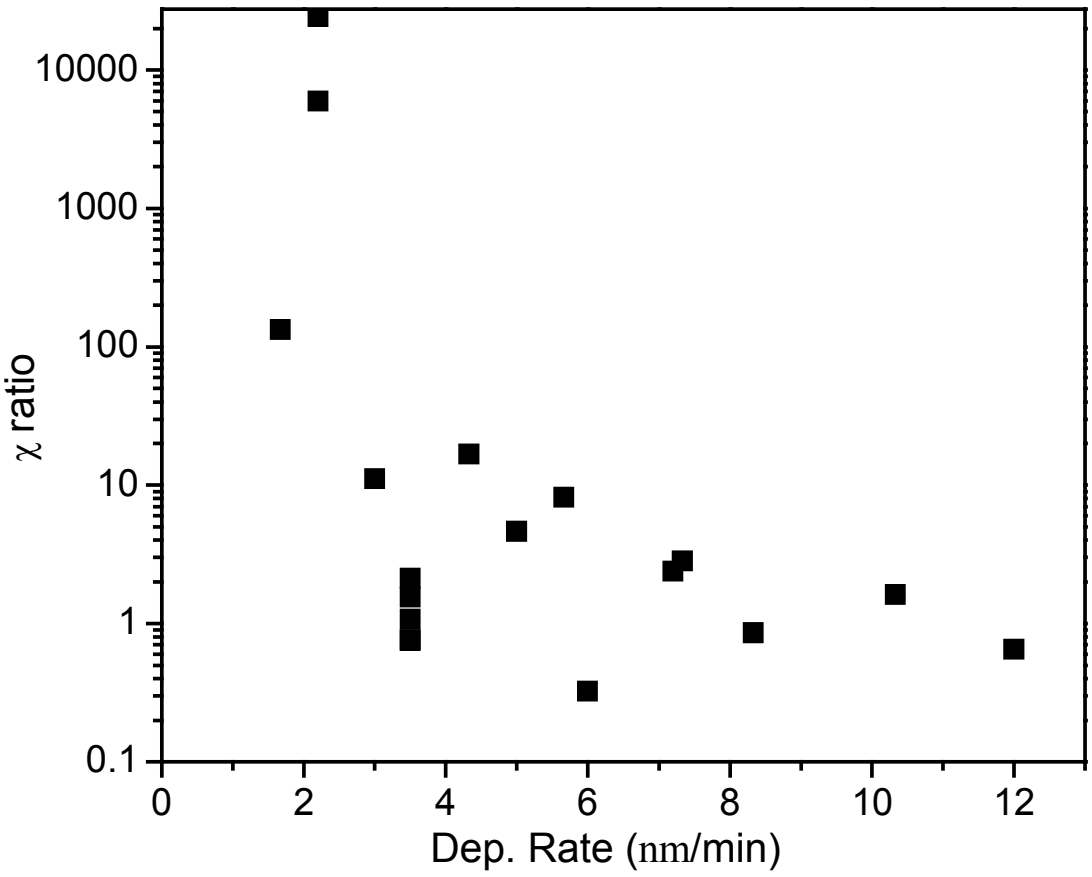

Figure 3.5: The ratio of the intensity of the $SrTiO_3$ (110) plane at the appropriate χ value to the intensity at $\chi = 90°$ as a function of deposition rate for films deposited at 600°C. The crystal quality drops precipitously with deposition rates above 2nm/min.

order to grow the epitaxial heterostructure, compromises on sputtering conditions must be made. As indicated above, the deposition parameters for $SrTiO_3$ allow a relatively narrow window for optimal crystal quality. In particular, a high deposition temperature and moderate oxygen content (40% by volume) were optimal for growing $SrTiO_3$ on MgO. Fortunately, these process parameters result in excellent NiO crystal quality as well. While a higher deposition rate for NiO could be achieved by lowering the oxygen content during NiO deposition, it is desirable to keep process parameters constant during the entire deposition of the heterostructure. We therefore adopted the following deposition parameters: Tsubstrate = 600°C, P_{O2}=12mtorr, and P_{Ar} = 18 mtorr. The NiO was deposited at 100 W using an elemental Ni target and $SrTiO_3$ at 50W from a ceramic $SrTiO_3$ target. The two sputtering sources were arranged at 180° from each other with the sample in the middle.

The growth of epitaxial $SrTiO_3$/NiO/MgO was fount to be straightforward; the excellent crystal quality of the NiO layer leads to epitaxy comparable to $SrTiO_3$/MgO. The FWHM of the $SrTiO_3$ (100) diffraction peak was 0.9° after annealing at 1000 °C for 1 hour, which is better than for $SrTiO_3$/MgO. We attribute the improved crystal quality to the slightly improved lattice mismatch between $SrTiO_3$ and NiO compared to $SrTiO_3$ and MgO.

The analysis of the opposite stack proved to be less straightforward. The NiO/$SrTiO_3$/MgO heterostructure results in the same difficulty with respect to XRD characterization; the top film diffraction peaks are obscured by the substrate. Nevertheless, XRD analysis of this sample showed that there was a small amount of misoriented NiO material; the ratio of oriented to misoriented material was not possible to estimate quantitatively. Because so little misoriented material is observed, we infer that the NiO has relatively good crystal quality. This was confirmed by the subsequent growth of high quality epitaxial $SrTiO_3$ on top of this layer.

A $(SrTiO_3/NiO)_n/MgO$ film with n=2 was then grown with each individual $SrTiO_3$ or NiO layer being about 100 nm thick. This structure has two layers of $SrTiO_3$ grown on NiO, and of course the $SrTiO_3$ has XRD peaks not obscured by the substrate. The crystal quality of the $SrTiO_3$ is representative of the crystal quality of the entire stack. XRD analysis of this heterostructure again showed a small amount of misoriented NiO; however, there was no evidence of misoriented $SrTiO_3$. Figure 3.6 shows the $SrTiO_3$ (100) rocking curve for this sample with the (110) pole figure inset. The FWHM of 1.3° suggests that there has been very little degradation in the top $SrTiO_3$ film due to possible inferior crystal quality of bottom layers. The pole figure shows a good fourfold symmetry with no evidence of misoriented phase. These data confirm that NiO can be grown on $SrTiO_3$.

We have determined the growth parameters necessary for synthesisi of epitaxial heterostructures of $(SrTiO_3/NiO)_n/MgO$ using reactive r.f. off-axis sputtering. Systematic exploration of the process parameters appropriate for each individual layer allowed us to identify common conditions that yield material with excellent crystal quality. These multilayers are the basis for a unique multiferroic material that could exhibit a negative index of refraction int eh the terahertz region. In order to achieve this, it will be necessary to adjust the resonances associated with each layer using doping. The off-axis sputtering approach used in this study is particularly suitable for quickly examining doping effects of thin films.

3.2 Bulk NiO and $SrTiO_3$ ceramics

A second method of generating a material with a negative index of refraction is through bulk ceramics. A small grain composite material of NiO and $SrTiO_3$ should exhibit a negative index of refraction if the resonances are made to match and the particle size is much smaller than the wavelength of radiation of interest. In order to make a composite material consisting of NiO and $SrTiO_3$, the materials must be

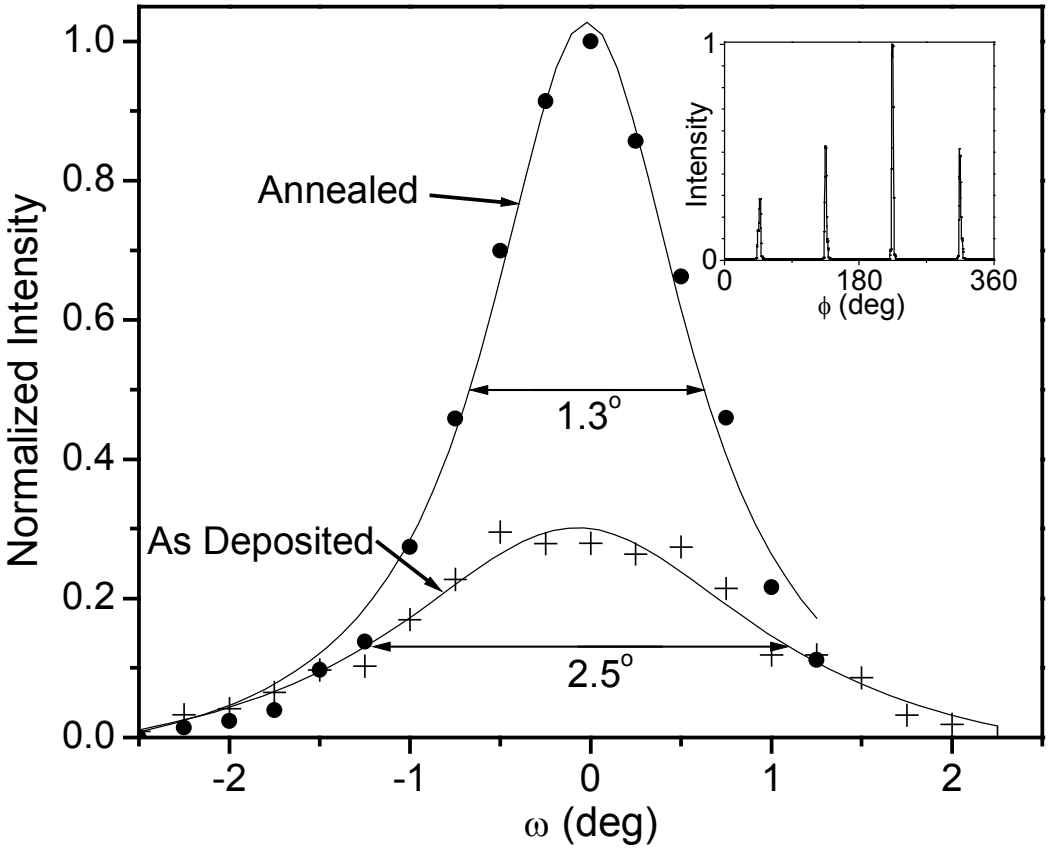

Figure 3.6: Rocking curve for the (100) peak of a $(SrTiO_3/NiO)/_n/MgO$ sample deposited at 600°C before and after annealing at 1000°C in air. Inset is the (110) pole figure of the same sample after annealing. Very little degradation in the crystal quality of the top layer is seen.

compatible and non-reacting. In order to test this, ceramics of NiO, $SrTiO_3$ and a 50/50 at % composite of NiO/$SrTiO_3$ were fabricated from NiO and $SrTiO_3$ powders. The powders were mixed in a mortar and pestle and pressed into 0.5 in. (1.27cm) diameter pellets of approximately 1-2 mm thick. Samples were pressed at a pressure of 100 MPa using isopropyl alcohol as a lubricant. The sample were sintered in air at temperatures of up to 1550°C. The theoretical density of $SrTiO_3$ was achieved with a 1400°C sinter; however, the highest density for NiO was only about 80% of the theoretical. This kept the density of the composite material at about 85% of the theoretical. The density is likely to improve with hot pressing.

Figure 3.7 shows the XRD results for the composite material compared with single phase $SrTiO_3$ and NiO after sintering at 1550°C. The composite shows evidence of only two phases, $SrTiO_3$ perovskite and NiO rocksalt structures, with lattice constants unchanged from those of the individual $SrTiO_3$ and NiO samples. This is evidence that NiO and $SrTiO_3$ are compatible and non-reacting.

3.3 FTIR measurements of $SrTiO_3$ and NiO in the far-infrared

Fourier transform in the infrared (FTIR) spectroscopy measurements have been completed on samples by Mark Lee at Sandia National Labs. This technique was a reflection technique that converts time domain data into frequency response in the far-infrared. This system did not exhibit a high enough signal-to-noise ratio to measure thin film samples, but resonances measured for bulk ceramics.

Figure 3.8 shows the FTIR results for the pressed powder composite sample sintered at 1400°C. The sharp kink in the reflectivity at about 175 cm^{-1} is thought to be due to a twisting of the Ti-O bonds [122-123]. It is undetermined whether or not that peak can be systematically shifted to lower frequency – if so, it might prove useful for achieving a negative index in this system. The peak of interest in this discussion is the

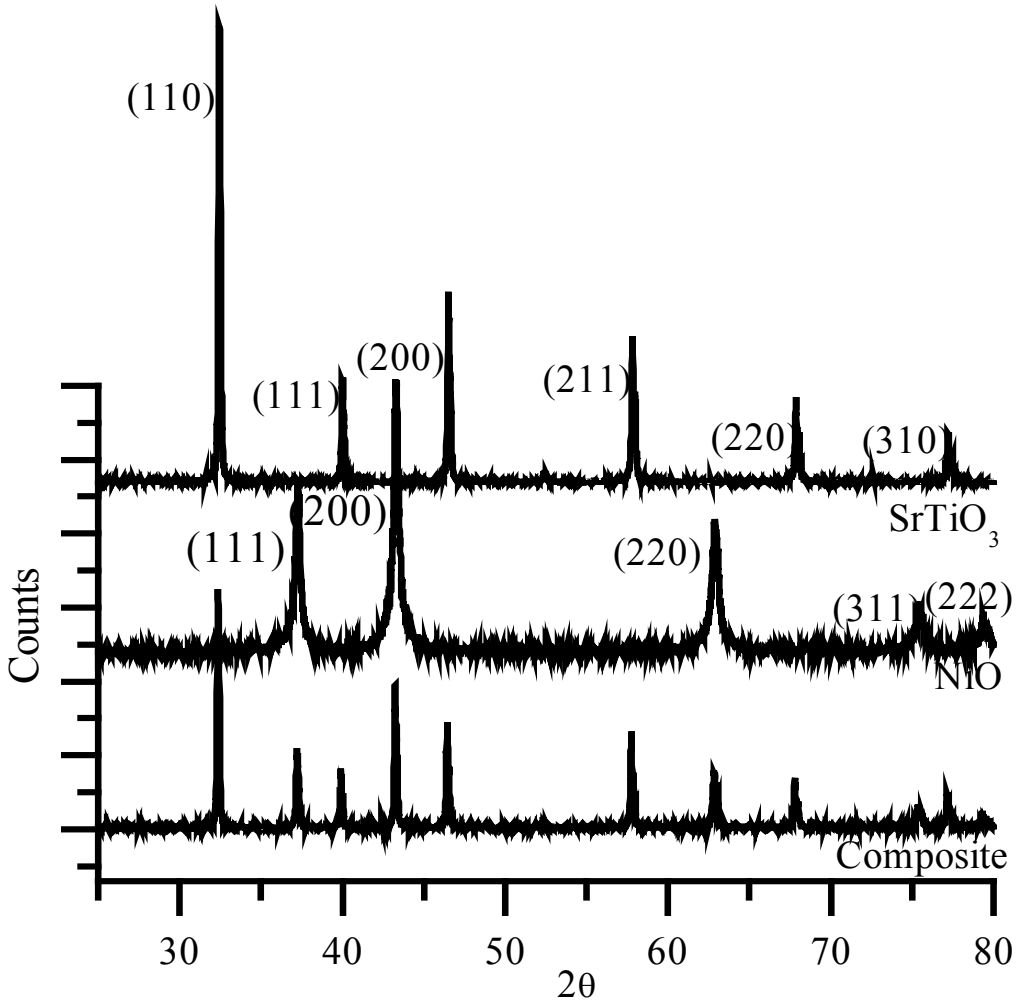

Figure 3.7: XRD results for pressed powder $SrTiO_3$/NiO composite. Composite was 50 atomic % and was sintered at 1550°C. Composite is made up of only perovskite $SrTiO_3$ and rocksalt NiO phases.

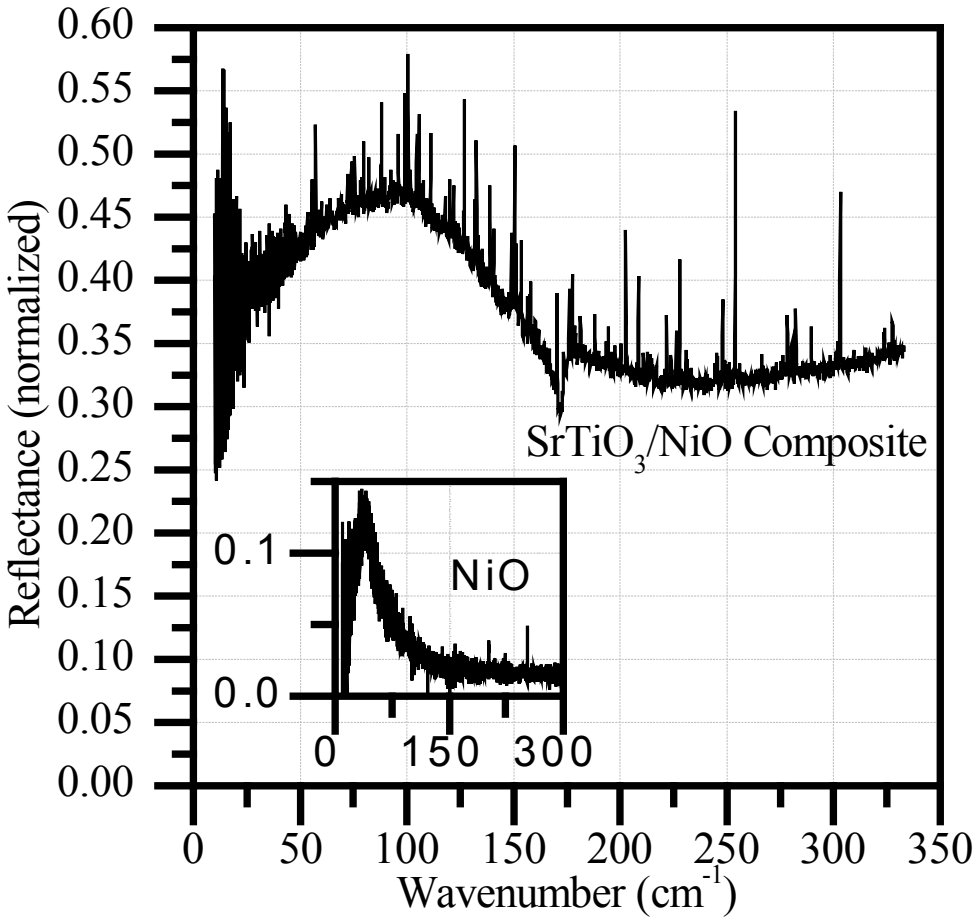

Figure 3.8: FTIR results for $SrTiO_3$/NiO ceramic. The $SrTiO_3$ dipolar resonance can be seen around 100 cm^{-1}. The NiO AFMR signal (inset) is smaller at around 35 cm^{-1} and is difficult to resolve in the composite material.

broad peak visible at about 100 cm^{-1}, which has been shown to shift with temperature and doping (Chapter 1). The other small peaks throughout the frequency range are due to residual water vapor in the measurement chamber. The NiO AFMR cannot be identified in the composite sample due to the low signal-to-noise ratio at low wavenumbers. The inset shows the FTIR reflectivity of the pure NiO sample for comparison, with a resonance peak visible at about 36 cm^{-1} as expected. The weak signal has been attributed to the poor density and rough surface achieved in the pressed ceramic. Improvement of the NiO density and surface of the sample should significantly improve this signal. These data show that the polycrystalline samples exhibit strong resonance.

In theory, this bulk ceramic could be used to achieve a negative index of refraction – however, improvement of the NiO density is required to improve the material response. It would also be beneficial to gain the signal-to-noise ratio needed to measure the response of a thin film heterostructure. This might be possible through use of polarized radiation [124] or through high-intensity sources such as synchrotrons. Thicker heterostructures might also aid in the signal to noise ratio. It is uncertain how thick the heterostructures or how many layers can be grown before crystal quality degrades to an unusable manner.

3.4 Terahertz Time Domain Spectroscopy

Terahertz time domain spectroscopy (TDS) has been attempted on the various materials designed for a negative index of refraction in the far infrared. THz TDS measures the electric field of an electromagnetic pulse with resolution in the picoseconds. Taking the Fourier transform of the measured signal in the time domain results in a power signal as a function of frequency. By sending a well-known signal

pulse that contains a range of frequencies through a sample, one can learn information about the material response by looking at the transmitted pulse.

THz TDS has been used successfully to measure the NiO AFMR. Figure 3.9 shows the electric field of the pulse signal in the time domain. It can be seen that the pulse signal has a time scale of about a picosecond – i.e. about a 1 THz frequency. Figure 3.10 shows the complex transmission signals (real and imaginary) of the NiO sample. A peak in the imaginary part of the transmission is obvious at the expected value of the AFMR at 1 THz. The AFMR can be seen more clearly in Figure 3.11 by looking at the transmission power spectrum for NiO. The transmisson clearly drops by an order of magnitude at 1 THz. This is a clear measurement of the NiO AFMR.

THz TDS measurements were attempted on thin film and bulk ceramic SrTiO3 as well. In general, the thin films were too thin to be able to have a strong enough effect to measure. For thin samples, secondary reflection signals will follow the primary signal in a shorter time. This results in a short time scale for which the Fourier transform can be done. A shorter time scale means less accuracy in the frequency domain. For $SrTiO_3$, the bulk ceramic had a very low transmission of the signal. No clean signals of the $SrTiO_3$ resonance have been completed using THz TDS.

In order to measure a material response using THz TDS, several aspects must be met. First, the sample must be thick enough in order to have a long time scale between the initial transmission pulse and any subsequent pulses due to reflections. The usable collection time is the time starting with the initial transmission pulse until the first pulse that results from reflections in the sample. Second, there must be a strong enough transmission through the material in order to measure an accurate electric field. For most materials, this results in a need to find the ideal thickness in order to balance transmitted electric field strength with usable collection time. For

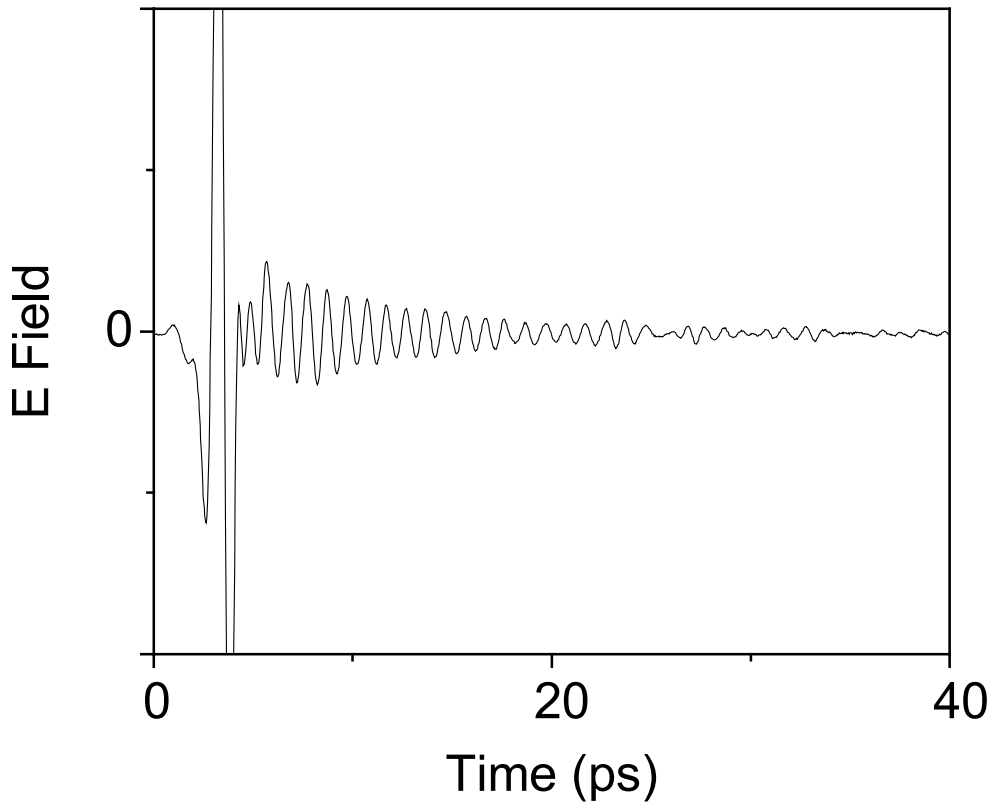

Figure 3.9: Time domain electric field transmission through a NiO ceramic sample with a thickness of 4.95mm.

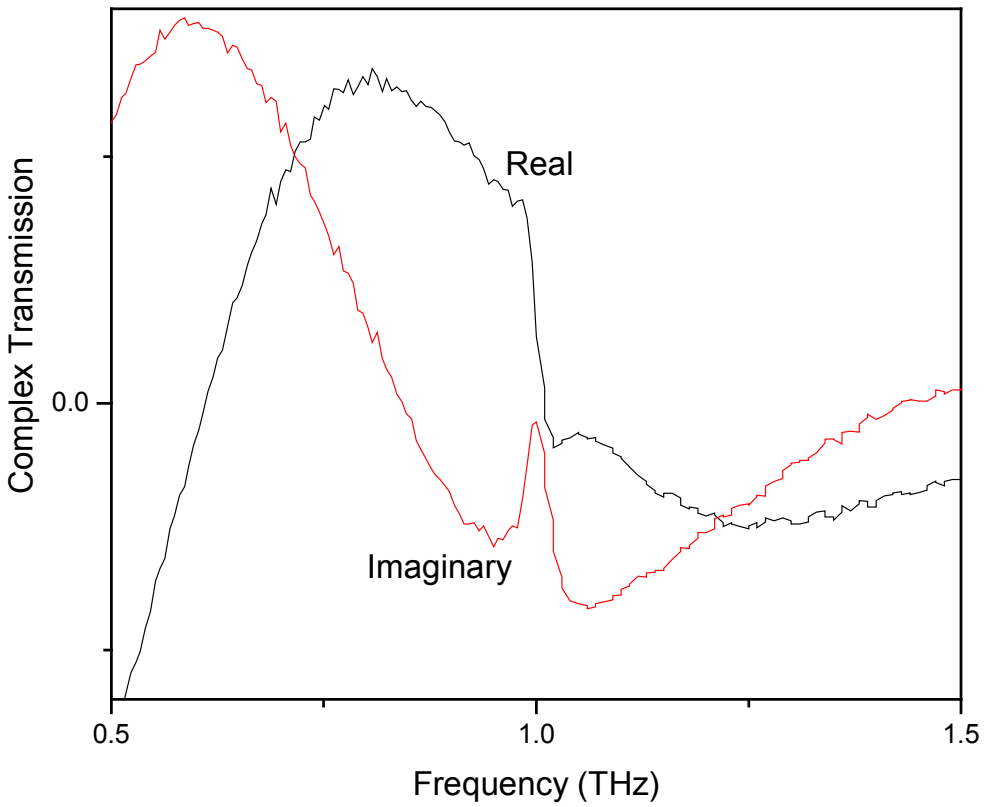

Figure 3.10: The complex Fourier transform of the transmitted electric field normalized to air. A sharp resonance at 1 THz is obvious in the imaginary part of the transmission.

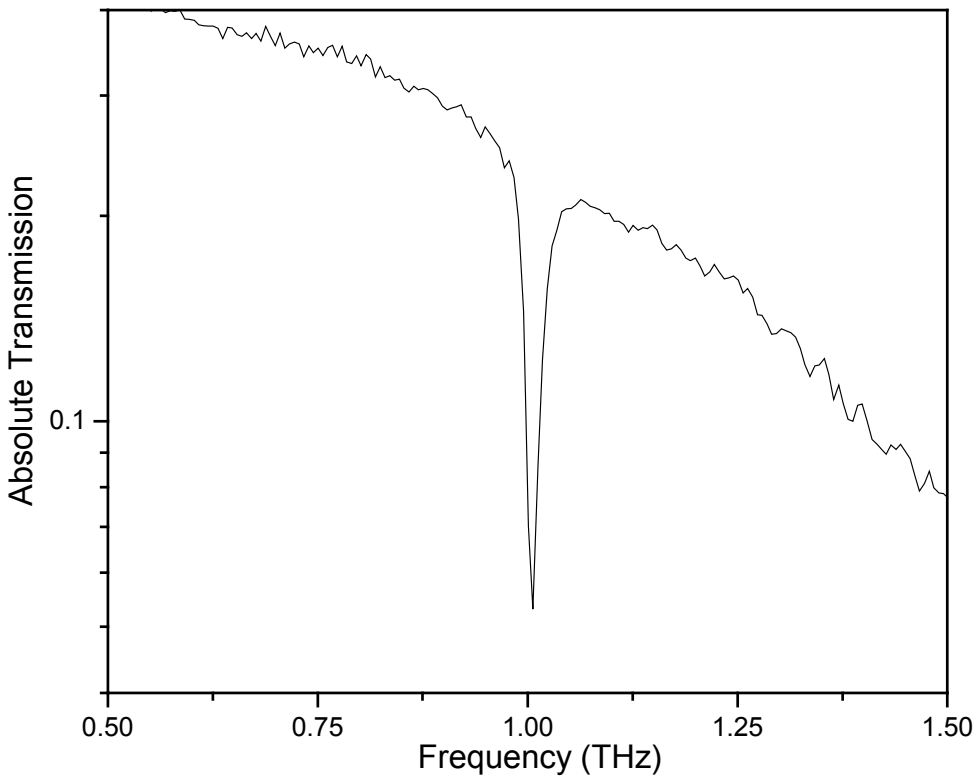

Figure 3.11: The absolute value of the normalized Fourier transform of the transmitted electric field. A large drop in the absolute transmission can easily be seen at 1 THz.

highly transparent materials, such as NiO, this does not create a problem. For less transparent materials such as $SrTiO_3$, this becomes more difficult or even impossible.

3.5 Conclusions and the Future

A material that has both a negative permittivity and a negative permeability at the same frequency will have a negative index of refraction. We have proposed a method of obtaining a negative index of refraction in the far-infrared using only intrinisic material properties. This involves combining the negative permeability from the NiO AFMR with the negative permittivity from the $SrTiO_3$ ionic resonance. We expect to be able to shift these resonances to match through doping, changing temperature or through applying a magnetic field.

Thus far, two methods of fabricating the composite have been devised. The first involves an epitaxially grown thin film heterostructure, the second involves small phase bulk composite ceramic. Two methods of measuring the terahertz frequency response have been attempted. The first is an FTIR technique working in reflection. This method has successfully measured the strong reflection signal of $SrTiO_3$ and indicated both the soft ionic phonon mode related to ferroelectricity in perovskite materials and other high frequency modes. The FTIR technique has also seen a signal from the NiO AFMR, however this signal was very weak and could not be seen in the composite material due to the strong $SrTiO_3$ response and the high level of noise. The second technique was THz TDS. This technique has been able to measure the NiO AFMR with high precision. The $SrTiO_3$ dielectric resonance has not been measured to date. This is due to the poor transmission of $SrTiO_3$ at these frequencies.

In order to achieve and verify a negative index of refraction in the far-infrared, several items need to be resolved. First, a method of measuring both the dielectric and the magnetic resonance with high precision must be devised. Currently, a reflection technique has resulted in a strong signal for the ionic resonance of $SrTiO_3$, but has a

week signal for NiO. The transmission THz TDS technique has allowed for a strong signal response for the NiO AFMR, but has been unable to measure the $SrTiO_3$ ionic resonance. An improved measurement technique or a different material combination is needed in order to achieve this.

CHAPTER 4

IMPROVED CONDUCTIVITY OF ZINC OXIDE THROUGH CODOPING WITH INDIUM AND ALUMINUM

4.1 Introduction

Transparent conducting oxide (TCO) materials are very important for a variety of current and future applications, including flat panel displays, photovoltaics and transparent electronics [30,37]. Currently, indium tin oxide (ITO) is the most commonly used TCO. ZnO has been studied extensively in recent years [59,61], leading to development of ZnO materials that might be able to replace the more expensive ITO films. Highly conductive n-type ZnO has been achieved through doping with Al [83-104], In [110-115] or Ga[105-109]. However, the electrical properties of ZnO are highly dependent on native point defects such as oxygen vacancies, zinc intersitials [62-65] and even hydrogen [70-77] which all act as electron donors. In order to obtain high conductivity ZnO, these point defects must be deliberately induced. In general, the highest conductivity is achieved after annealing in reducing conditions (vacuum, inert gases or hydrogen) while annealing in oxidizing conditions (typically O_2 or air) degrades the conductivity significantly [53,125-128]. Reducing anneals are one way to activate dopants and increase the carrier concentration.

However, it is desirable to achieve high conductivity ZnO without the need for high temperature processing or relying on oxygen vacancies or hydrogen as dopants as these approaches result in materials with poor electrical stability in air. We propose that one method to achieve this might be through codoping with two donors. Zn2+ has an ionic radius of 0.074nm while Al^{3+} has an ionic radius of 0.05 nm and In^{3+} has 0.081nm [119]. These large mismatches of -32% for Al^{3+} and +9% for In^{3+} can lead to

large strain in the lattice. We anticipated that codoping with both Al^{3+} and In^{3+} should allow for higher total dopant solubility and activation along with improved crystal quality even for low temperature depositions without the need for high temperature annealing. This could enable applications with a low thermal budget, such as TCO films deposited on polymer substrates or films. We used a composition spread technique to systematically study the effect of codoping ZnO with Al and In. Materials with a wide range of compositions were deposited in a single experiment, i.e., under identical conditions, which facilitates a robust comparison of composition-dependent properties.

4.2 Experimental Details

In order to systematically study the effects of codoping ZnO, we prepared composition spreads using off-axis reactive radio frequency (rf) sputtering as described previously [28]. In this technique, thin films are deposited by cosputtering with two or more independent magnetron sputtering guns located 90° to each other and 90° to the substrate. This results in a composition spread that has a variation of composition on a single 2 to 3 inch diameter substrate. Using this technique, we deposited three ZnO films on Corning D-263 glass. One film was Al-doped only, one In-doped only and the third was doped with both Al and In. The combinatorial technique allowed for a doping range of 1-7 atomic percent for each cation dopant. The films were deposited using 2-inch diameter metal Zn, Al and In targets in 2.4 mtorr O_2 and 27.6 mtorr Ar. The Zn, Al, and In targets were powered by independent rf supplies (200W-Zn, 100W-Al, 20W-In) to achieve the desired composition range on the substrates. The films thickness ranged from 200 to 500 nm on each substrate. No systematic effect of thickness was observed. The films were deposited with a substrate temperature of 250°C in a system with a base pressure of 2×10^{-6} torr. It should be noted that the process parameters were chosen such that an undoped ZnO film is

insulating. Compositions were verified through energy dispersive x-ray spectroscopy (EDS). Electrical properties were measured using Hall measurements in the van der Pauw configuration. In order to decrease the effect of composition and thickness variation on a sample hall measurements samples were cut in to 5 mm squares. Measurements on unpatterned squares were compared with those obtained on samples scribed with a smaller clover leaf pattern. The two measurements were consistent within about 10% which confirms that the small inhomogeneity in a single sample had little impact on the electrical measurements. X-ray diffraction (XRD) data was taken using a Bruker AXS system with a General Area Detector Diffraction System (GADDS). This system allows for quickly viewing several diffraction peaks even for highly textured films. All films – all compositions – were found to be >80% transparent between wavelengths of 400 – 1000 nm using a calibrated spectrophotometer. This is excellent for such thick films (>200 nm).

4.3 Results and Discussion

The measured electrical properties are summarized in Figure 4.1 as a function of composition. Data for the pseudobinary $Zn_{1-x}Al_xO_y$ sample are presented on the ZnO-$AlO_{1.5}$ tie line and data for the $Zn_{1-x}In_xO_y$ sample are presented on the ZnO-$InO_{1.5}$ tie line. These data are also included as a xy scatter plot in Figure 4.2 for clarity. The contours represent our interpretation of the underlying trends and are consistent with the raw data. In Figure 4.1a, it can be seen that there is a maximum in the conductivity around 1.5% Al for the sample with only Al doping. Above this level, the conductivity drops due to a decrease in the mobility while the carrier concentration is approximately constant as seen in Figure 4.1b and 4.1c. That is, Al incorporation above ~1.5% is electrically inactive as a dopant. For the In doped sample, the conductivity continues to increase slowly with indium content for the entire range.

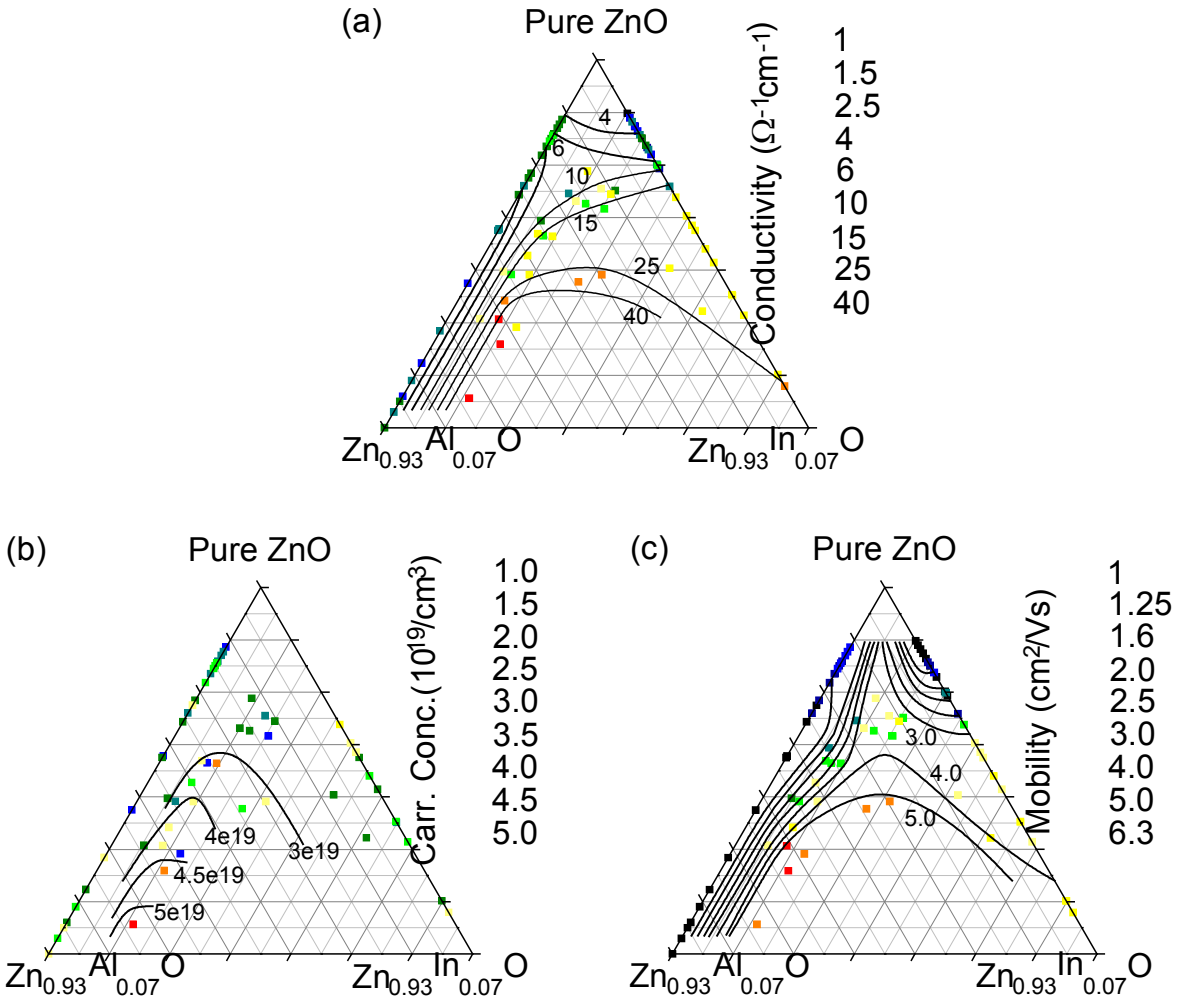

Figure 4.1: The electrical properties of ZnO composition spreads. Data obtained from the $Zn_{1-x}Al_xO_y$ and the $Zn_{1-x}In_xO_y$ samples are plotted on the ZnO-$AlO_{1.5}$ and ZnO-$InO_{1.5}$ tie lines. The conductivity ($\Omega^{-1}cm^{-1}$) ,carrier concentration (cm^{-3}) and mobility (cm^2/Vs) are plotted in the conventional ternary composition diagrams (a), (b), and (c), respectively. Isopleth contours have been added to show the authors' interpretation of the trends.

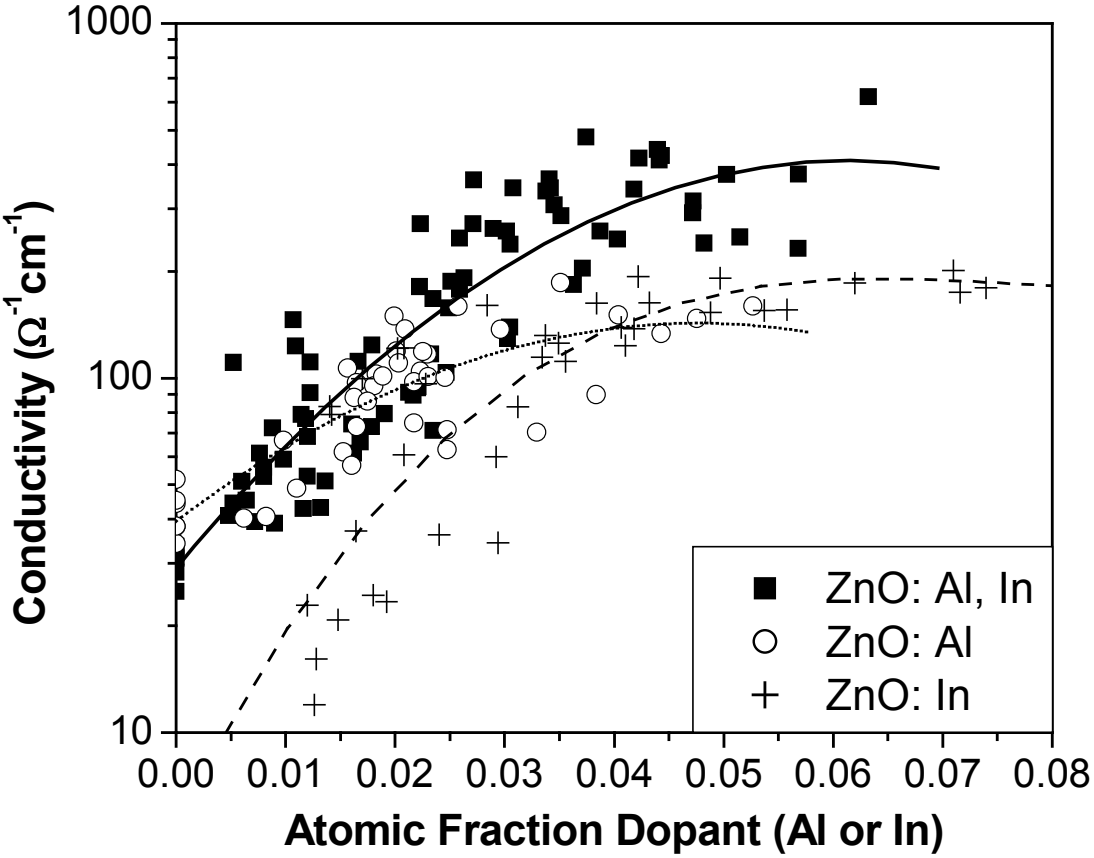

Figure 4.2: Conductivity of ZnO doped with Al, In and codoped with both Al and In as a function of dopant concentration. The conductivities appear to plateau by 1.5% for Al doped and 4% for the In doped or codoped. The codoped samples have higher conductivities than either Al or In doping alone.

Although there are some reports of Al solubility as high as 4% [96], these trends agree well with the literature [83-104].

The codoped sample shows improvement in the conductivity compared to either singly-doped film. In particular, near the ZnO-$AlO_{1.5}$ tie line, the conductivity increases by a factor of 4 or more with small In additions. For example, for $Zn_{1-x}Al_xO_y$ with $x > 0.025$, the conductivity has dropped below 4 $\Omega^{-1}cm^{-1}$. When 1% In is added the conductivity increases to more than 15 $\Omega^{-1}cm^{-1}$ for $Zn_{0.96}Al_{0.03}In_{0.01}O_y$ and to more than 40 $\Omega^{-1}cm^{-1}$ for $Zn_{0.95}Al_{0.04}In_{0.01}O_y$ – an order of magnitude increase. From Figure 1b and 1c, it can be seen that there is an increase in both mobility and carrier concentration with codoping in this range.

The optical transmission of several compositions is shown in Figure 4.3. The transmission is above 80% from 400 nm – 1000 nm. One can also see the well known Burstein-Moss shift of the band gap that results for high carrier concentrations. This shift is further shown in the inset of α^2 versus energy. This shift agrees well with the electrical data presented.

Figure 4.4 shows the XRD scattering intensity versus scattering angle (2θ) for a typical film. As is typical for ZnO, this and all of our films were highly c-axis textured. The inset shows the GADDS output for the same sample. The area detector allows us to sample a wide range of reciprocal space in a single experiment. In order to determine whether size compensation plays an important role in the structure of ZnO and therefore can be implicated in the electrical properties, the atomic volume was examined. Several diffraction peaks were located using the GADDS data and precise lattice parameters were calculated using the Cohen technique [120]. Figure 4.5 shows the change of the volume of the unit cell as a function of composition. Again, the xy scatter plot is included in Figure 4.6 for clarity. It can be seen that the volume shifts systematically from smaller volume for Al doping to larger values for In doping.

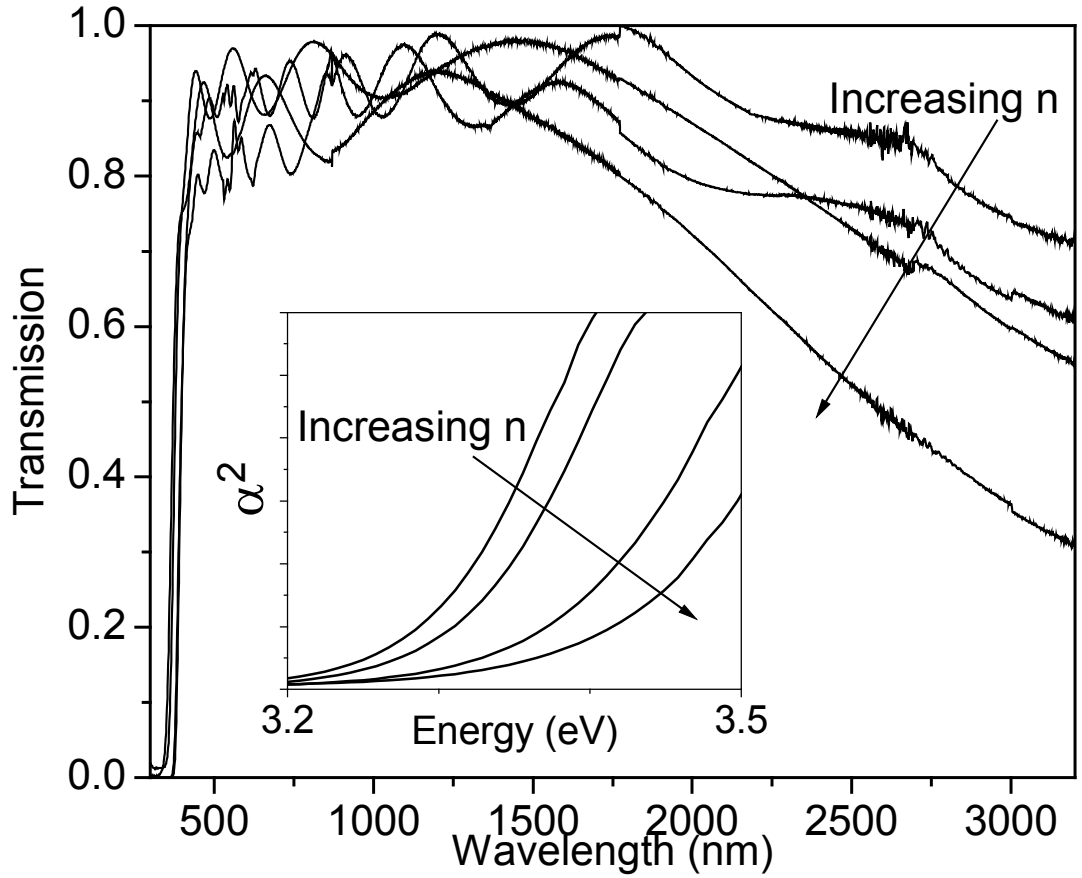

Figure 4.3: Optical and near-infrared transmission of representative samples with various Al and In doping levels. The transmission is greater than 80% over the range 350 nm to more than 1000 nm. The arrows show increasing carrier concentration. The shift in the plasma edge agrees with the Hall measurements. The Burstein-Moss shift can be seen in the plot of α^2 (inset) vs. photon energy.

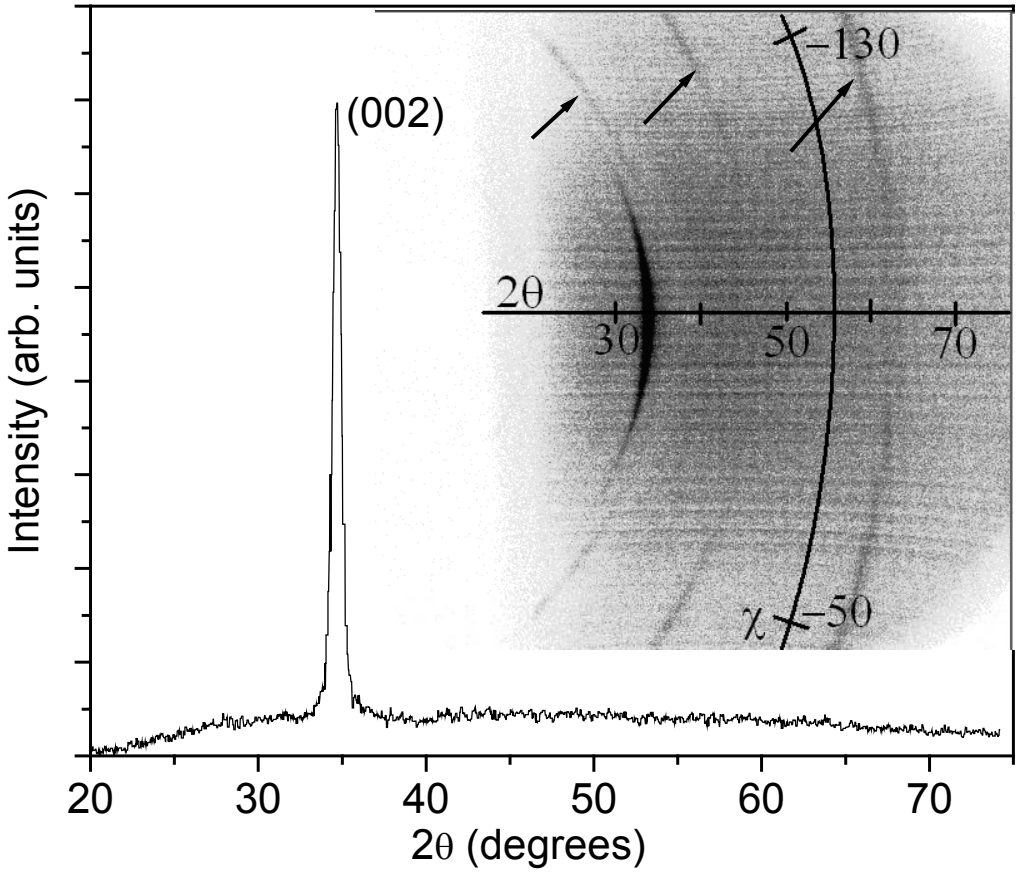

Figure 4.4: XRD results for a representative sample. The high level of texture can be seen in the standard theta-theta plot. The inset shows the output from the two-dimensional detector, which allows for quick characterization of diffraction peaks (arrows) away from the equatorial plane in a textured film. The scale for the scattering angle χ is indicated for the case $2\theta=56^{\circ}$.

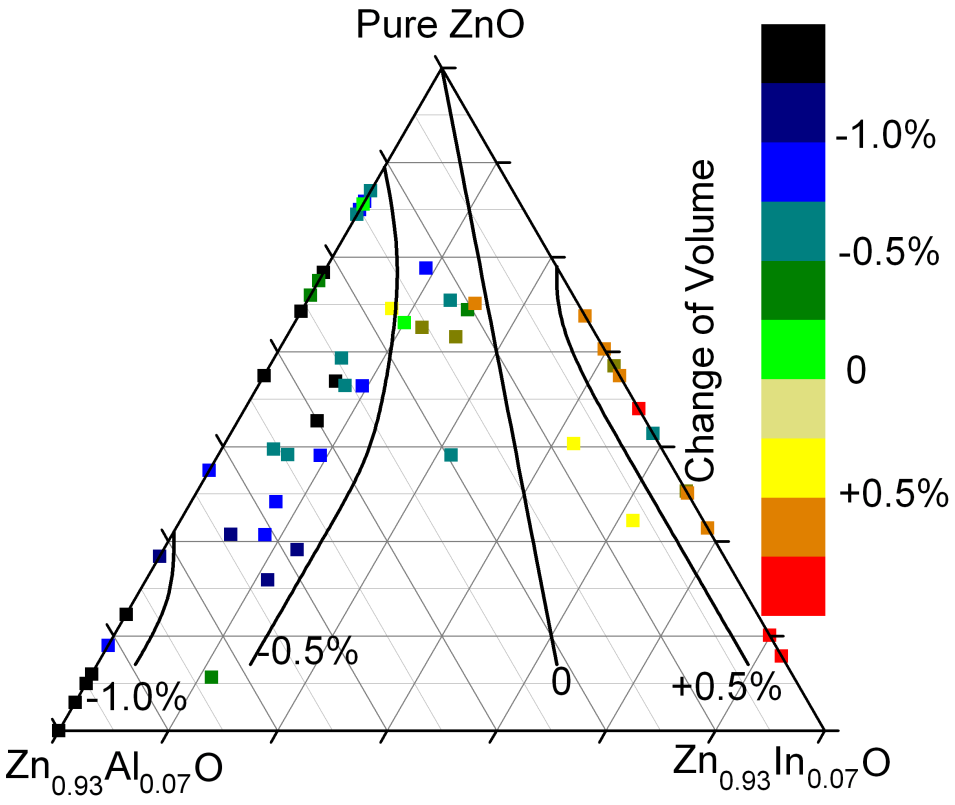

Figure 4.5: The change in the atomic volume as a function of composition. Data obtained on the $Zn_{1-x}Al_xO_y$ and the $Zn_{1-x}In_xO_y$ samples are plotted on the ZnO-$AlO_{1.5}$ and ZnO-$InO_{1.5}$ tie lines. The "0" contour represents calculated compositions that should yield no change from the atomic volume of undoped ZnO.

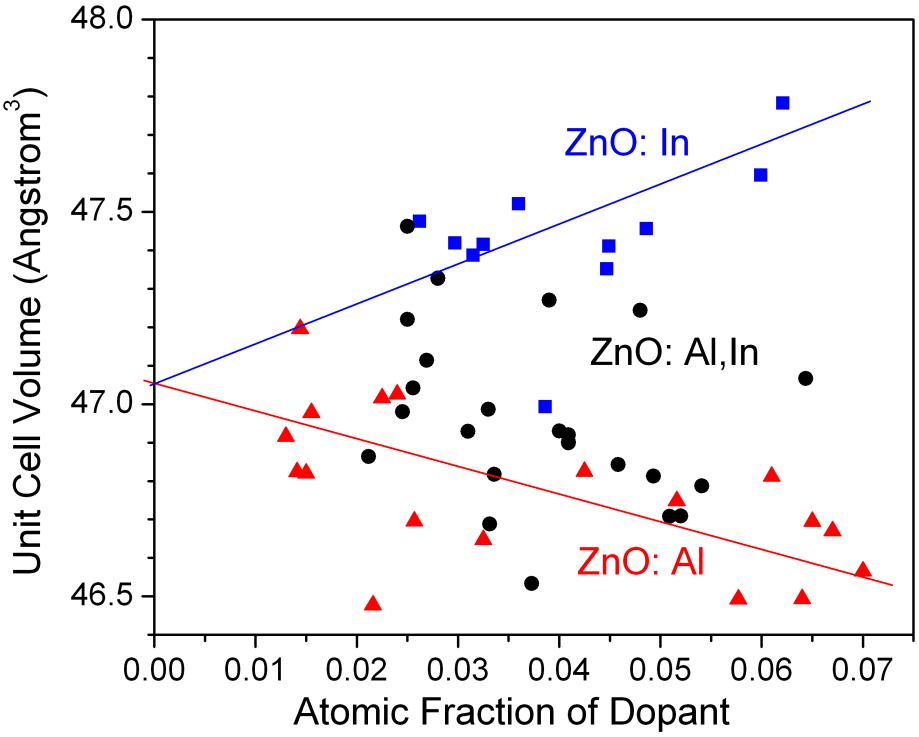

Figure 4.6: The volume of the unit cell of ZnO doped with Al, In and codoped with both Al and In as a function of dopant concentration. Doping with In increases the unit cell volume linearly while doping with Al decreases the unit cell volume linearly.

As expected from their relative ionic radii compared to Zn, Al has a much greater effect than In. It is also expected that there should be a line at which one would expect the cell volume to remain the same as pure ZnO due to dopant size compensation. In the simplest model, $\Delta V = (r_{Zn} - r_{Al})X_{Al} + (r_{Zn} - r_{In})X_{In}$ where r_{In} and r_{Al} are the ionic radii stated above. The locus of concentrations for which $\Delta V = 0$ forms a line as indicated on the ternary plot. Codoping clearly has a strong effect on the local structure in the lattice.

It has been shown that there is a structural and electrical effect on ZnO from codoping. In comparing Figure 4.1 with Figure 4.5, it can be seen that the conductivity of Al doped ZnO reaches a maximum at about 1.5% Al for our films. This results in about 0.5 – 0.6% compression in the lattice volume. Above this level, the carrier concentration no longer increases much and the mobility decreases, which is consistent with a model in which Al no longer occupied substitutional sites but instead precipitates out in nanocrystals of Al_2O_3. By also adding the larger In^{3+}, more Al^{3+} can be incorporated without exceeding the critical 0.5 – 0.6% strain level. It can be seen that the carrier concentration increases along the isochoric line of about 0.5-0.6% strain. The mobility is improved by keeping the lattice volume closer to that of pure ZnO – we interpret this as reflecting the absence of scattering by long range strain-induced inhomogeneity.

4.4 Conclusions

We have demonstrated a dramatic improvement in the electrical properties of ZnO with codoping. It should be noted that the conductivity in the subject films are lower than the highest reported in the literature, but we point out that our films are intentionally deposited under conditions that are not optimal for high conductivity: the films were deposited at a modest substrate temperature and with relatively high oxygen content during deposition. The oxygen content was deliberately kept high in

order to minimize the variation in oxygen content across the substrate due to variation in deposition rate. Pure ZnO deposited with these process parameters results in an insulating film. A large increase in conductivity would be obtained, at even lower substrate temperature, by specifically optimizing the deposition parameters (deposition rate, energetic particle bombardment, oxygen fugacity).

This work shows that codoping ZnO with Al and In significantly improves the electrical properties of ZnO with no degradation of the optical properties. In particular, by adding a small amount of In into Al-doped ZnO, we find decreased compression in the lattice volume associated with Al substitution. This allows a higher level of dopant activation as well as improved mobility. With process optimization, codoping could lead to high conductivity ZnO with low deposition temperature and without the need for high temperature annealing or addition of hydrogen. Codoping could lead to an increased viability of ZnO as a replacement of the expensive ITO. The amount of In used in this scenario is an order of magnitude smaller than the amount used in ITO. ZnO-based transparent conductors are prone to degradation during processing in air; the improvements in robustness associated with codoped films are the subject of current investigation.

CHAPTER 5

THERMAL STABILITY OF CODOPED ZINC OXIDE

5.1 Introduction

ZnO has been identified as a possible replacement for ITO for many high-end applications such as flat panel displays. However, there are still significant issues that must be addressed in order for ZnO to actually replace ITO. For FPDs, the transparent electrode must be made very thin in order to keep the device uniform over large-scale areas. This results in a strong need for higher conductivities to improve device performance. Also, the electrical properties of ZnO thin films do not tend to be stable at the high temperatures needed in subsequent processing of these devices. The previous chapter discusses how codoping might improve the conductivity of ZnO. The effect of codoping on the thermal stability will be studied here.

The electrical properties of ZnO have been known to change substantially by annealing in various environments. Annealing in oxygen, nitrogen, hydrogen, air, and other environments have been shown to have large effects on the electrical properties of ZnO. This is due to the high correlation between the electrical properties with point defects, such as zinc and oxygen vacancies and interstitials. It has long been thought that zinc interstials or oxygen vacancies are the leading source of donors in undoped ZnO and still play a large role in the extrinsically doped ZnO as well. Also, compensating defects such as oxygen interstials also affect the electrical properties. It has traditionally been thought that annealing in oxygen or air decreases the n-type oxygen vacancies or zinc interstitials and might introduce compensating oxygen vacancies. Reducing anneals, such as annealing in H_2, have been used to eliminate oxygen interstitials and possibly add oxygen vacancies. More recent experiments have

shown that hydrogen itself acts as a donor in ZnO and is often a significant source of carriers in n-type ZnO.

Using optimized processing, it has been possible to achieve ZnO with conductivities of greater than $10^4\ \Omega^{-1}cm^{-1}$. This processing almost always involve reducing anneals such as in hydrogen. The electrical properties of these materials tend to degrade rapidly when annealed in air or other oxygen or even nitrogen atmospheres. This has been true for ZnO doped with Al, Ga, and In as well. This lack of thermal stability becomes even more problematic for thinner films, which are required for many applications that require a great deal of patterning such as flat panel displays. It is desirable to devise a method to improve on the thermal stability of ZnO. One possible method is through the use of codoping.

5.2 Thermal Stability in Air

The first and easiest anneal study is to heat the samples in air to a moderate temperature. This has been done to the samples presented in Chapter 4. These samples were heated in air at a temperature of 150 ºC for 1 hour. The conductivities of these films have been plotted in Figure 5.1 as a function of composition. It can be seen that best conductivities are located on the ZnO: In tie line. The ZnO: Al sample shows particularly poor conductivity. For the Al doped sample, the best conductivity was obtained in the sample with the least Al concentration (1.5% Al); the conductivity decreases rapidly with increased Al content. This is not surprising, since Al_2O_3 precipitates are thought to form at doping levels above this amount, which will decrease the mobility. A second likely reason for the decrease in conductivity above this amount is that Al collects at the grain boundaries, increasing the grain boundary scattering.

The second annealing study was to anneal the same samples in a modest vacuum of 1×10^{-6} torr at 300 ºC for 1 hour. The electrical data after annealing in

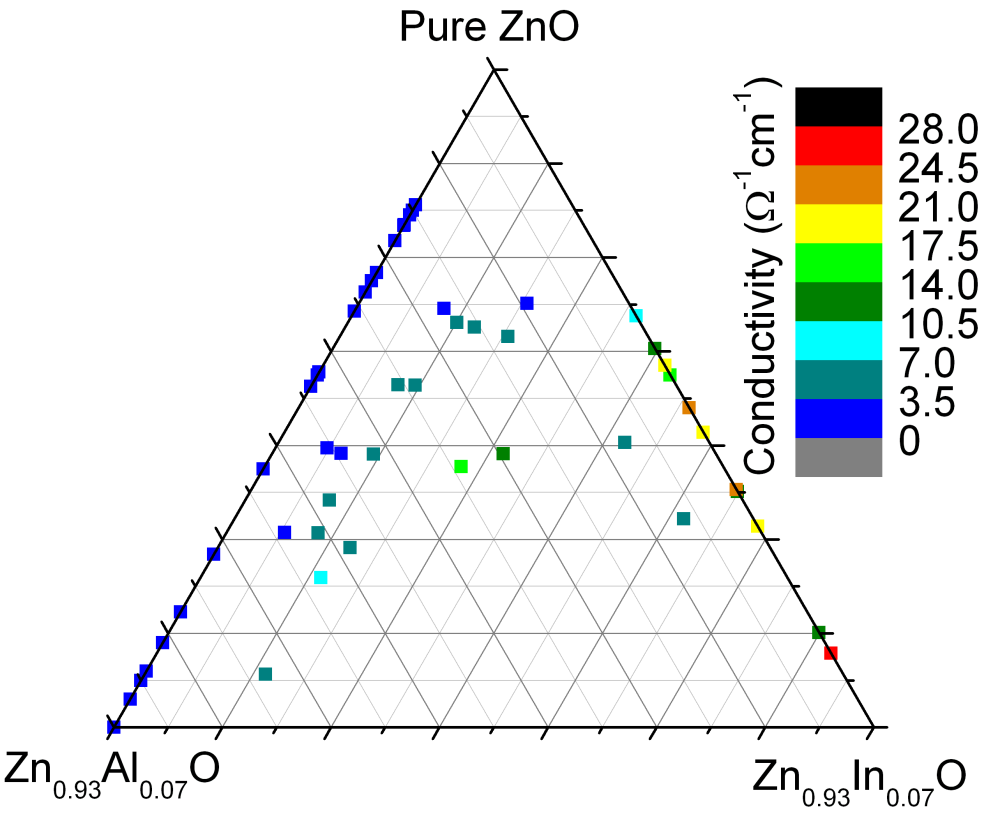

Figure 5.1 Conductivity of (Al,In): ZnO composition spread after annealing in air at 150 °C for 1 hour. The In side appears much more stable than the Al side. A small amount of In greatly increases the conductivity of highly doped Al: ZnO.

vacuum is plotted in Figure 5.2. From Figure 5.2a, it can be seen that the conductivity as a function of composition has a similar trend to the as deposited case in Chapter 4. The best conductivity for the Al doped sample is again at 1.5%. The trend for the In doped sample is less obvious. The codoped sample shows a clear trend that shows high conductivity along the 1% In content isopleth that increases with increased Al content. It is particularly interesting to note that the carrier concentration is higher for areas of high Al content, while the mobility is greatest for high In. The codoped sample shows carrier concentrations that are higher than for the In doped sample along with mobilities that are much higher than for Al doping. In a sense, the codoped sample combines the advantageous behavior associated with each dopant.

In order to further examine this data, cross sections of the data are cut at 3, 4 and 5% total dopant. This corresponds to data for $Zn_{0.97}Al_{y-x}In_x O$, where y = 0.03 for the 3% cross section. The data has been plotted as a function of the In content y. For comparison, the as deposited data has been plotted along with data from both anneals, air and vacuum. Figure 5.3 shows the electrical properties for the 3% cross section. For the dopant amount, there is a steady trend that shows that the conductivity increases with In content. It can be seen that this increase in conductivity is mostly due to an increase in the mobility. It is well known that the mobility of Al doped ZnO decreases rapidly when the Al concentration is above the solubility limit due to precipitates causing increased scattering [84].

Figure 5.4 shows the electrical properties for the 4% cross section again plotted as a function of In content. For this data, it can be seen that there is a decrease in resistivity when adding a small amount of In to the Al doped only sample. This is true for both the as deposited and the air annealed data. There also seems to be a decrease in resistivity until a minimum at around 2% In content, at which time, the resistivity increases slightly for the higher In content. From Figure 5.4 b and c, one can see that

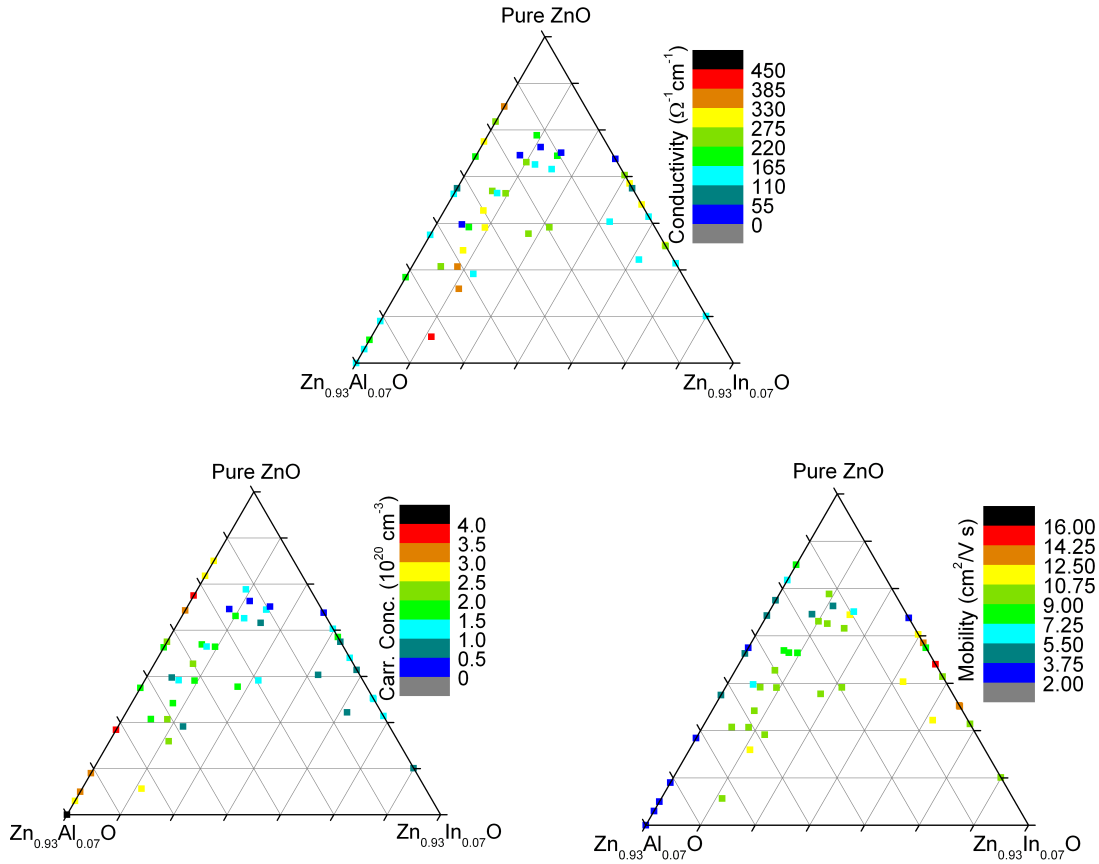

Figure 5.2 Electrical properties of the (Al,In): ZnO composition spread after annealing at 5×10^{-6} torr at 300°C for 1 hour. The (a) conductivity, (b) carrier concentration, and (c) mobility were all obtained from Hall measurements using the van der Pauw technique.

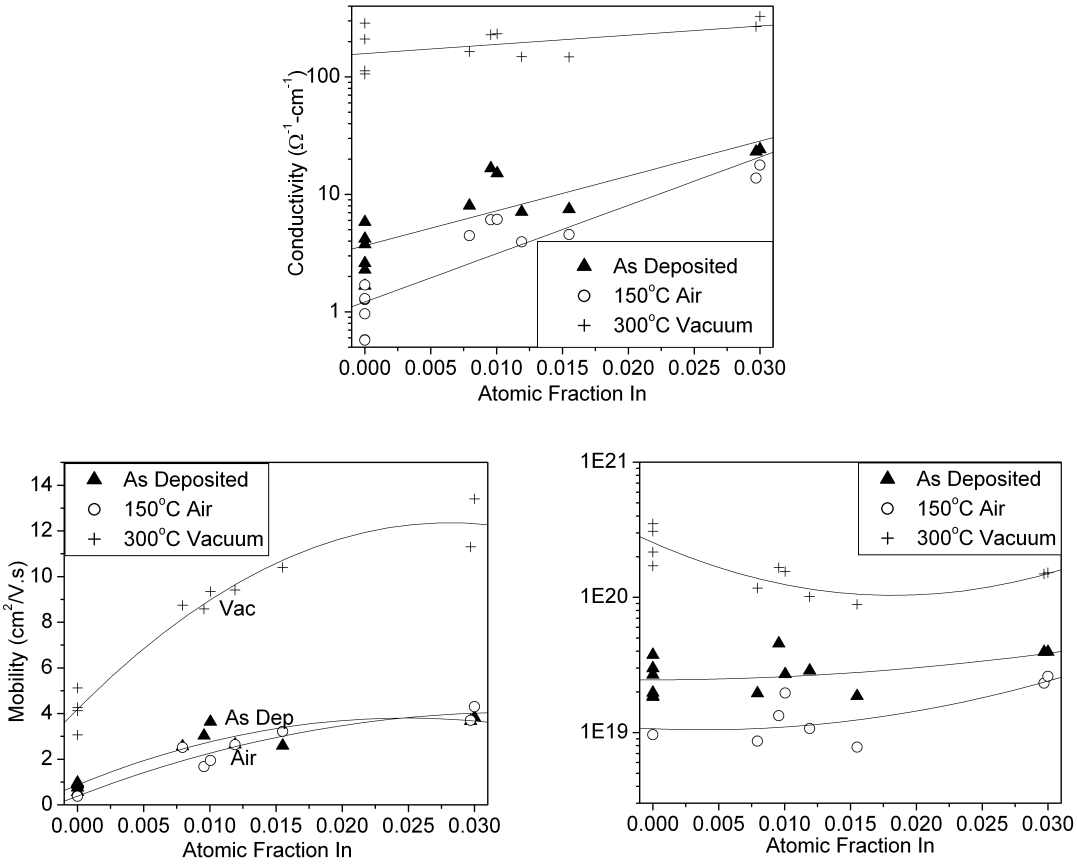

Figure 5.3: The electrical properties as deposited, after annealing in air and after annealing in vacuum for samples with total dopant ($X_{Al} + X_{In}$) equal to 3%.

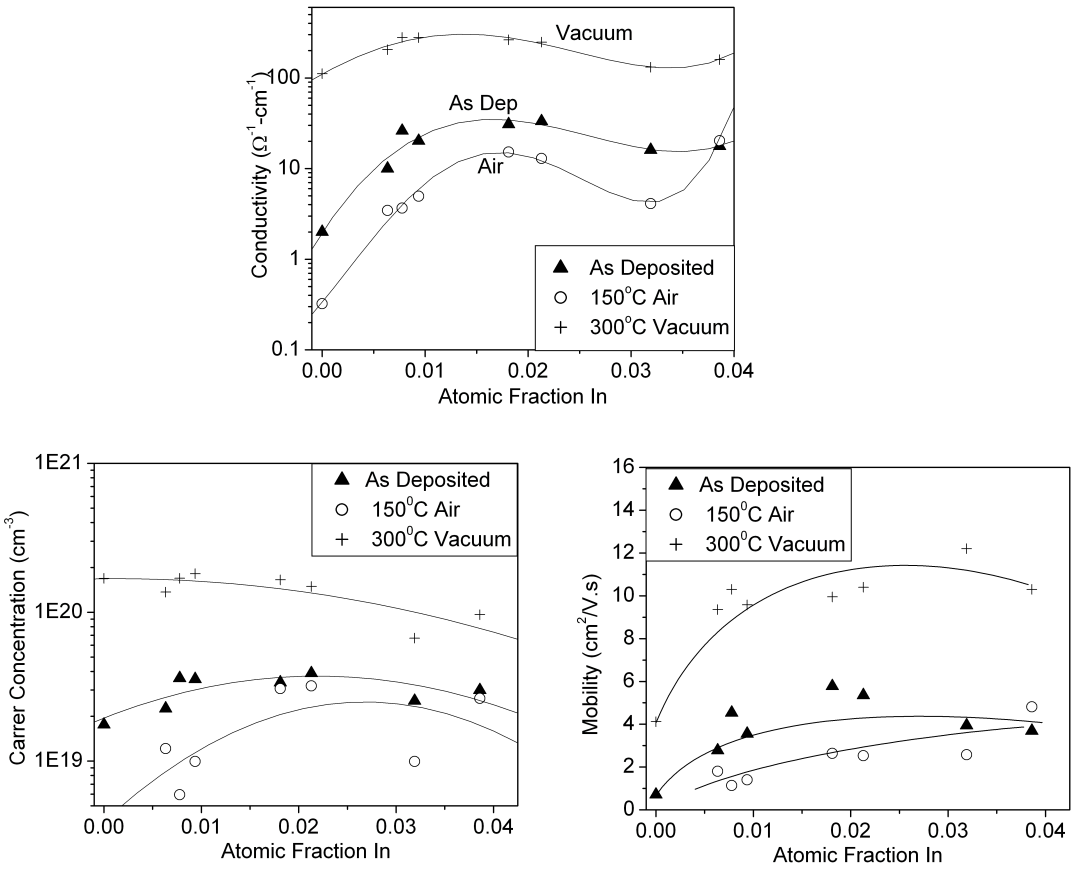

Figure 5.4: The electrical properties as deposited, after annealing in air and after annealing in vacuum for samples with total dopant ($X_{Al} + X_{In}$) equal to 4%.

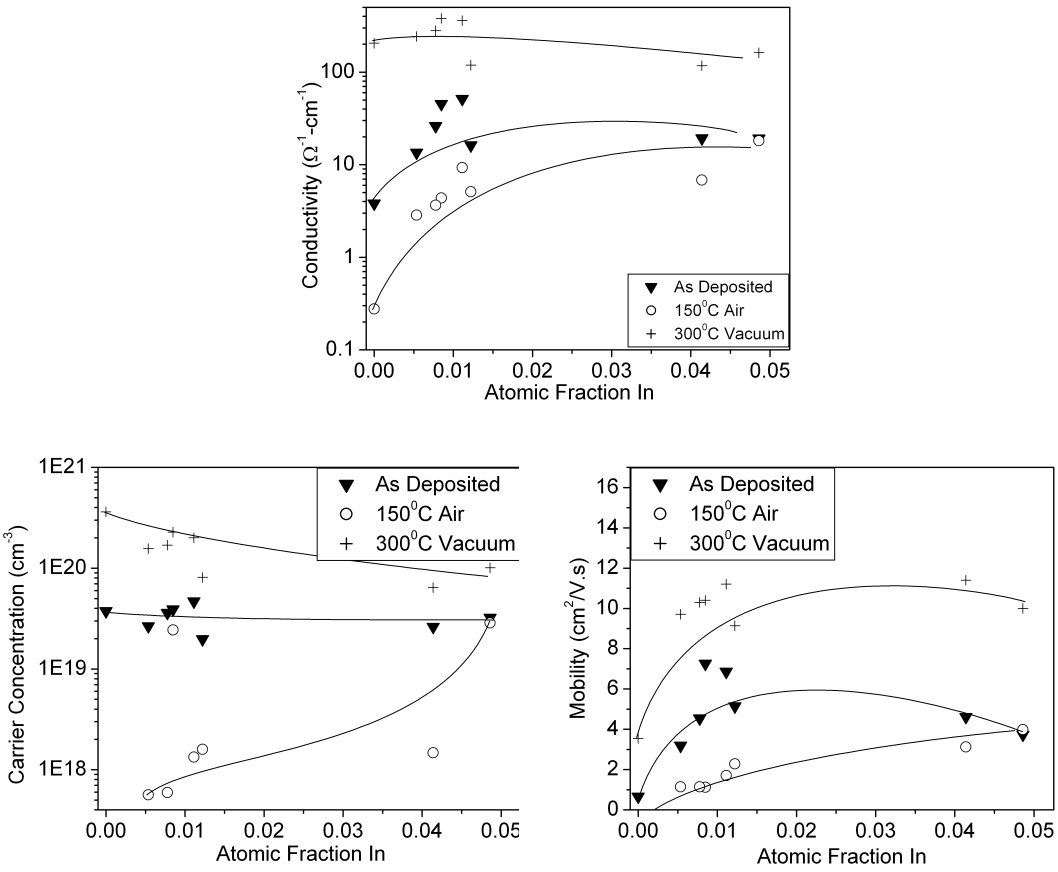

Figure 5.5: The electrical properties as deposited, after annealing in air and after annealing in vacuum for samples with total dopant ($X_{Al} + X_{In}$) equal to 5%.

the improvement in resistivity is due to both an improvement in the mobility and the carrier concentration. For the Al doped sample, the Hall voltage was too small to measure resulting from poor conductivity and low Hall mobility. In examining the data further, it can be seen that the carrier concentration was very stable after annealing for 2% and higher In. The mobility seems to increase consistently with increased In content. When annealed in vacuum, the carrier concentration increases with high Al content while the mobility increases with added In content. This results in the minimum that is seen around 1% In content. At this level, the carrier concentration remains high and the mobility has increased dramatically over the Al only doped sample.

Figure 5.5 shows the electrical properties for the 5% cross section plotted as a function of In content. Again, there is a significant decrease in the resisitivity when adding 1% In. This is true for both the as deposited and the air annealed data. Again, there is an increase in mobility that occurs with added In. The vacuum anneal again greatly improves the electrical properties. After vacuum anneal, the carrier concentration improves with higher Al content while the mobility improves with added In.

From Figures 5.3 through 5.5, it can be seen that adding 1% In improves the conductivity of ZnO. In order to further examine the role of Al with 1% In doping, the electrical properties of ZnO doped with 1% In are plotted as a function of the atomic fraction of Al in Figure 5.6. The mobility and carrier concentration after air annealing have not been included. The conductivity before and after annealing increases with increased Al content. The trend appears similar to the Al only case with a significant increase in conductivity from 1% to 1.8% with a continual, but less increase above this amount. The mobility follows a similar trend with a decrease in mobility occurring above 4.5% Al content. This 4.5% is 3 times the Al content for the maximum mobility

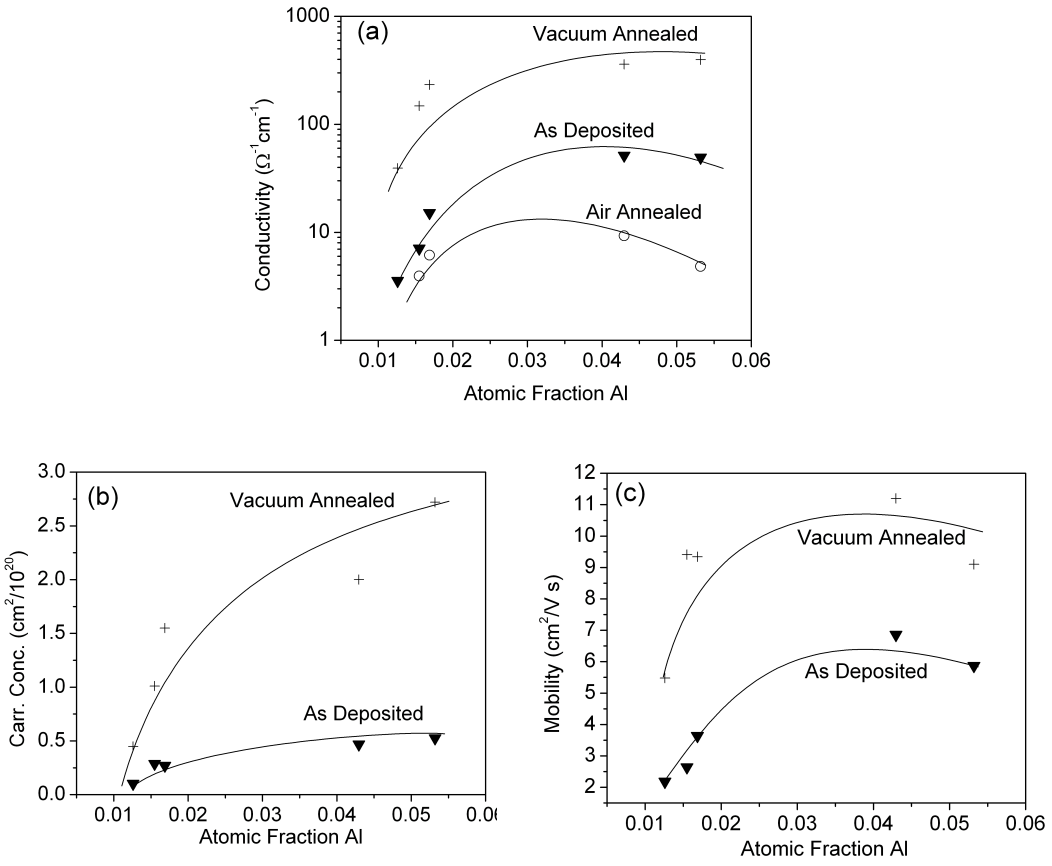

Figure 5.6 Electrical properties of the (Al,In): ZnO composition spread as deposited, after annealing at 150ºC in air and after annealing at 5×10^{-6} torr at 300°C for 1 hour for all data with an In content of 1% ($X_{In} = 0.01$). The (a) conductivity, (b) carrier concentration, and (c) mobility were all obtained from Hall measurements using the van der Pauw technique.

for the Al only doped sample. Over the entire range, the carrier concentration continues to increase with Al content; In particular, by increasing the Al content by 6 times (1% to 6%), the carrier concentration increased by almost 6 times (0.45×10^{20} to 2.7×10^{20}). Comparing Figure 5.6 with Figure 4.1 supports that adding 1% In to Al doped ZnO improves the solubility of Al. By adding 1% In, the amount of Al that can be added before a decrease in mobility occurs increases from 1.5% to 4.5%.

In general, the annealing data for this composition spread shows several trends. First, the data suggests that for Al doped ZnO, the best conductivity occurs at 1.5% Al content. Above this amount, the carrier concentration levels off and the mobility drops substantially. This is true for as deposited and after annealing in air or vacuum. This suggests that the solubility of Al in the given films is about 1.5% and that above this level, Al is no longer activated; either precipitates of Al_2O_3 form or some other complex forms, which causes scattering and degrades the mobility. For In doped ZnO, the conductivity improves with added In for the entire range. The carrier concentration does not improve significantly with added In, which suggests that non-activated In precipitates do not degrade the mobility in a way similar to Al_2O_3. In doping also shows much greater electrical stability in air than for Al doping.

The codoped sample seems to follow from the above trends. Al doping tends to result in high carrier concentrations with the strong possibility of degraded mobility. In doping tends to have higher mobility with lower carrier concentration. Codoping seems to suggest that adding a small amount of In to highly Al doped ZnO results in improved mobility and high carrier concentration. For the as deposited film, codoping improved both the carrier concentration and the mobility substantially, resulting in much improved conductivity for the codoped film. After annealing in air, a small amount of In greatly improved the conductivity of Al doped ZnO. Although the conductivity of the codoped film was lower than for In only doped ZnO, codoping

does improve the stability of Al doped ZnO and might be used for applications in which cost is an issue – 1% In is much better than 3 or 4%.

5.3Codoping and Hydrogen Annealing

Typically, ZnO films used for high conductivity applications are annealed in reducing gases, particularly H_2. Some of the samples from the composition spread have been annealed in 6% H_2/Ar at 300 ºC for 1 hour. All samples showed greatly improved conductivity with mobilities around 10 cm^2/V.sec and carrier concentrations above 10^{20} cm^{-3}. For these samples, the conductivity showed a strong dependence on thickness with the thinnest films showing the best conductivities. We interpret this to result from the shorter distance for H_2 to travel. This trend might also result from the thinner films having a different grain boundary structure. Trends with respect to composition were difficult to determine. In order to get around this thickness variation, 4 samples were chosen that had similar thickness. The thicknesses of the four samples were 200 +/- 20 nm. All four samples had resistivities of about 1×10^{-3} Ω-cm. The four samples had Al/In compositions of 1.8%/0%, 0%/3.1%, 1.9%/2.1% and 1.6%/1.0%. The fact that the resistivities after annealing in H_2 depended strongly on thickness and not on composition supports the suggestion that hydrogen acts as an electron donor.

In order to determine if codoping improves the stability of highly conductive films that have been annealed in a common reducing gas, the four samples were subsequently annealed in air at increasing temperatures for 1 hour each temperature. The temperature of the anneal as a function of time is shown in Figure 5.7. The electrical properties of the four samples were measured during the anneal using a “half van der Pauw” approach as in the inset of Figure 5.7. For uniform samples, the measured voltage is exactly proportional to the resistivity of the film. Figure 5.8 shows the measured voltage as a function of time for one of the four samples. For the short

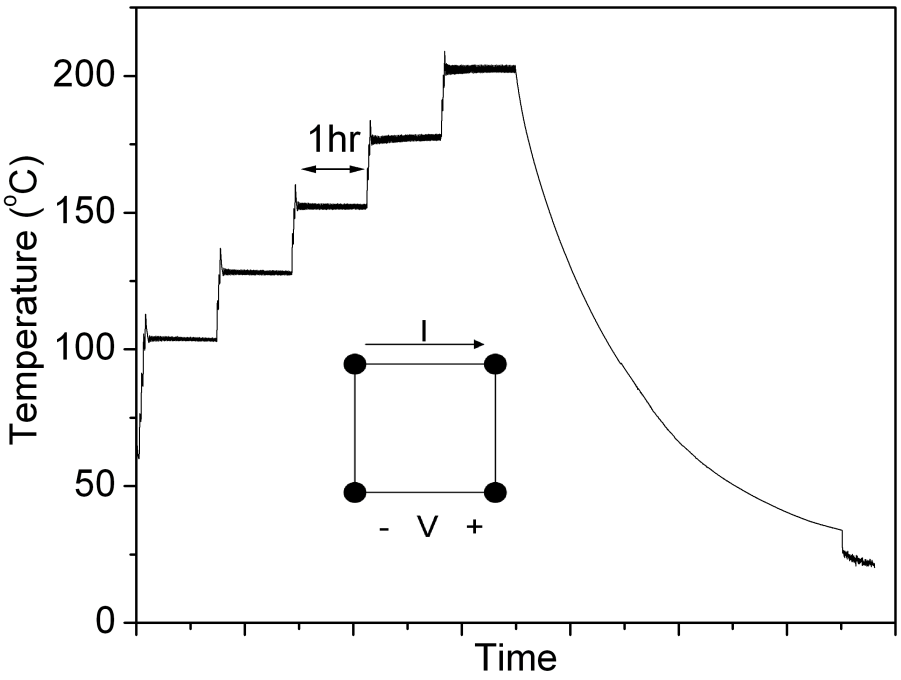

Figure 5.7: Temperature as a function of time for annealing in air after annealin in 6% H_2 at 300°C. Temperatures were held constant for 1 hour increments. The inset shows a schematic of the "half van der Pauw" technique used for in situ electrical measurements.

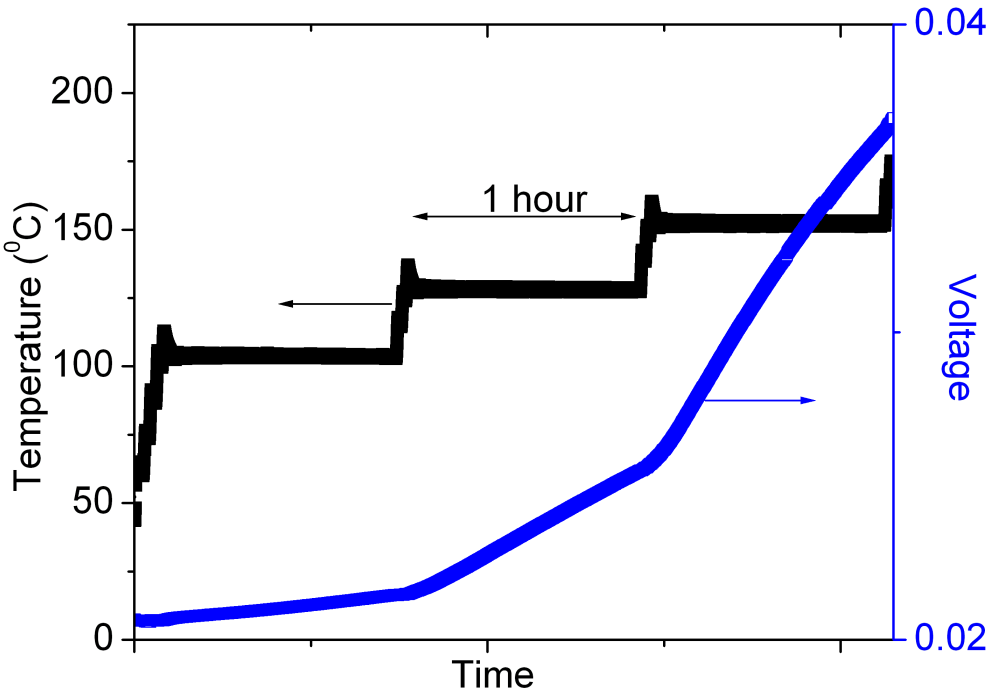

Figure 5.8: The measured voltage of a sample as a function of time using the experiment shown in Figure 5.7. The voltage change with time appears to be linear on this time scale.

time of 1 hour at these modest temperatures, the change in voltage with time is linear indicating incomplete diffusion or activation of the dopant.. In order to quantify the empirical stability of these films, the slope of these voltage curves with respect to time is plotted as a function of temperature in Figure 5.9. The voltage has been divided by the current in order to gain a more meaningful value of resistance. It is obvious that the Al doped film has very poor stability when compared to the other films. Surprisingly, both codoped samples have very similar curves that are much lower than that for even the In doped sample.

The data from Figure 5.9 suggests that codoped ZnO that has been annealed in hydrogen is more stable than Al or In only doped ZnO. This could be due to improved atomic structure. The crystal grain size might be larger in these films due to the lessened strain. This would result in fewer grain boundaries that act as high diffusivity paths for hydrogen or oxygen. This hypothesis has not been verified. The XRD equipment used does not have the resolution needed in order to determine grain size accurately.

5.4 Combinatorial Codoping Using On-Axis Sputtering

In order to further study the effects of codoping, a second combinatorial technique has been used. This second technique uses an on-axis 4-inch sputter source with a ZnO target. A pulsed DC power supply with a frequency of 250 Hz and a power of 350 W was used to get a near uniform ZnO layer on a 5 cm substrate. Al and In were introduced using 2 inch 90º off-axis sputter sources. This technique can be used to deposit a composition spread that has near uniform thickness with a near constant total dopant concentration (Al +In). The composition as a function location on substrate for a $Zn_{0.97}Al_xIn_yO$ sample, with x + y =0.03 is shown in Figure 5.10. A second sample was also successfully deposited for $Zn_{0.96}Al_xIn_y$ O sample, with x + y =0.04. It was determined to be difficult to achieve well-controlled compositions for Al

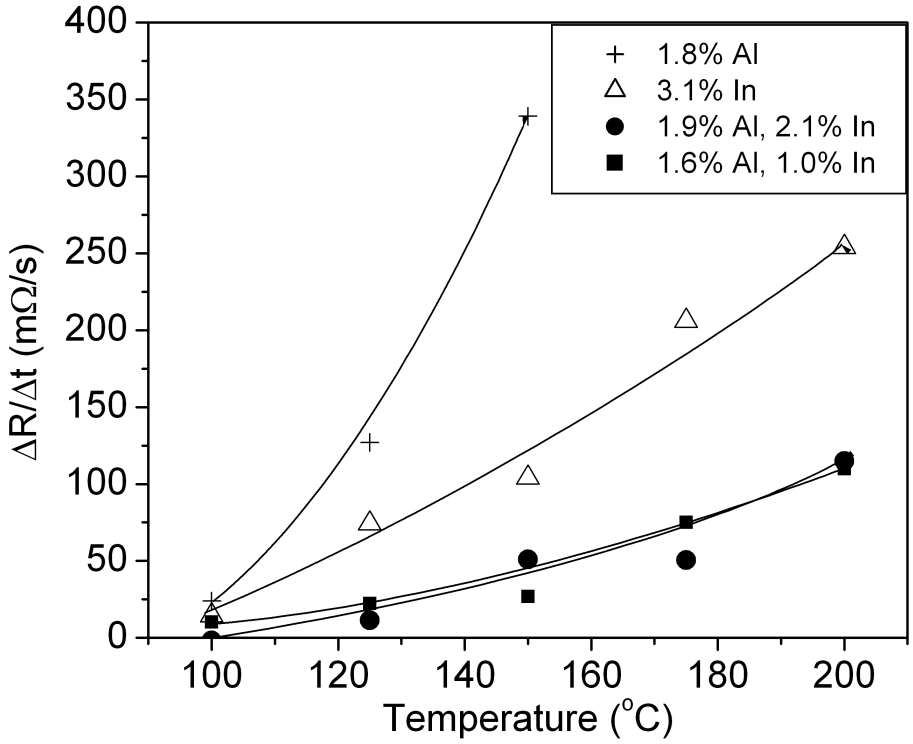

Figure 5.9: The change in resistance with time (slope from Figure 5.8) as a function of temperature for four doped ZnO samples. Both codoped samples were found to be more stable than Al or In doped samles. However, there is still a significant increase in resistance for even codoped samples at low temperatures.

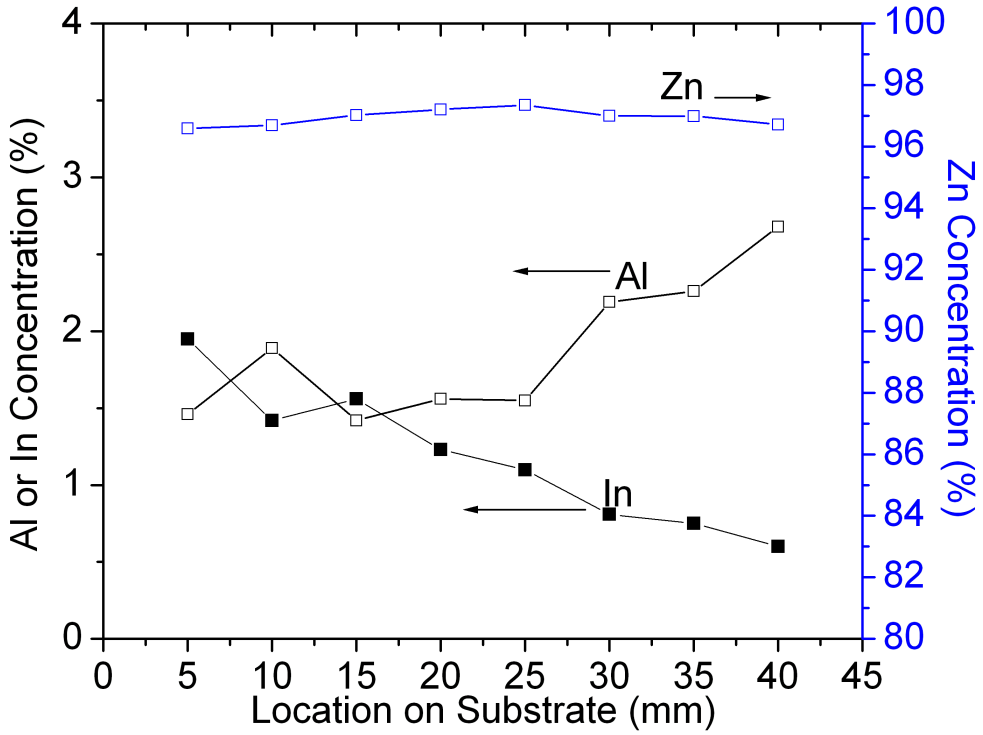

Figure 5.10: The Al, In and Zn concentration for a sample with a target Zn concentration of 97% (3% total dopant). There is a reasonably low variation in the Zn concentration and the general trend of increased Al:In ratio can be seen.

or In below about 1% for this technique due to the high ZnO deposition rate and the low Al or In rates needed. The XRD data showed that these samples were not highly textured as is typical for thin films – particularly films with hexagonal crystal structures. The system shows no measurable variation in the crystal quality as measured with the GADDS system. The lattice constants again increased with increased In concentration – decreased with increased Al concentration.

The substrates used were strips of Corning E-2000 that were 50 mm long and 5 mm wide. The resistivity after annealing in 6% H_2 in Ar for 1 hour at 300°C as a function of In content is shown for each sample in Figure 5.11. It can be seen that both samples have a trend that shows improved resistivity as a function of In content. The sample with higher total content shows improved resistivity. This suggests that the Al is indeed playing some role in improving the electrical properties as well. Unfortunately, the end members for these samples have not been achieved on the sample.

In order to study the stability of the electrical properties of these materials, contacts were made on the sample in a line as in Figure 5.12. The contact to contact distance was 5 mm. Robust contacts were made using a silver epoxy and verified by verifying that the voltage at each contact as a function of current is linear. A current was applied between the end contacts and voltages at each contact were measured. The electrical measurement could be measured during high temperature annealing. This measurement mimics a standard four-point probe measurement. The voltage between two contacts is then proportional to the resistivity of the film between those contacts.

The samples were then annealed in air at 100 °C, 150 °C and 200 °C, cooling to room temperature between each anneal. The contact to contact voltage at room

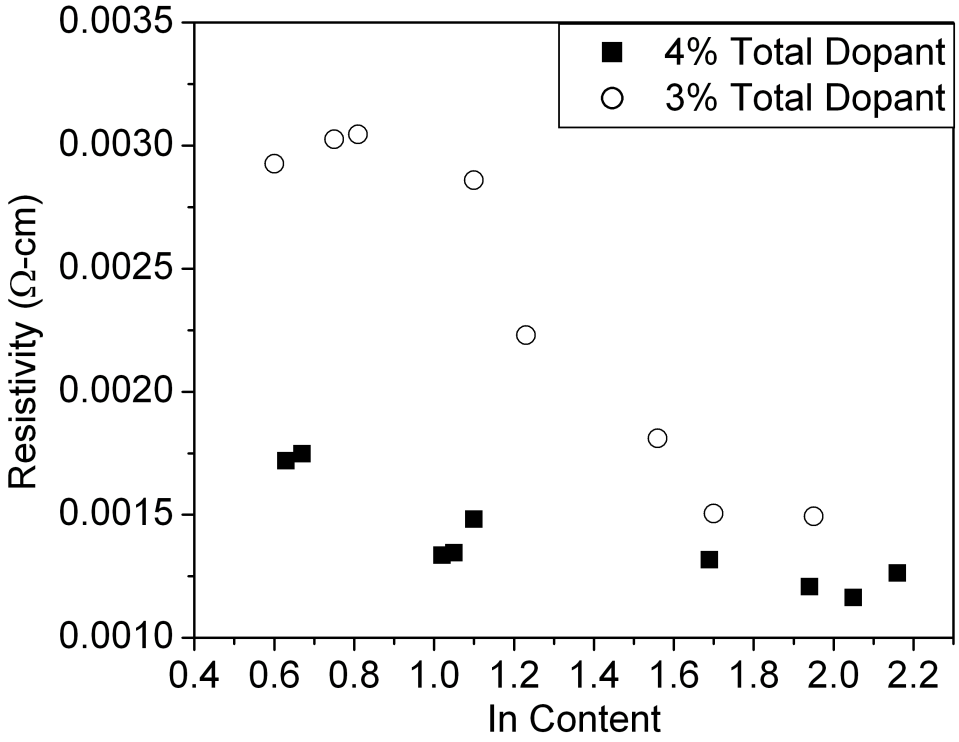

Figure 5.11: The resistivity as a function of In concentration for a sample with 3% total dopant and 4% total dopant after annealing in 6% H_2 in Ar. Both samples trend toward improved resistivity with greater In concentration. The 4% sample shows improved resistivity over the 3% sample suggesting that Al does improve the electrical properties. The end members (pure Al or In) were not achieved on these samples.

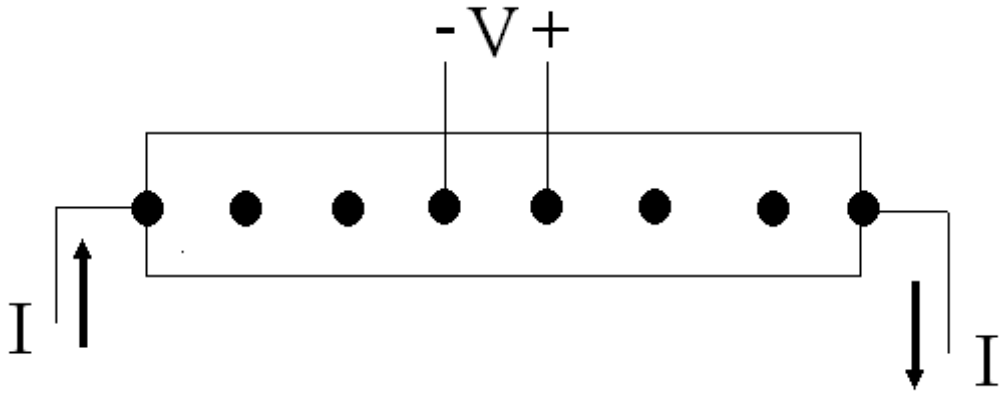

Figure 5.12: Schematic of experimental electrical technique for in situ high temperature anneals. A current is applied between the edge contacts while the voltages are measured at each inner contact. This technique mimics a standard linear four-point probe technique.

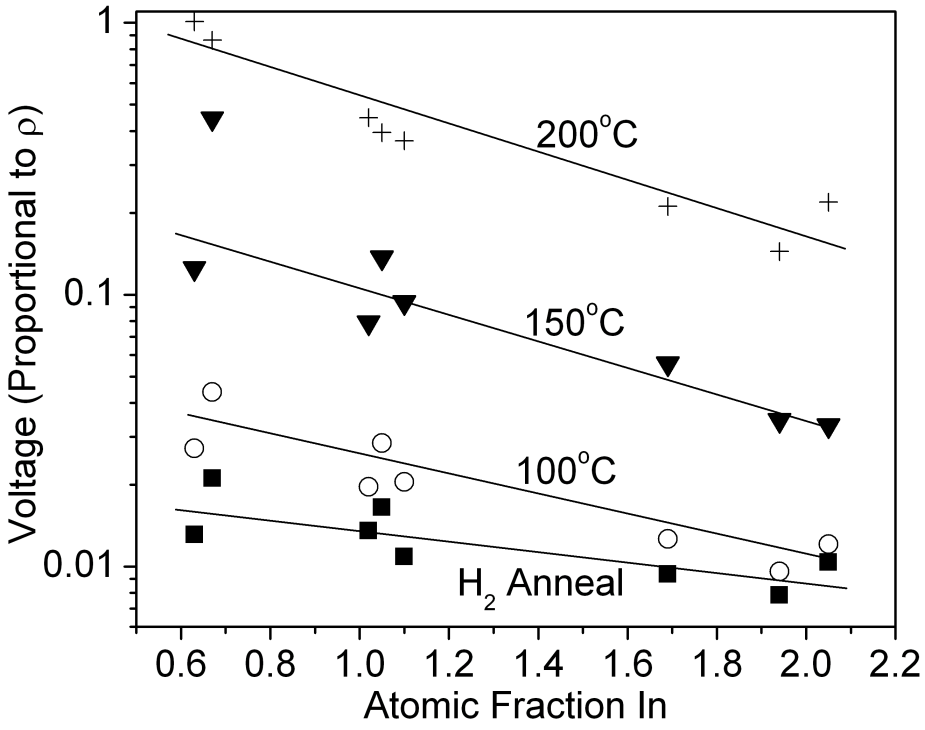

Figure 5.13: The measured voltage (proportional to resistivity) as a function of the atomic fraction of In after H_2 anneal and three temperatures in air for the 3 percent total dopant sample.

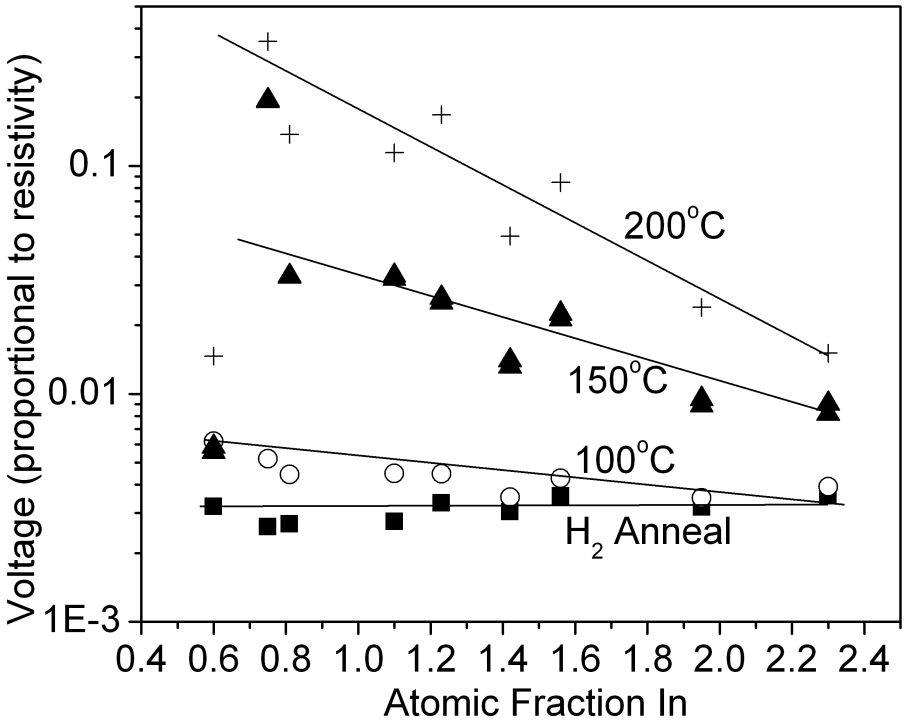

Figure 5.14: The measured voltage (proportional to resistivity) as a function of the atomic fraction of In after H_2 anneal and three temperatures in air for the 4 percent total dopant sample.

temperature following each anneal is plotted as a function In concentration for each sample in Figure 5.13 and Figure 5.14. For these samples, the trend of improved resistivity with higher In content remains after annealing in air. For the 3% total dopant film, the electrical properties again show a trend of being more stable with increased In content. For this sample, the area with only 0.6% In also appears to be very stable. It is unclear why this is. This value does correspond to the area of greatest improvement in the electrical properties in the first composition spreads. For the 4% total dopant sample, the stability does not seem to be improved with increased In concentration. The increase in resistivity appears to be roughly the same over the entire sample.

5.5 Conclusions

The effect of Al and In doping on the electrical stability of ZnO has been studied using combinatorial techniques. The effect of annealing in air, vacuum and hydrogen has been systematically studied. It has been found that In doped ZnO has much more stable electrical properties at high temperature in air than Al doped ZnO. For codoping, increasing the concentration of In was found to increase the mobility, however, having a high Al concentration results in higher carrier concentrations. Annealing the samples in hydrogen resulted in much improved conductivities.

CHAPTER 6

DENSITY FUNCTIONAL THEORY OF CODOPED ZINC OXIDE

6.1 Introduction

Density functional theory (DFT) has become a common method to calculate the electronic structure of many condensed matter systems [129]. DFT is a quantum mechanical approach to calculating electronic properties that is based on the Hohenbberg-Kohn theorem [130] and the Kohn-Sham equations [131]. These theorems state that the ground state of a many-electron system depends only on functionals of the electron density. This results in the ground state depending on the electron density that has only three spatial coordinates instead of the many-body wavefunction for N electrons with 3N spatial coordinates. This greatly decreases the computational power needed to calculate the electronic ground state of many systems. This theory and subsequent approximations, along with increased computer speed, has led to a huge increase in the number of condensed matter systems being studied using a first-principle approach.

The calculations presented here were completed using the local density approximation (LDA). This approximation assumes that the functionals depend only on the spatical coordinates where the functional is being evaluated. This approximation is commonly used and is fairly robust. However, LDA fails to describe systems with localized d and f electrons, leading to errors in electron energies. Most often this error results in underestimation of energy band gaps. Often, this is partially corrected by adding a intra-atomic charge to the atomic system. This technique is typically coined LDA+U. There is still some debate as to the most accurate method to determine the correct U term to add to the system.

The calculations have been completed using the Vienna ab-initio simulation package (VASP). VASP performs DFT type molecular dynamics simulations using pseudopotentials or the projector-augmented plane wave method and a plane wave basis set. Here we use the highly accurate projector-augmented plane-wave method. Using this method, one defines the starting lattice geometry and ionic placement. VASP uses period boundary conditions; therefore, supercells must be used to control the concentration of any defect to be studied. The number and location of k-points and the pseudopotentials or projectors are introduced for the calculation. The final energy and structure calculated will depend on both the number of k-points and the cut-off energy, which defines the maximum plane wave energy used in the basis set. The higher the number of k-points and the higher the cut-off energy, the more converged is the calculation. Steps should be made to verify that the energy of the system studied has converged to a reasonable accuracy with the cut-off energy and the number of k-points, as well as system size for defects.

Our experimental results suggested that codoping is beneficial over doping with a single dopant. DFT has been used to determine if codoping is energetically favorable. For various size of supercell, we have calculated the energy, volume and DOS for the relaxed cell for various cases. Al, In and Ga have been added as substitutional dopants on Zn lattice sites. Codoping has been studied by adding two dopants to a single supercell. Various lattice sites have been studied to vary the distance between dopants. Both neutral and charged (achieved by removing an electron from the system) defects have been studied. The affect of adding an oxygen interstitial to an octahedral site has also been studied briefly.

6.1.1 Energy cut-off and k-point convergence

In order to ensure that the DFT calculations are accurate, energy convergence with respect to the cut off energy and the number of k-points was calculated. Energy

convergence was calculated for a single wurtzite unit cell with 4 total atoms. This unit cell contains 2 zinc and 2 oxygen. In order to verify accuracy when adding Al, Ga and In, energy convergence was also calculated with one zinc atom replaced by the substituting cation.

The k-points were chosen using the automatic mesh function incorporated in VASP. This mesh creates Γ centered Monkhorst-Pack grids. The number of subdivisions along each reciprocal lattice direction are given by:

$$\begin{aligned} N_1 &= \max\left(1, l * \left|\vec{b}_1\right| + 0.5\right) \\ N_2 &= \max\left(1, l * \left|\vec{b}_2\right| + 0.5\right) \\ N_3 &= \max\left(1, l * \left|\vec{b}_3\right| + 0.5\right) \end{aligned} \tag{6.1}$$

A grid of equally spaced k-points is then generated with the coordinates:

$$\vec{k} = \vec{b}_1 \frac{n_1}{N_1} + \vec{b}_2 \frac{n_2}{N_2} + \vec{b}_3 \frac{n_3}{N_3}$$

$$n_1 = 0..., N_1 - 1 \quad n_2 = 0..., N_2 - 1 \quad n_3 = 0..., N_3 - 1 \tag{6.2}$$

Convergence then just depends on the term l. The calculation becomes more accurate with more k-points. Figure 6.1 shows the energy convergence for Zn_2O_2, $AlZnO_2$, $InZnO_2$ and $GaZnO_2$ as a function of the mesh length *l*. The cut off energy for this convergence was 425 eV. It can be seen that the energy has converged to less than 1 meV/atom with $l = 20$.

The convergence for the cut-off energy is shown in Figure 6.2. The convergence was calculated with a k-point mesh length *l* of 30. The energy has converged to less than 1 meV/atom with a cut-off energy of 500 eV. This is significantly larger than the default value from any of the pseudopotential files, the greatest of which is 282eV. The standard energy cut-off and k-point mesh length for the remainder of the calculations have been chosen to be 500 eV and 20 respectively.

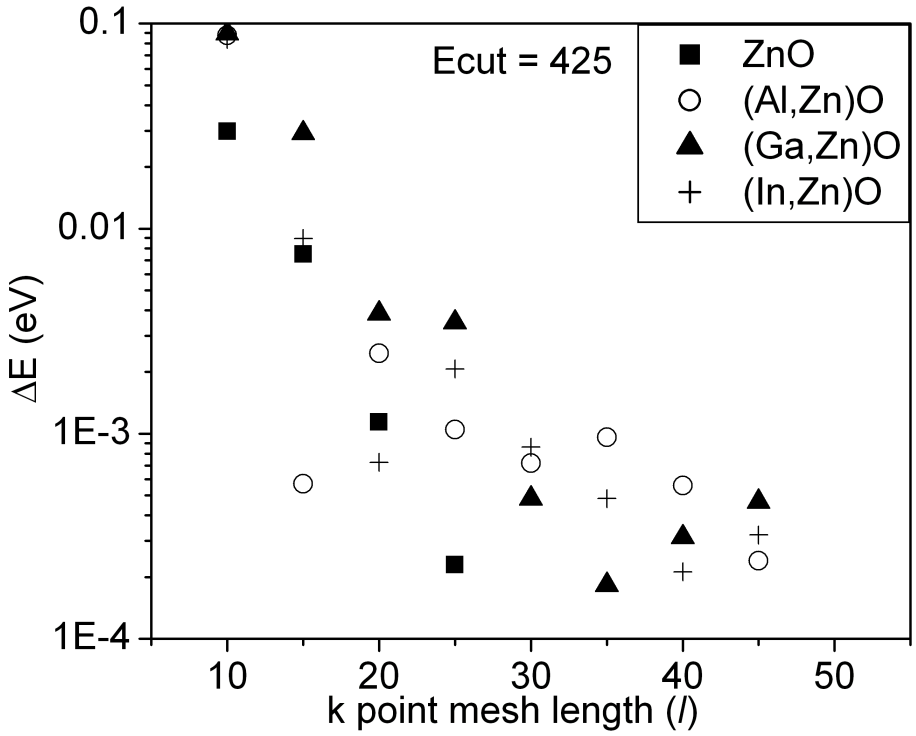

Figure 6.1: Energy conversion with number of k-point for calculations of desired materials with a cut-off energy of 425 eV and 4 atoms per unit cell. The energy has converged to less than 1 meV/atom with *l*=20.

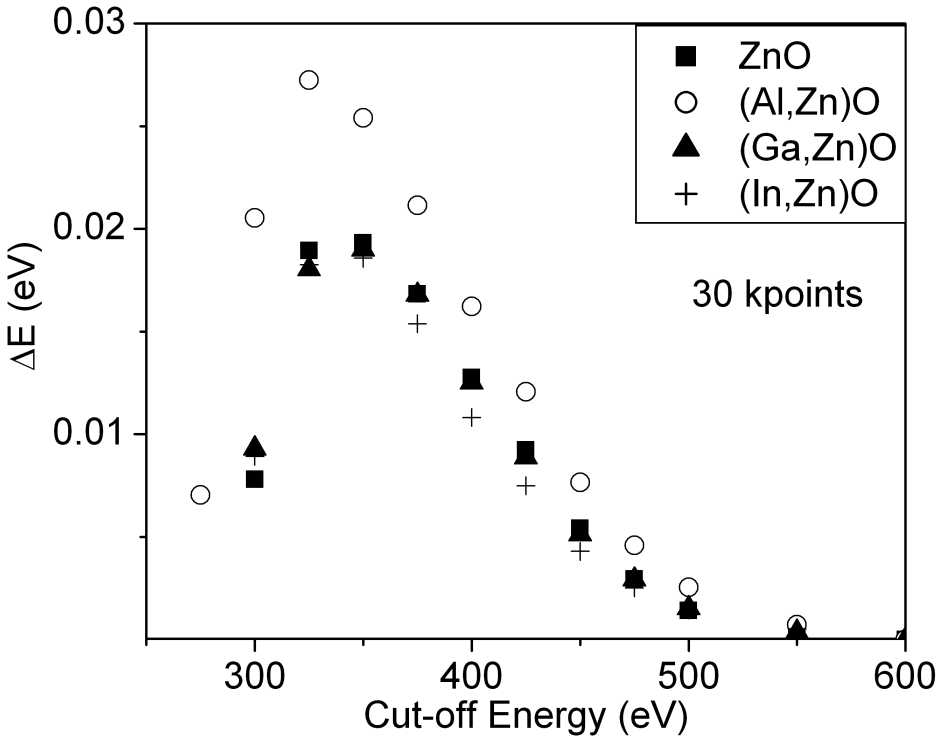

Figure 6.2: Energy conversion with the cut-off energy for calculations of desired materials with *l=25* for k-points and 4 atoms per unit cell. The energy has converged to less than 1 meV/atom with cut-off energy of 500 eV.

6.2 Energy Calculations

6.2.1 LDA Calculations of Codoped ZnO

DFT calculations were done to study the effect of codoping on the energy of ZnO. The experimental structure of ZnO is wurtzite, which has 2 zinc atoms and 2 oxygen per unit cell. In order to calculate the effect of doping at reasonable doping concentrations, a 3x3x2 supercell size was used for all calculations. This results in 36 zinc ions and substitutional dopant concentration of 2.78% or a single dopant or 5.56% for two dopants in a supercell. These concentrations correspond to the experimental data obtained for codoping ZnO. The ground state energy was calculated for the fully relaxed structure for ZnO with a single Al or In, two Al, two In and with both one Al and one In. For the cases with two dopants, calculations were completed with various configurations that correspond to increased distance between the dopants.

In order to determine if dopants tend to conglomerate within the lattice, the change in energy with increased distance for a volume relaxed cell is calculated and plotted in Figure 6.3. The energy difference is the difference in energy of a system with a cation spacing relative to the energy of the system with nearest neighbor distance for cations. The infinite distance values are taken from the single dopant case. Figure 6.3 shows that it is energetically expensive to bring the dopant ions together. In general, the energy decreases by 100 to 300meV when the dopants are not nearest neighbors. The energy does not change substantially for distances of 4.5 Å to 8 Å due to the supercell method resulting in a second defect – defect distance that decreases while this distance increases. It is not surprising that Al-Al or In-In tend to repel due to size constraints, however, this can not be driving force due to the fact that Al-In repel with a similar driving force.

The effect of distance between dopants can also be examined by plotting the formation energy of a single dopant as a function of concentration. For this case, a

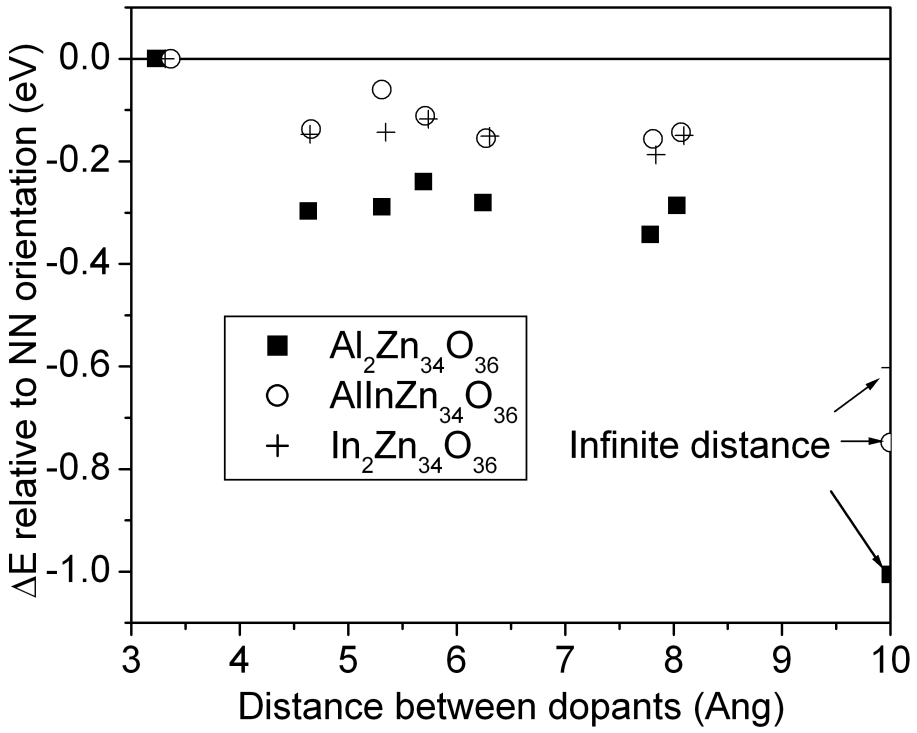

Figure 6.3: The change in energy with distance between dopant atoms relative to the nearest neighbor location. There is a strong repulsion between dopants.

single Al, In or Ga was added to supercells of different size. For a larger supercell, the distance between dopant ions increases. The formation energy change as a function of one over the distance between dopant ions is plotted in Figure 6.4. The data has been normalized to the smallest supercell size. It can be seen that the energy drops by more than 0.5eV when increasing the distance from 6 Å to 13 Å. The difference in Al, In and Ga can be partially explained by looking at the Bader charge. The Bader charge is a method of determining the charge associated with a given ion by finding maximums and minimums in the charge density function. For example, the Zn pseudopotential has 12 valance electrons. In a perfect ZnO wurtzite lattice, a Zn ion has a charge of 10.78. This means that the Zn ion has an effective charge of +1.22. For a single substitutional dopant in a 3x3x2 supercell, Al has a charge of +2.42, Ga of +1.76 and In of +1.70. The change in energy is plotted as a function of the effective charge over the distance in Figure 6.5. Although, the fit is relatively poor, a linear fit is added for each dopant type. It can be seen that the slope of each fit is approximately equal. The data do not line up exactly due to the fact that the energy is normalized to the smallest supercell size (large 1/r). This causes a shift in the curve proportional to the difference in charge between dopants. The constant slope between each dopant type suggests that the energy repulsive force is indeed close to coulombic, with the nonlinearity due to uncertainty in the calculations or the fact that the repulsion is screened. Al has the largest repulsive force while In has a smaller repulsive force. This data suggests that the charge repulsion is likely to have a stronger effect than pure size consideration as hypothesized.

In order to determine if size compensation still plays a role in determining the energetics of codoped ZnO, the energy as a function distance is compared for the following formula:

$$\frac{1}{2}(Al_2Zn_{34}O_{36} + In_2Zn_{34}O_{36}) \Leftrightarrow AlInZn_{34}O_{36} \qquad (6.3)$$

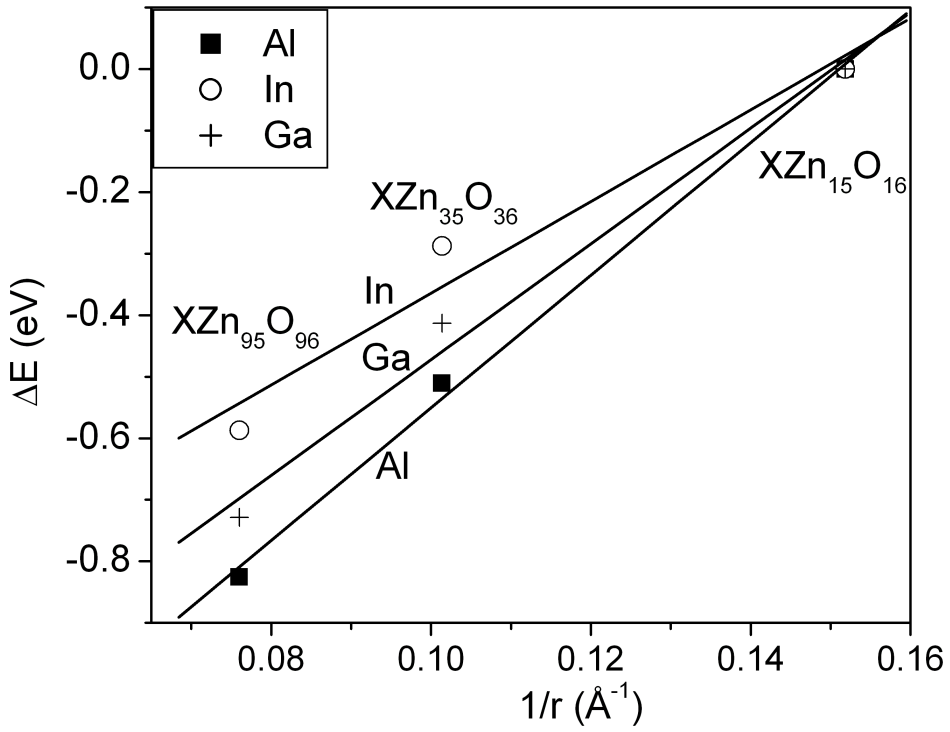

Figure 6.4: The change in formation energy with supercell size. The data is plotted as a function of one over distance between dopants due to periodic boundary conditions.

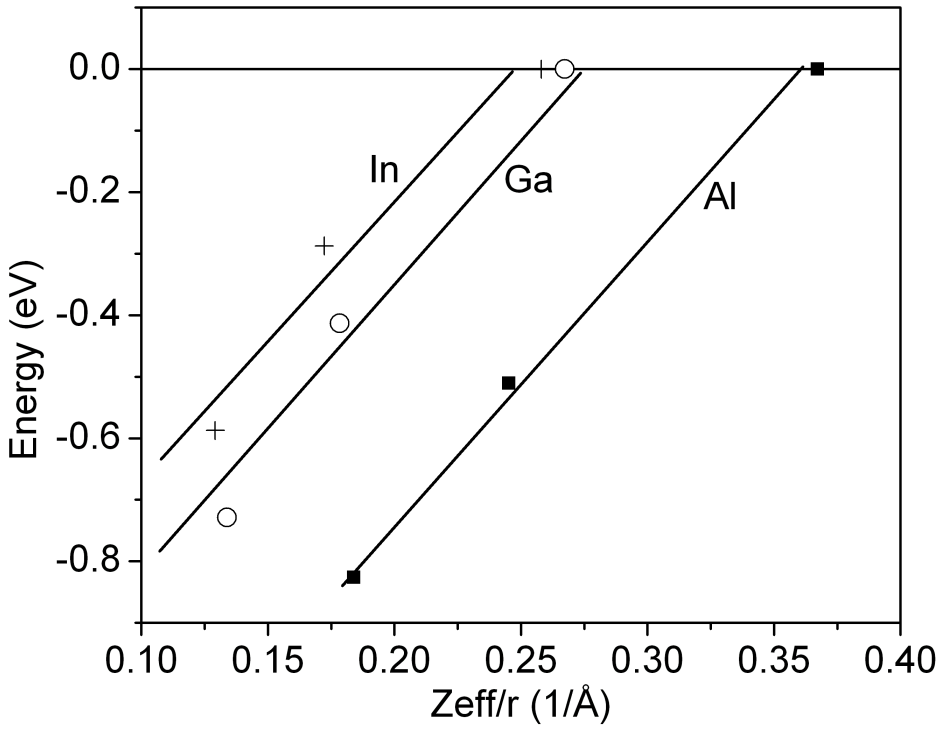

Figure 6.5: The change in formation energy versus one over the distance scaled by the effect charge (Z_{eff}) for Al, In, and Ga. A linear fit for each dopant type results in lines of similar slope. The difference in intercepts results from the normalization of the energy to the smallest distance (large 1/r).

Figure 6.6 shows the values of the calculated energy for these two energies as a function of distance between dopants. It can be seen that the difference in energy for each distance is less than 100 meV. The only data point that shows that codoping is energetically favorable is the nearest neighbor value.

6.2.2 LDA+U Calculation of Codoped ZnO

DFT with LDA has long been known to underestimate the band-gap of ZnO due to the poor representation of Zn *d* electrons. This can be partially corrected by using LDA+U. In order to study codoping with a more realistic ZnO lattice, a U value of 4.7eV has been chosen to be added to the Zn ions. This value corresponds to the value taken from Janotti et al [73]. This shifts the band gap from about 0.8eV to 1.5 eV, which is still much lower than the experimental value of about 3.4 eV. LDA+U was used to calculate the energy difference from Equation 6.3. When calculating this difference, it was found that the nearest neighbor codoped sample had an energy that was 0.9eV higher than that for the single dopant case. This does not support the hypothesis that codoping is energetically favorable.

6.3 Volume Calculations of Codoped ZnO

6.3.1 DFT Volumes compared to experiment

The energies of the doped ZnO lattices have been calculated by fully relaxing the atomic lattice of the supercell. The relaxed volume of a single unit cell is plotted in Figure 6.7 for the neutral Al or In on a Zn lattice site along with the codoped case. The volumes of the charged defects are plotted in Figure 6.8. The experimental values from Figure 4.6 are repeated in Figure 6.9. The scale of Figures 6.7, 6.8 and 6.9 are the same to allow for easy comparison. The values plotted in Figure 6.7 and 6.8 correspond to calculations using a 3x3x2 supercell using LDA+U. LDA + U was

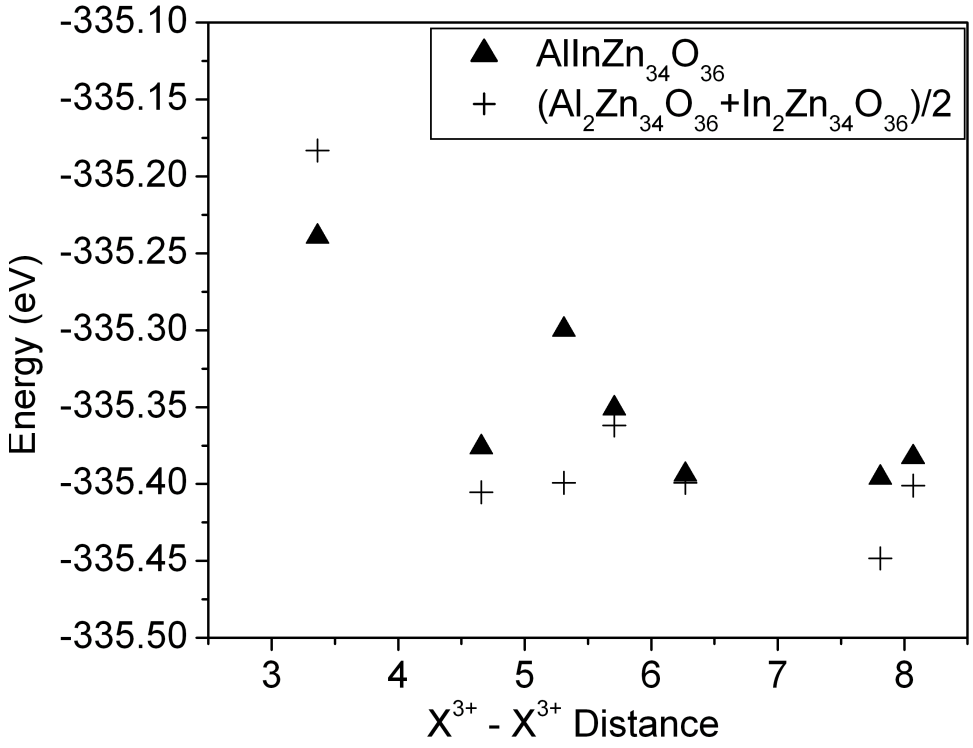

Figure 6.6: The change in energy as a function of distance for the codoped case compared to the average of the not codoped case with the same configuration. The energy difference is small. The only case that suggests that the codoping is beneficial is the nearest neighbor case.

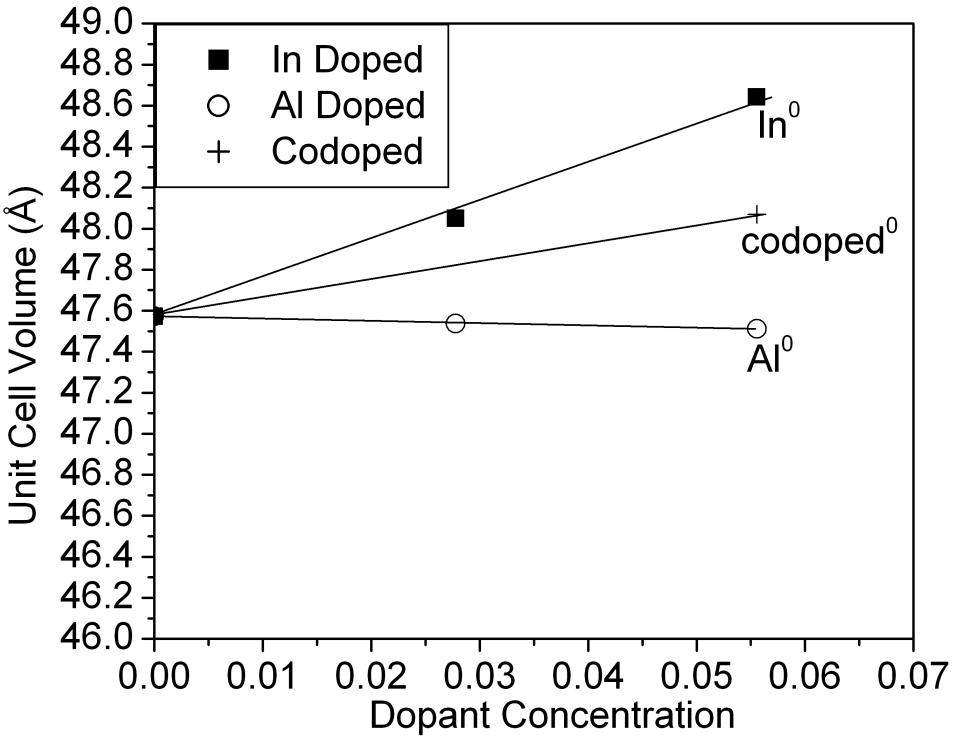

Figure 6.7: The calculated volume of a single supercell (3×3×2) as a function of dopant concentration for neutral Al, In and the codoped case using LDA+U. The volume change is seen to be larger for a neutral In than for a neutral Al.

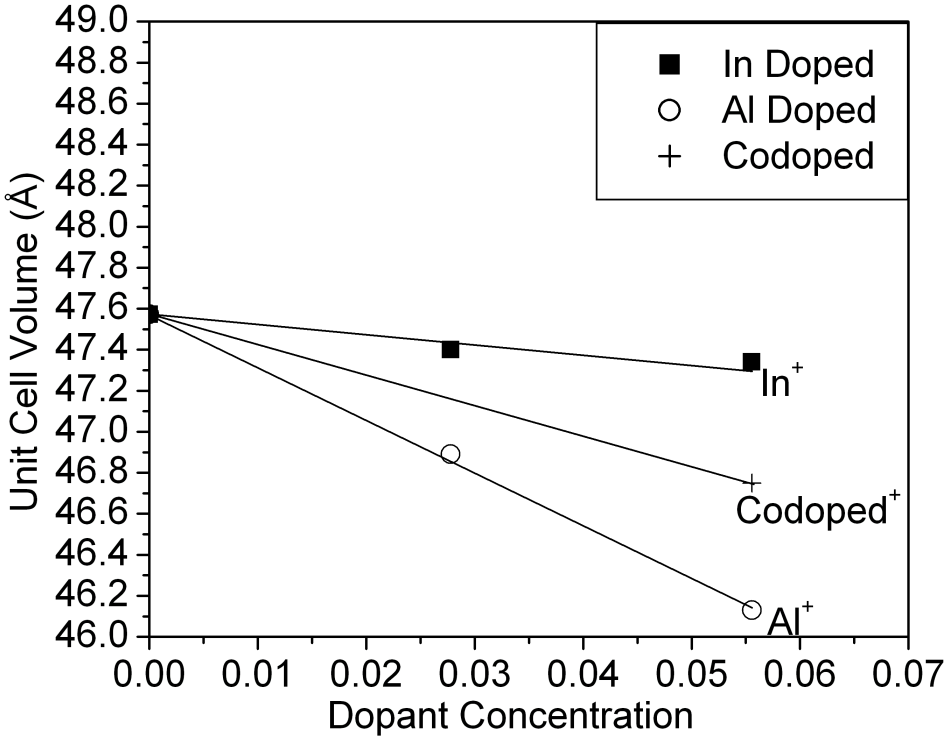

Figure 6.8: The calculated volume of a single supercell (3×3×2) as a function of dopant concentration for charged Al, In and the codoped case using LDA+U. The volumes were found to be smaller than for the neutral case.

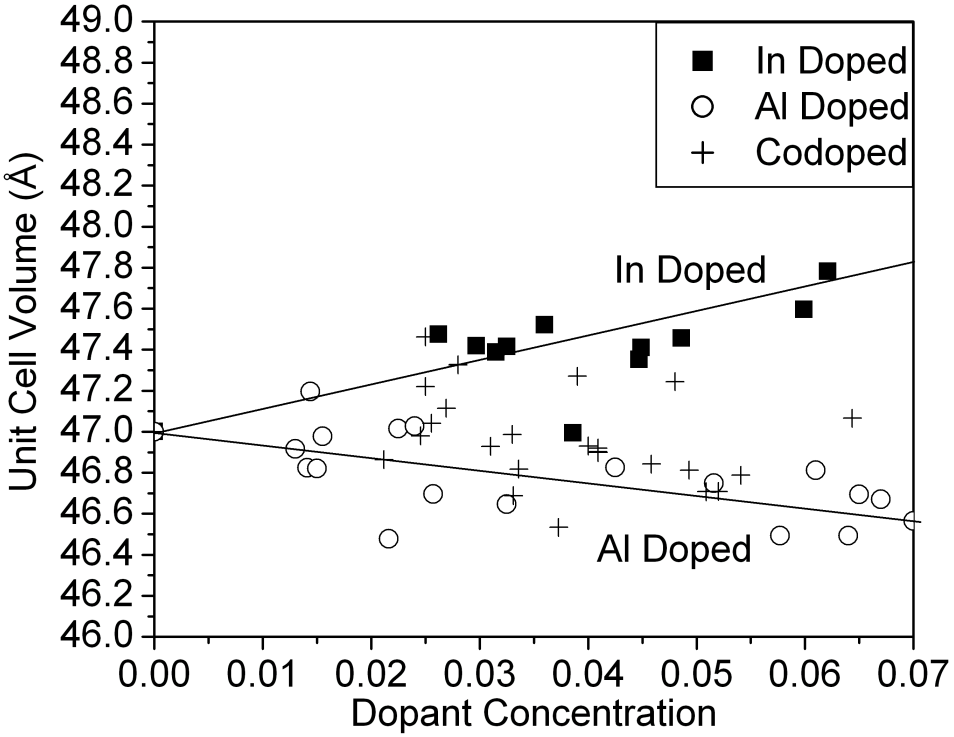

Figure 6.9: The volume of the unit cell of ZnO doped with Al, In and codoped with both Al and In as a function of dopant concentration. Doping with In increases the unit cell volume linearly while doping with Al decreases the unit cell volume linearly.

found to have improved agreement with experiment over LDA without corrections. Calculations were also completed with adding a U term to the In ions. The value for this U_{In} value was determined by using the atomic electron correlation energy energy from Janotti et al [73] and dividing by the ZnO dielectric constant. The U_{In} term had a negligible effect on the calculated volume and has not been included in the plot. This is also true for the calculated formation energy.

It can be seen that there is a significant change in the calculated unit cell volume when doping with Al or In. By comparing Figure 6.7 with Figure 6.8, there is reasonable agreement with the trend of Al or In doping between computed volumes with experimental volumes. The calculations also suggest that In has a large affect on the volume, with an increase of more than 2% for 5.56% doping. Al doping is seen to have a smaller effect, with only a small decrease in volume even at 5.56% dopant. This trend does not correspond with our hypothesis that ionic radius will be the leading cause volume changes. If this were true, Al3+ would have a larger effect than In3+ due to the larger difference in radius compared to Zn2+ (-30% compared to +10%).

The larger increase in volume associated with In doping and smaller decrease in volume associated with Al doping is likely attributed to the charge effects that are seen in the energy calculations. In particular, we found that two charged X^{3+} ions tend to repel each other. The Bader charge for Al^{3+} was found to be larger than for In^{3+}. This charge repulsion would be expected to result in an increase in volume of the unit cell. This effect is likely the cause of larger volumes than would be expected simply due to ionic radius arguments.

This effect is also seen when examining the volume of the charged defects. The charged defects are calculated by removing any excess electrons that result from doping. This decreases the repulsive charge and compacts the dopant ions. There is

obviously a significant decrease in volume of the unit cell when the dopant ions are charged. Comparisons between the experimental data and the theoretical data suggest that there is some fraction of dopant atoms (Al or In) that are not ionized and do not attribute to conduction. This is of course true; the measured carrier concentrations suggest that only a fraction of the dopants are actually ionized.

6.4 DOS for Codoped ZnO

DFT calculations also yield an estimate of the density of states (DOS). As discussed above, the band gap of ZnO calculated with DFT is known to be underestimated. LDA+U improves agreement with experimental values, however it is still more than a factor of 2 too small. However, an examination of the calculated DOS is meaningful. The integrated DOS are plotted in Figure 6.10 for each doped case along with ZnO. The origin of the ordinate corresponds to the top of the valence band. It appears from the plot, that the In^{3+} adds states that are deeper than those of Al^{3+}. The codoped sample appears to shift in a manner that is the superposition of the Al^{3+} and In^{3+}.

Plotting the formation energy as a function of the Fermi energy can also help to determine the location of a defect state in an energy gap. The formation energy for an substitutional Al with a charge q is given by:

$$E^{f}_{Al(Zn)} = E_{ZnO} - E^{q}_{Al(Zn)} + qE_{f} + \mu_{Al} - \mu_{Zn} \qquad (6.4)$$

The formation energy of the neutral and charged states for Al and In in ZnO are shown in Figure 6.11. Both the experimental and the theoretical (LDA+U) band gap are shown. It can be seen that both Al^{+} and In^{+} are stable until close to the experimental band gap. It can be seen that the Al^{+} to Al^{0} transition is shallower than the In^{+} to In^{0} transition. This supports the experimental data that shows that Al is easier to ionize and results in higher carrier concentrations.

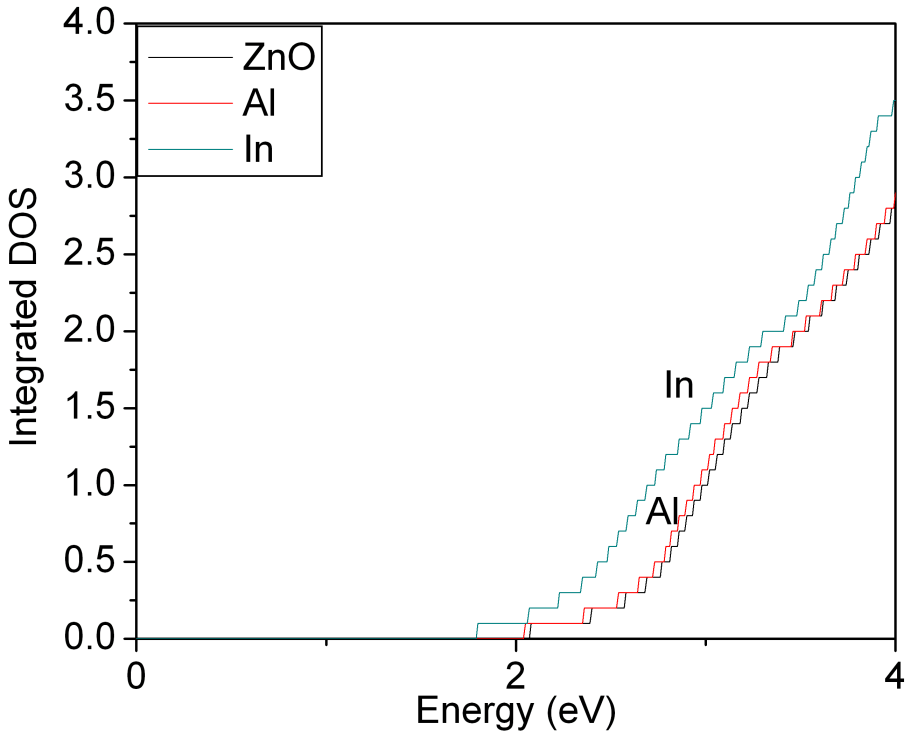

Figure 6.10: The integrated DOS for ZnO, ZnO: Al, and ZnO: In. The origin corresponds to the top of the valence band. This result suggests that In is a deeper donor than Al.

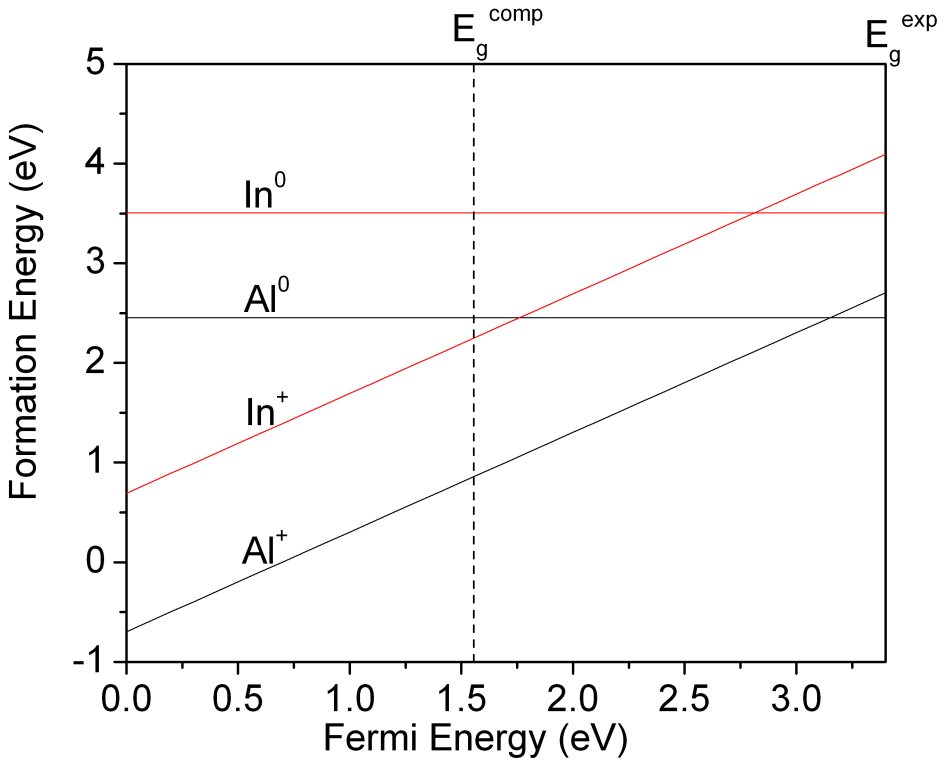

Figure 6.11: The formation of the neutral and charged Al and In defects on a Zn lattice site as a function of the Fermi energy. The computational (E_g^{comp}) and experimental (E_g^{exp}) bandgaps are shown. Both charged defects are stable for Fermi energies up to near the experimental bandgap. Al is a more shallow donor than In.

6.5 Doping of ZnO and the Oxygen Interstitial

Al and In have both been shown experimentally to be good donors in ZnO. However, typically, only a fraction of the dopant is actually ionized. This could be due to the Al or In precipitating out as Al_2O_3 or In_2O_3 or more likely being trapped at grain boundaries or associated with an oxygen interstitial. However, the stability of the carriers has been found to be very poor, even at temperatures low enough that should not allow significant diffusion of Al or In in the lattice. In order to study whether other compensating defects could play a large role, we studied the energetics of an oxygen interstitial with doping. The formation energy of an oxygen interstitial has been calculated using LDA. The formation energy within a given cell is given by:

$$E_O^f(lattice) = E(lattice) - E_O^0(lattice) + \mu_O \qquad (6.5)$$

Since comparisons between lattices are all that we desire, the chemical potential of oxygen is arbitrary and we can set $\mu_O = 0$. Table 6.1 summarizes the results.

Table 6.1: Formation Energy of Oxygen Octahedral Interstial In Various Lattices

Lattice	**E_O^f(lattice)**
ZnO	+6.16 eV (6.2eV) [117]
$AlZn_{35}O_{36}$	+2.12 eV
$InZn_{35}O_{36}$	+2.17 eV
$Al_2Zn_{34}O_{36}$	-6.03 eV
$In_2Zn_{34}O_{36}$	-5.17 eV
$AlInZn_{34}O_{36}$	-5.12 eV

For the calculations, all cation dopant ions were placed with a distance of ~5.7Angstroms (not nearest neighbors). The oxygen interstitial was placed in the octahedral location adjacent to the first dopant. It is obvious that the charge compensation that occurs when inserting oxygen is energetically favorable. When two

cation dopants are in the lattice, the oxygen interstitial is very energetically favorable. Comparisons between Al and In doping individually and codoping are difficult to interpret. With a single dopant, formation energy for each case are the same. For two dopants, there approximately 0.9eV difference between Al doping and In doping or codoping. It is difficult to determine how significant this difference due to the magnitudes of the formation energies. Again, the absolute values of these formation energies is meaningless without a finite chemical potential term for the added oxygen.

6.6 Conclusions

DFT calculations have been used to study codoping in ZnO. It was found that charge considerations greatly influence the structure and energy of the doped ZnO system. Bader charge analysis shows that the X^{3+} cation dopants repel each other in a manner that is proportional to the charge associated with the cation. This causes the volume of the doped lattice to be larger than one might expect simply due to ionic radius considerations. Looking at the charged defects (removing the excess electrons), the volume decreases substantially. The volumes calculated through DFT correspond well with experimental unit cell volumes if one considers that only a fraction of the dopants in the experimental material are activated.

Comparisons of the DOS and activation of donors suggests that Al acts as a shallower donor than In, which might explain the higher carrier concentrations for Al-rich ZnO compared to In-rich ZnO for the as deposited and vacuum annealed data. A brief study of oxygen interstitials and doping suggests that Al is more likely to accept an oxygen interstitial that acts to trap free electrons, causing the material to be insulating.

In conclusion, some understanding of the difference and interaction of dopants in highly doped ZnO has been gained. Calculations have not proven that codoping is beneficial over doping with Al or In individually. This study has not, however, been

an exhaustive study of codoping. Questions still remain as to how dopants react with point defects including oxygen interstitials and hydrogen. Understanding point defects is vital in understanding ZnO and its electrical properties.

CHAPTER 7

CONCLUSIONS

7.1 Status of a negative index of refraction in the far- infrared

A material with a negative index of refraction would be very technologically exciting. We have proposed a method of obtaining a negative index of refraction using only intrinsic materials properties. Our proposal involves combining a $SrTiO_3$ material which has an intrinsic dielectric resonance in the far-infrared with NiO, which has an intrinsic antiferromagnetic resonance in the far-infrared. It should be possible to shift the resonance frequencies of these materials through doping, temperature or applied magnetic field. We have proposed that a composite material of $SrTiO_3$/NiO can be fabricated as a thin film or as a bulk ceramic.

Fabrication of these composite materials has been completed. Several methods of measuring the permittivity and permeability of the composite material have been considered. Two of these methods have been used to attempt to measure the properties. The first was an FTIR system in reflection. The second was a time domain THz spectroscopy method that works in transmission. Neither method has proven successful in measuring thin film materials. $SrTiO_3$ materials are easy to measure in reflection modes due to a relatively high reflection signal, while NiO is easier to measure in transmission due to the very high transmission of THz radiation through NiO.

In conclusion, a material with a negative index of refraction in the far-infrared should be possible using only intrinsic materials properties. In order to do this, a combination of materials must be found that have a dielectric resonance and a magnetic resonance at the same frequency, and a method to measure these properties must be determined. Improving the ceramic material densities and improving the

signal-to-noise ratio of measurement techniques would aid in gaining meaningful permittivity and permeability data for this material combination.

7.2 Status of Codoped ZnO as a replacement for ITO

ZnO has been identified as a possible replacement for ITO in high-end applications such as flat-panel displays and solar cells. The low cost of ZnO is a huge advantage over the much more expensive ITO, which relies on scarce and expensive indium. Despite extensive research on ZnO in recent years, ZnO has still failed to replace ITO in standard flat-panel displays and many manufactured solar cells, even though careful processing of doped ZnO films can result in conductivities that approach those of ITO. Although improvements in conductivity are always desirable, the key problem with ZnO remains the stability of the electrical properties. The stability problem becomes more pronounced for FPD applications, which require very thin films.

We proposed that codoping might improve the conductivity and the stability of ZnO. Size compensation occurs with codoping with Al^{3+} and In^{3+}, due to Al^{3+} having an ionic radius 30% smaller than Zn^{2+} and In^{3+} having an ionic radius 10% larger. This effect has been studied by using a combinatorial approach using reactive off-axis r.f. sputtering. This technique offers a robust, rapid approach of studying effects of variations in composition. This method has been used to study ZnO with Al and In compositions that range from 1% to 7%.

Our results suggest that codoping with both Al and In is beneficial. As deposited codoped ZnO resulted in improved electrical properties with higher carrier concentration and mobility over either Al or In doping alone. Thermal stability tests have shown that Al tends to ionize more easily while also causing more scattering (if not ionized) than In. This was inferred from the fact that Al rich films had higher carrier concentrations and lower mobilities.

Density functional theory calculations help to explain Al and In as dopants in ZnO. It was found that charge, along with ionic radius, plays a significant role in determining the atomic structure of the doped Zno. The unit cell volume was found to be larger than one would expect if ionic radius alone is considered. This helps to explain why our best conductivities were found in an area where there is a significantly higher Al content than In. The computational study also supports the suggestion that Al is a more shallow donor than In, which would result in higher carrier concentrations for Al-doped ZnO than for In-doped ZnO. A brief study of oxygen interstitials using density functional theory shows how important point defects are in determining the electrical properties of ZnO. A single oxygen interstitial is found to be energetically favorable in highly doped ZnO and can compensate two donors.

In conclusion, codoping appears beneficial in controlling the electrical properties of ZnO. Improvements in the as-deposited film properties, along with improvements in the properties of films annealed in hydrogen or air indicate that a small amount of In added to highly Al doped ZnO has benefits. In order to definitively determine the role played by codoping, further experimentation must be done. Methods such as temperature dependent photoluminescence can be used to examine the presence and electronic state of defects, both intential (Al, In) and unintentional (oxygen vacancies, interstitials, hydrogen). In order to fully understand the role of dopants in ZnO, one must also fully understand the role of these point defects and their interaction with dopants.

REFERENCES

[1] S. Venzke, R. B. vanDover, J. M. Phillips, E. M. Gyory, T. Siegrist, C.-H. Chen, D. Werder, R. M. Fleming, R. J. Felder, E. Coleman, and R. Opila, "Epitaxial growth and magnetic behaviour of NiFe2O4 thin films," *Journal of Materials Research*, vol. 11, pp. 1187-1198, 1996.

[2] Y. Suzuki, "Epitaxial Spinel Ferrite Thin Films," *Annual Review of Material REsearch*, vol. 31, pp. 265-289, 2001.

[3] V. G. Veselago, "Electrodynamics of substances with simultaneously negative values of sigma and mu," *Soviet Physics Uspekhi*, vol. 10, pp. 509, 1968.

[4] J. B. Pendry, "Negative Refraction Makes a Perfect Lens," *Physical Review Letters*, vol. 85, pp. 3966-3969, 2000.

[5] R. W. Ziolkowski and A. D. Kipple, "Application of Double Negative Materials to Increase the Power Radiated by Electrically Small Antennas," *IEEE Transactions on Antennas and Propagation*, vol. 51, pp. 2626-2640, 2003.

[6] C. M. Krowne, "Electromagnetic-field theory and numerically generated results for propagation in left-handed guided-wave single-microstrip structures," *IEEE Transactions on Microwave Theory and Techniques*, vol. 51, pp. 2269-2283, 2003.

[7] J. B. Pendry, "Perfect cylindrical lenses," *Optics Express*, vol. 11, pp. 755-760, 2003.

[8] J. B. Pendry and S. A. Ramakrishna, "Refining the perfect lens," *Physica B: Condensed Matter*, vol. 338, pp. 329-332, 2003.

[9] R. A. Shelby, D. R. Smith, and S. Schultz, "Experimental Verification of a Negative Index of Refraction," *Science*, vol. 292, pp. 77-79, 2001.

[10] W. Park and J. Kim, "Negative-Index Materials: Optics by Design," *MRS Bulletin*, vol. 33, pp. 907, 2008.

[11] P. Chaturvedi, K. Hsu, S. Zhang, and N. Fang, "New Frontiers of Metamaterials: Design and Fabrication," *MRS Bulletin*, vol. 33, pp. 915, 2008.

[12] U. K. Chettiar, S. Xiao, A. V. Kildishev, W. Cai, H.-K. Yuan, V. P. Drachev, and V. M. Shalaev, "Optical Metamagnetism and Negative-Index Metamaterials," *MRS Bulletin*, vol. 33, pp. 921, 2008.

[13] T. Baba, T. Asatsuma, and T. Matsumoto, "Negative Refraction in Photonic Crystals," *MRS Bulletin*, vol. 33, pp. 927, 2008.

[14] L. Fok, M. Ambati, and X. Zhang, "Acoustic Metamaterials," *MRS Bulletin*, vol. 33, pp. 931, 2008.

[15] D. R. Fredkin and A. Ron, "Effectively left-handed (negative index) composite material," *Applied Physics Letters*, vol. 81, pp. 1753-1755, 2002.

[16] A. Alu and N. Engheta, "Pairing an Epsilon-Negative Slab With a Mu-Negative Slab: Resonance, Tunneling and Transparency," *IEEE Transactions on Antennas and Propagation*, vol. 51, pp. 2258-2271, 2003.

[17] R. C. LeCraw, E. G. Spencer, and E. I. Gordorn, "Extremely Low Loss Acoustic Resonance in Single-Crystal Garnet Spheres," *Physical Review Letters*, vol. 6, pp. 620, 1961.

[18] A. S. Barker and M. Tinkham, "Far-Infrared Ferroelectric Vibration Mode in SrTiO3," *Physical Review*, vol. 125, pp. 1527, 1962.

[19] A. J. Sievers and M. Tinkham, "Far Infrared Antiferromagnetic Resonance in MnO and NiO," *Physical Review*, vol. 129, pp. 1566-1571, 1963.

[20] C. R. Becker, P. Lau, R. Geick, and V. Wagner, "Antiferromagnetic Resonance in NiO:Co2+ and NiO:Fe2+," *Phys. Stat. Sol.*, vol. 67, pp. 653-663, 1975.

[21] W. Cochran, "Crystal stability and theory of ferroelectricity," *Advances in Physics*, vol. 9, pp. 387-423, 1960.

[22] A. S. Barker, "Infrared Dielectric Behavior of Ferroelectric Crystals," in *Ferroelectrics*, E. F. Weller, Ed. Amsterdam-London-New York: Elsevier Publishing Company, 1967, pp. 213-250.

[23] R. A. Cowley, "Lattice Dynamics and Phase Transistions of Strontium Titanate," *Physical Review*, vol. 134, pp. A981-A997, 1964.

[24] H. V. Alexandru, C. Berbecaru, F. Stanculescu, A. Ioachim, M. G. Banciu, M. I. Toacsen, L. Nedelcu, D. Ghetu, and G. Stoica, "Ferroelectric solid solutions (Ba,Sr)TiO3 for microwave applications," *Materials Science and Engineering B*, vol. 118, pp. 92-96, 2005.

[25] D. T. Margulies, "Origin of the anomalous magnetic behavior in single crystal Fe3O4," *Physical Review Letters*, vol. 79, pp. 5162-5165, 1997.

[26] M. T. Hutching and E. J. Samuelsen, "Measurement of Pin-Wave Dispersion in Nio by Inelastic Neutron-Scattering and Its Relation to Magnetic Properties," *Physical Review B*, vol. 6, pp. 3447, 1972.

[27] J. Sakurai, W. J. L. Buyers, R. A. Cowley, and G. Dolling, "Crystal Dynamics and Magnetic Excitations in Cobaltous Oxide," *Physical Review*, vol. 167, pp. 510, 1968.

[28] R. B. Van Dover and L. F. Schneemeyer, "The Codeposited Composition Spread Approach to High-Throughput Discovery/Exploration of Inorganic Materials," *Macromolecular Rapid Communications*, vol. 25, pp. 150-157, 2004.

[29] G. Haacke, "TRANSPARENT CONDUCTING COATINGS.," *Annual Review of Materials Science*, vol. 7, pp. 73-93, 1977.
[30] R. G. Gordon, "Criteria for Choosing Transparent Conductors," *MRS Bulletin*, vol. 25, pp. 52-57, 2000.

[31] K. L. Chopra, S. Major, and D. K. Pandya, "Transparent conductors--A status review," *Thin Solid Films*, vol. 102, pp. 1-46, 1983.

[32] C. G. Granqvist, "Transparent conductive electrodes for electrochromic devices: A review," *Applied Physics A: Materials Science & Processing*, vol. 57, pp. 19-24, 1993.

[33] T. J. Coutts, D. L. Young, and X. Li, "Characterization of Transparent Conducting Oxides," *MRS Bulletin*, vol. 25, pp. 58-65, 2000.

[34] A. J. Freeman, K. R. Poeppelmeier, T. O. Mason, R. P. H. Chang, and T. J. Marks, "Chemical and Thin-Film Strategies for New Transparent Conducting Oxides," *MRS Bulletin*, vol. 25, pp. 45-51, 2000.

[35] D. S. Ginley and C. Bright, "Transparent Conducting Oxides," *MRS Bulletin*, vol. 25, pp. 15-18, 2000.

[36] H. Kawazoe, H. Yanagi, K. Ueda, and H. Hosono, "Transparent p-type Conducting Oxides: Design and Fabrication of p-n Heterojunctions," *MRS Bulletin*, vol. 25, pp. 28-36, 2000.

[37] B. G. Lewis and D. C. Paine, "Applications and Processing of Transparent Conducting Oxides," *MRS Bulletin*, vol. 25, pp. 22-27, 2000.

[38] T. Minami, "New n-Type Transparent Conducting Oxides," *MRS Bulletin*, vol. 25, pp. 38-44, 2000.

[39] B. J. Ingram, G. B. Gonzalez, D. R. Kammler, M. I. Bertoni, and T. O. Mason, "Chemical and structural factors governing transparent conductivity in oxides," *Journal of Electroceramics*, vol. 13, pp. 167-175, 2004.

[40] H. L. Hartnagel, A. L. Dawar, A. K. Jain, and C. Jagadish, *Semiconducting Transparent Thin Films*: IOP Publishing Ltd, 1995.

[41] D. D. Edwards, T. O. Mason, F. Goutenoire, and K. R. Poeppelmeier, "A new transparent conducting oxide in the Ga2O3-In2O3-SnO2 system," *Applied Physics Letters*, vol. 70, pp. 1706-1708, 1997.

[42] X. Wu, T. J. Coutts, and W. P. Mulligan, "Properties of transparent conducting oxides formed from CdO and ZnO alloyed with SnO[sub 2] and In[sub 2]O[sub 3]," presented at The 43rd national symposium of the American Vacuum Society, Philadelphia, Pennsylvania (USA), 1997.

[43] T. Minami, "Transparent and conductive multicomponent oxide films prepared by magnetron sputtering," *Journal of Vacuum Science & Technology*, vol. 17, pp. 1765-1772, 1999.

[44] T. J. Coutts, D. L. Young, X. Li, W. P. Mulligan, and X. Wu, "Search for improved transparent conducting oxides: A fundamental investigation of CdO, Cd[sub 2]SnO[sub 4], and Zn[sub 2]SnO[sub 4]," *Journal of Vacuum Science & Technology A: Vacuum, Surfaces, and Films*, vol. 18, pp. 2646-2660, 2000.

[45] J. D. Perkins, J. A. Del Cueto, J. L. Alleman, C. Warmsingh, B. M. Keyes, L. M. Gedvilas, P. A. Parilla, B. To, D. W. Readey, and D. S. Ginley, "Combinatorial studies of Zn-Al-O and Zn-Sn-O transparent conducting oxide thin films," *Thin Solid Films*, vol. 411, pp. 152-160, 2002.

[46] A. Kurz and M. A. Aegerter, "Transparent conducting films in the Zn-Sn-O tie line," *Journal of Sol-Gel Science and Technology*, vol. 31, pp. 267-271, 2004.

[47] T. Moriga, Y. Hayashi, K. Kondo, Y. Nishimura, K.-i. Murai, I. Nakabayashi, H. Fukumoto, and K. Tominaga, "Transparent conducting amorphous Zn--Sn--O films deposited by simultaneous dc sputtering," *Journal of Vacuum Science & Technology A: Vacuum, Surfaces, and Films*, vol. 22, pp. 1705-1710, 2004.

[48] M. P. Taylor, D. W. Readey, C. W. Teplin, M. van Hest, J. L. Alleman, M. S. Dabney, L. M. Gedvilas, B. M. Keyes, B. To, P. A. Parilla, J. D. Perkins, and D. S. Ginley, "Combinatorial growth and analysis of the transparent conducting oxide ZnO/In (IZO)," *Macromolecular Rapid Communications*, vol. 25, pp. 344-347, 2004.

[49] H. Tetsuka, Y. Jin Shan, K. Tezuka, and H. Imoto, "Transparent amorphous conductive Cd-In-Sb-O thin films for flexible devices," *Vacuum*, vol. 80, pp. 1038-1041, 2006.

[50] Y. R. Ryu, S. Zhu, D. C. Look, J. M. Wrobel, H. M. Jeong, and H. W. White, "Synthesis of p-type ZnO films," *Journal of Crystal Growth*, vol. 216, pp. 330-334, 2000.

[51] L. L. Chen, Z. Z. Ye, J. G. Lu, and P. K. Chu, "Control and improvement of p-type conductivity in indium and nitrogen codoped ZnO thin films," *Applied Physics Letters*, vol. 89, pp. 252113-3, 2006.

[52] M. Kumar, T.-H. Kim, S.-S. Kim, and B.-T. Lee, "Growth of epitaxial p-type ZnO thin films by codoping of Ga and N," *Applied Physics Letters*, vol. 89, pp. 112103-3, 2006.

[53] D.-S. Liu, C.-S. Sheu, and C.-T. Lee, "Aluminum-nitride codoped zinc oxide films prepared using a radio-frequency magnetron cosputtering system," *Journal of Applied Physics*, vol. 102, pp. 033516-6, 2007.

[54] H. B. Ye, J. F. Kong, W. Z. Shen, J. L. Zhao, and X. M. Li, "Origins of shallow level and hole mobility in codoped p-type ZnO thin films," *Applied Physics Letters*, vol. 90, pp. 102115-3, 2007.

[55] Z. Z. ye, L. L. Chen, B. H. Zhao, and H. P. He, "Photoluminescence in heavily doped ZnO:N:In films," *Applied Physics Letters*, vol. 92, pp. 231913, 2008.

[56] E.-J. Yun, H.-S. Park, K. H. Lee, H. G. Nam, and M. Jung, "Characterization of Al-As codoped p-type ZnO films by magnetron cosputtering deposition," *Journal of Applied Physics*, vol. 103, pp. 073507, 2008.

[57] Y. J. Zeng, Z. Z. Ye, W. Z. Xu, J. G. Lu, H. P. He, L. P. Zhu, B. H. Zhao, Y. Che, and S. B. Zhang, "p-type behavior in nominally undoped ZnO thin films by oxygen plasma growth," *Applied Physics Letters*, vol. 88, pp. 262103-3, 2006.

[58] www.econstats.com: downloaded December 2008

[59] S. J. Pearton, D. P. Norton, K. Ip, Y. W. Heo, and T. Steiner, "Recent advances in processing of ZnO," *Journal of vacuum Science & Technology B: Microelectronics and Nanometer Structures*, vol. 22, pp. 932-948, 2004.

[60] T. Makino, Y. Segawa, A. Tsukazaki, A. Ohtomo, and M. Kawasaki, "Electron transport in ZnO thin films," *Applied Physics Letters*, vol. 87, pp. 022101-3, 2005.

[61] U. Ozgur, Y. I. Alivov, C. Liu, A. Teke, M. A. Reshchikov, S. Dogan, V. Avrutin, S.-J. Cho, and H. Morkoc, "A comprehensive review of ZnO materials and devices," *Journal of Applied Physics*, vol. 98, pp. 041301-103, 2005.

[62] P. Cheng, S. Li, L. Zhang, and J. Li, "Characterization of intrinsic donor defects in ZnO ceramics by dielectric spectroscopy," *Applied Physics Letters*, vol. 93, pp. 012902, 2008.

[63] X. Yang, G. Du, X. Wang, J. Wang, B. Liu, Y. Zhang, D. Liu, D. Liu, H. C. Ong, and S. Yang, "Effect of post-thermal annealing on properties of ZnO thin film grown on c-Al2O3 by metal-organic chemical vapor deposition," *Journal of Crystal Growth*, vol. 252, pp. 275-278, 2003.

[64] D. C. Look, J. W. Hemsky, and J. R. Sizelove, "Residual Native Shallow Donor in ZnO," *Physical Review Letters*, vol. 82, pp. 2552 LP - 2555, 1999.

[65] S. B. Zhang, S.-H. Wei, and A. Zunger, "Intrinsic n-type versus p-type doping asymmetry and the defect physics of ZnO," *Physical Review B*, vol. 63, pp. 075205, 2001.

[66] Y.-J. Lin, C.-L. Tsai, Y.-M. Lu, and C.-J. Liu, "Optical and electrical properties of undoped ZnO films," *Journal of Applied Physics*, vol. 99, pp. 093501-4, 2006.

[67] F. K. Shan, G. X. Liu, W. J. Lee, and B. C. Shin, "The role of oxygen vacancies in epitaxial-deposited ZnO thin films," *Journal of Applied Physics*, vol. 101, pp. 053106-8, 2007.

[68] L. Sun, W. Cheng, F. Lin, X. Ma, and W. Shi, "Changes of structure and optical energy gap induced by oxygen pressure during the deposition of ZnO films," *Physica B: Condensed Matter*, vol. 381, pp. 109-112, 2006.

[69] P. Cheng, S. Li, L. Zhang, and J. Li, "Characterization of intrinsic donor defects in ZnO ceramics by dielectric spectroscopy," *Applied Physics Letters*, vol. 93, pp. 012902, 2008.

[70] C. v. d. Walle, "Hydrogen as a cause of doping in zinc oxide," *Physical review Letters*, vol. 85, pp. 1012-1015, 2000.

[71] C. G. V. d. Walle, "Defect analysis and engineering in ZnO," *Physica B - Condensed Matter*, vol. 308, pp. 899-903, 2002.

[72] A. Janotti and C. v. d. Walle, "New insights into the role of native point defects in ZnO," *Journal of Crystal Growth*, vol. 287, pp. 58-65, 2006.

[73] A. Janotti, D. Segev, and C. G. V. d. Walle, "Effects of cation d states on the structural and electronic properties of III-nitride and II-oxide wide-band-gap semiconductors," *Physical Review B*, vol. 74, pp. 045202, 2006.

[74] S. F. J. Cox, E. A. Davis, S. P. Cottrell, P. J. C. King, J. S. Lord, J. M. Gil, H. V. Alberto, R. C. VilÃ£o, J. Piroto Duarte, N. Ayres de Campos, A. Weidinger, R. L. Lichti, and S. J. C. Irvine, "Experimental Confirmation of the Predicted Shallow Donor Hydrogen State in Zinc Oxide," *Physical Review Letters*, vol. 86, pp. 2601 LP - 2604, 2001.

[75] D. M. Hofmann, A. Hofstaetter, F. Leiter, H. Zhou, F. Henecker, B. K. Meyer, S. B. Orlinskii, J. Schmidt, and P. G. Baranov, "Hydrogen: A Relevant Shallow Donor in Zinc Oxide," *Physical Review Letters*, vol. 88, pp. 045504, 2002.

[76] E. V. Lavrov, J. Weber, F. Börrnert, C. G. Van de Walle, and R. Helbig, "Hydrogen-related defects in ZnO studied by infrared absorption spectroscopy," *Physical Review B*, vol. 66, pp. 165205, 2002.

[77] L.-Y. Chen, W.-H. Chen, J.-J. Wang, F. C.-N. Hong, and Y.-K. Su, "Hydrogen-doped high conductivity ZnO films deposited by radio-frequency magnetron sputtering," *Applied Physics Letters*, vol. 85, pp. 5628-5630, 2004.

[78] G. A. Shi, M. Stavola, S. J. Pearton, M. Thieme, E. V. Lavrov, and J. Weber, "Hydrogen local modes and shallow donors in ZnO," *Physical Review B*, vol. 72, pp. 195211, 2005.

[79] T. Minami, H. Sato, H. Nanto, and S. Takata, "Group-Iii Impurity Doped Zinc-Oxide Thin-Films Prepared by Rf Magnetron Sputtering," *Japanese Journal of Applied Physics Part 2-Letters*, vol. 24, pp. L781-L784, 1985.

[80] M. Hiramatsu, K. Imaeda, N. Horio, and M. Nawata, "Transparent conducting ZnO thin films prepared by XeCl excimer laser ablation," *Journal of Vacuum Science & Technology A: Vacuum, Surfaces, and Films*, vol. 16, pp. 669-673, 1998.

[81] P. Nunes, E. Fortunato, P. Tonello, F. Braz Fernandes, P. Vilarinho, and R. Martins, "Effect of different dopant elements on the properties of ZnO thin films," *Vacuum*, vol. 64, pp. 281-285, 2002.

[82] R. Tahar and N. Tahar, "Boron-doped zinc oxide thin films prepared by sol-gel technique," *Journal of Materials Science*, vol. 40, pp. 5285-5289, 2005.

[83] J. U. Brehm, M. Winterer, and H. Hahn, "Synthesis and local structure of doped nanocrystalline zinc oxides," *Journal of Applied Physics*, vol. 100, pp. 064311-9, 2006.

[84] T. Minami, H. Nanto, and S. Takata, "Highly Conductive and Transparent Aluminum Doped Zinc-Oxide Thin-Films Prepared by Rf Magnetron Sputtering," *Japanese Journal of Applied Physics Part 2-Letters*, vol. 23, pp. L280-L282, 1984.

[85] Z.-C. Jin, I. Hamberg, and C. G. Granqvist, "Optical properties of sputter-deposited ZnO:Al thin films," *Journal of Applied Physics*, vol. 64, pp. 5117-5131, 1988.

[86] T. Minami, K. Oohashi, S. Takata, T. Mouri, and N. Ogawa, "Preparations of ZnO:Al Transparent Conducting Films by D.C. Magnetron Sputtering," *Thin Solid Films*, vol. 193/194, pp. 721-729, 1990.

[87] J. Hu and R. G. Gordon, "Textured aluminum-doped zinc oxide thin films from atmospheric pressure chemical-vapor deposition," *Journal of Applied Physics*, vol. 71, pp. 880, 1991.

[88] W. Tang and D. Cameron, "Aluminum doped zinc oxide transparent conductors deposited by the sol-gel process," *Thin Solid Films*, vol. 238, pp. 83-87, 1994.

[89] K. H. Kim, K. C. Park, and D. Y. Ma, "Structural, electrical and optical properties of aluminum doped zinc oxide films prepared by radio frequency magnetron sputtering," *Journal of Applied Physics*, vol. 81, pp. 7764, 1997.

[90] H. Kim, C. M. Gilmore, J. S. Horwitz, A. Pique, H. Murata, G. P. Kushto, R. Schlaf, Z. H. Kafafi, and D. B. Chrisey, "Transparent conducting aluminum-doped zinc oxide thin films for organic light-emitting devices," *Applied Physics Letters*, vol. 76, pp. 259-261, 2000.

[91] A. E. Delahoy, S. Y. Guo, C. Paduraru, and A. Belkind, "Reactive-environment, hollow cathode sputtering: Basic characteristics and application to Al[sub 2]O[sub 3], doped ZnO, and In[sub 2]O[sub 3]:Mo," *Journal of*

Vacuum Science & Technology A: Vacuum, Surfaces, and Films, vol. 22, pp. 1697-1704, 2004.

[92] T. Miyata, Y. Minamino, S. Ida, and T. Minami, "Highly transparent and conductive ZnO:Al thin films prepared by vacuum arc plasma evaporation," *Journal of Vacuum Science & Technology A: Vacuum, Surfaces, and Films*, vol. 22, pp. 1711-1715, 2004.

[93] H. Tanaka, K. Ihara, T. Miyata, H. Sato, and T. Minami, "Low resistivity polycrystalline ZnO:Al thin films prepared by pulsed laser deposition," *Journal of Vacuum Science & Technology A: Vacuum, Surfaces, and Films*, vol. 22, pp. 1757-1762, 2004.

[94] H. Ko, W.-P. Tai, K.-C. Kim, S.-H. Kim, S.-J. Suh, and Y.-S. Kim, "Growth of Al-doped ZnO thin films by pulsed DC magnetron sputtering," *Journal of Crystal Growth*, vol. 277, pp. 352-358, 2005.

[95] B.-Y. Oh, M.-C. Jeong, W. Lee, and J.-M. Myoung, "Properties of transparent conductive ZnO:Al films prepared by co-sputtering," *Journal of Crystal Growth*, vol. 274, pp. 453-457, 2005.

[96] J. G. Lu, Z. Z. Ye, Y. J. Zeng, L. P. Zhu, L. Wang, J. Yuan, B. H. Zhao, and Q. L. Liang, "Structural, optical, and electrical properties of (Zn,Al)O films over a wide range of compositions," *Journal of Applied Physics*, vol. 100, pp. 073714-11, 2006.

[97] A. E. Manouni, F. J. Manjon, M. Mollar, B. Mari, R. Gomez, M. C. Lopez, and J. R. Ramos-Barrado, "Effect of aluminium doping on zinc oxide thin films grown by spray pyrolysis," *Superlattices and Microstructures*, vol. 39, pp. 185-192, 2006.

[98] B.-Y. Oh, M.-C. Jeong, T.-H. Moon, W. Lee, J.-M. Myoung, J.-Y. Hwang, and D.-S. Seo, "Transparent conductive Al-doped ZnO films for liquid crystal displays," *Journal of Applied Physics*, vol. 99, pp. 124505-4, 2006.

[99] S. W. Xue, X. T. Zu, W. G. Zheng, H. X. Deng, and X. Xiang, "Effects of Al doping concentration on optical parameters of ZnO:Al thin films by sol-gel technique," *Physica B: Condensed Matter*, vol. 381, pp. 209-213, 2006.

[100] W. Lin, R. Ma, J. Xue, and B. Kang, "RF magetron sputtered ZnO:Al thin films on glass substrates: A study of damp heat stability on their optical and electrical properties," *Solar Energy Materials & Solar Cells*, vol. 91, pp. 1902-1905, 2007.

[101] O. Bamiduro, H. Mustafa, R. Mundle, R. B. Konda, and A. K. Pradhan, "Metal-like conductivity in transparent Al:ZnO films," *Applied Physics Letters*, vol. 90, pp. 252108-3, 2007.

[102] B.-Z. Dong, G.-J. Fang, J.-F. Wang, W.-J. Guan, and X.-Z. Zhao, "Effect of thickness on structural, electrical, and optical properties of ZnO: Al films deposited by pulsed laser deposition," *Journal of Applied Physics*, vol. 101, pp. 033713-7, 2007.

[103] X. B. Zhang, Z. L. Pei, J. Gong, and C. Sun, "Investigation on the electrical properties and inhomogeneous distribution of ZnO:Al thin films prepared by dc magnetron sputtering at low deposition temperature," *Journal of Applied Physics*, vol. 101, pp. 014910-7, 2007.

[104] B.-Z. Dong, H. Hu, G.-J. Fang, X.-Z. Zhao, D.-Y. Zheng, and Y.-P. Sun, "Comprehensive investigation of structural, electrical, and optical properties for ZnO:Al films deposited at different substrate temperature and oxygen ambient," *Journal of Applied Physics*, vol. 103, pp. 073711, 2008.

[105] Y.-K. Moon, B. Bang, S.-H. Kim, C.-O. Jeong, and J.-W. Park, "Effects of working pressure on the electrical and optical properties of aluminum-doped zinc oxide thin films," *Journal of Materials Science - Materials in Electronics*, vol. 19, pp. 528-532, 2008.

[106] G. A. Hirata, J. McKittrick, J. Siqueiros, O. A. Lopez, T. Cheeks, O. Contreras, and J. Y. Yi, "High transmittance--low resistivity ZnO:Ga films by laser ablation," presented at The 42nd national symposium of the American Vacuum Society, Mineapolis, Minnesota (USA), 1996.

[107] N. R. Aghamalyan, E. A. Kafadaryan, R. K. Hovsepyan, and S. I. Petrosyan, "Absorption and reflection analysis of transparent conductive Ga-doped ZnO films," *Semiconductor Science and Technology*, vol. 20, pp. 80-85, 2005.

[108] V. Bhosle, A. Tiwari, and J. Narayan, "Electrical properties of transparent and conducting Ga doped ZnO," *Journal of Applied Physics*, vol. 100, pp. 033713-6, 2006.

[109] J. H. Kim, B. D. Ahn, C. H. Lee, K. A. Jeon, H. S. Kang, and S. Y. Lee, "Effect of rapid thermal annealing on electrical and optical properties of Ga doped ZnO thin films prepared at room temperature," *Journal of Applied Physics*, vol. 100, pp. 113515-3, 2006.

[110] A. Segura, J. A. Sans, D. Errandonea, D. Martinez-Garcia, and V. Fages, "High conductivity of Ga-doped rock-salt ZnO under pressure: Hint on

deep-ultraviolet-transparent conducting oxides," *Applied Physics Letters*, vol. 88, pp. 011910-3, 2006.

[111] C. Messaoudi, D. Sayah, and M. Abdlefdil, "Transparent Conducting undoped and indium-doped zinc-oxide films prepared by spray-pyrolysis," *Physica Status solidi A - Applied Research*, vol. 151, pp. 93097, 1995.

[112] J. M. Phillips, R. J. Cava, G. A. Thomas, S. A. Carter, J. Kwo, T. Siegrist, J. J. Krajewski, J. H. Marshall, W. F. Peck, and D. H. Rapkine, "Zinc-Indium-Oxide - a High-Conductivity Transparent Conducting Oxide," *Applied Physics Letters*, vol. 67, pp. 2246-2248, 1995.

[113] M. S. Tokumoto, A. Smith, C. V. Santilli, S. H. Pulcinelli, A. F. Craievich, E. Elkaim, A. Traverse, and V. Briois, "Structural electrical and optical properties of undoped and indium doped ZnO thin films prepared by the pyrosol process at different temperatures," *Thin Solid Films*, vol. 416, pp. 284-293, 2002.

[114] M. P. Taylor, D. W. Readey, C. W. Teplin, M. van Hest, J. L. Alleman, M. S. Dabney, L. M. Gedvilas, B. M. Keyes, B. To, P. A. Parilla, J. D. Perkins, and D. S. Ginley, "Combinatorial growth and analysis of the transparent conducting oxide ZnO/In (IZO)," *Macromolecular Rapid Communications*, vol. 25, pp. 344-347, 2004.

[115] B. Kumar, H. Gong, and R. Akkipeddi, "High mobility undoped amorphous indium zinc oxide transparent thin films," *Journal of Applied Physics*, vol. 98, pp. 073703-5, 2005.

[116] Y. Cao, L. Miao, S. Tanemura, M. Tanemura, Y. Kuno, Y. Hayashi, and Y. Mori, "Optical Properties of Indium-Doped ZnO Films," *Japanese Journal of Applied Physics*, vol. 45, pp. 1623-1628, 2006.

[117] B. D. Ahn, H. S. Kang, J. H. Kim, G. H. Kim, H. W. Chang, and S. Y. Lee, "Synthesis and analysis of Ag-doped ZnO," *Journal of Applied Physics*, vol. 100, pp. 093701-6, 2006.

[118] T. Minami, T. Yamamoto, and T. Miyata, "Highly transparent and conductive rare earth-doped ZnO thin films prepared by magnetron sputtering," *Thin Solid Films*, vol. 366, pp. 63-68, 2000.

[119] R. D. Shannon, “Revised effective Ionic Radii and Systematic Studies of Interatomic Distances in Halides and Chalcogenides.” *Acta Cryst.*, vol A32, p751, 1976

[120] B. B. He, "Introduction to two-dimensional X-ray diffraction," *Powder Diffraction*, vol. 18, pp. 71-85, 2003.

[121] E. Burstein, "Anomalous Optical Absorption Limit in InSb," *Physical Review*, vol. 93, pp. 632, 1953.

[122] J. T. Last, "Infrared-Absorption Studies on Barium Titanate and Related Materials," *Physical Review*, vol. 105, pp. 1740-1750, 1957.

[123] W. G. Spitzer, R. C. Miller, D. A. Kleinman, and L. E. Howarth, "Far Infrared Dielectric Dispersion in BaTio3, SrTiO3, and TiO2," *Physical Review*, vol. 126, pp. 1710-1721, 1962.

[124] S. S. A. Seo, H. N. Lee, and T. W. Noh, "Infrared spectroscopy of CaTiO3, SrTiO3, BaTiO3, Ba.5Sr.5TiO3 thin films and BatiO3/SrTiO3 superlattice grown on SrRuO3/SrTiO3 substrates," *Thin Solid Films*, vol. 486, pp. 94-97, 2005.

[125] S.-S. Lin, J.-L. Huang, and P. Sajgalik, "The properties of heavily Al-doped ZnO films before and after annealing in the different atmosphere," *Surface and Coatings Technology*, vol. 185, pp. 254-263, 2004.

[126] B. D. Ahn, S. H. Oh, H. L. Lee, G. H. Kim, K. H. Jae, and S. Y. Lee, "Influence of thermal annealing ambient on Ga-doped ZnO thin films," *Journal of Crystal Growth*, vol. 309, pp. 128-133, 2007.

[127] X. Chen, W. Guan, G. Fang, and X. Z. Zhao, "Influence of substrate temperature and post treatment on the properties of ZnO: Al thin films prepared by pulsed laser deposition," *Applied Surface Science*, vol. 252, pp. 1561-1567, 2005.

[128] V. Khranovkyy, U. Grossner, V. Lasorenko, G. Lashkarev, B. G. Svensson, and R. Yakimova, "Study of annealing influence on electrical and morphological properties of ZnO: Ga thin films," *Physica status solidi (c)*, vol. 3, pp. 780-784, 2006.

[129] J. Hafner, C. Wolverton and G. Ceder, “Towards computational materials design: The impact of density functional theory on materials research,” *MRS Bulletin,* vol. 31, pp. 659, 2006.

[130] P. Hohenberg and W. Kohn, *Physical Review B*, vol. 136, pp. 864, 1964.

[131] W. Kohn and L. J. Sham, *Physical Review A*, vol. 140, pp. 1133, 1965.